TU Graz
Graz University of Technology

The 19th International IGTE Symposium

on Numerical Field Calculation in Electrical Engineering

IGTE '20

Proceedings

Sept. 20 - 23, 2020

Hotel Novapark, Graz, Austria

Alice Reinbacher-Köstinger (editor)

Institute for Fundamentals and Theory in Electrical Engineering

IGTE

The 19th International IGTE Symposium on Numerical Field Calculation in Electrical Engineering was sponsored and supported by:







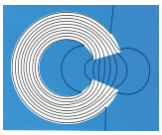

Imprint

Organisation: Christian Magele, Alice Reinbacher-Köstinger and Thomas Bauernfeind
Graz University of Technology, Institute of Fundamentals and Theory in Electrical Engineering (IGTE)

Editor: Alice Reinbacher-Köstinger
Layout: Alice Reinbacher-Köstinger
Cover: Alice Reinbacher-Köstinger

2025 Verlag der Technischen Universität Graz
www.tugraz-verlag.at

Proceedings of the 19th International IGTE Symposium on Numerical Field Calculation in Electrical Engineering, Graz, Novapark, 20-23.9.2020

ISBN (e-book): 978-3-85125-970-4
DOI: 10.3217/978-3-85125-970-4

List of Proceedings

Multi-objective free-form shape optimization of a synchronous reluctance machine

P. Gangl*, S. Köthe*, C. Mellak†, A. Cesarano*, and A. Mütze†

*Institute of Applied Mathematics, TU Graz, Steyrergasse 30, A-8010 Graz
† Electric Drives and Machines Institute, TU Graz, Inffeldgasse 18, A-8010 Graz
E-mail: gangl@math.tugraz.at

***Abstract*—This paper deals with the design optimization of a synchronous reluctance machine to be used in an X-ray tube, where the goal is to maximize the torque, by means of gradient-based free-form shape optimization. The presented approach is based on the mathematical concept of shape derivatives and allows to obtain new motor designs without the need to introduce a geometric parametrization. We validate our results by comparing them to a parametric geometry optimization in JMAG by means of a stochastic optimization algorithm. While the obtained designs are of similar shape, the computational time used by the gradient-based algorithm is in the order of minutes, compared to several hours taken by the stochastic optimization algorithm. Finally, we show an extension of the free-form shape optimization algorithm to the case of multiple objective functions and illustrate a way to obtain an approximate Pareto front.**

***Index Terms*—multiobjective shape optimization, shape derivative, synchronous reluctance machine.**

I. Introduction

In many industrial applications, the design of electric machines has to be tailored to the application at hand since off-the-shelf solutions are not available. The design of electric machines is usually based on engineering knowledge and is sometimes refined by geometric optimization. The most widely used approach is to introduce geometric parameters and optimize these, either using stochastic optimization algorithms or derivative-based methods, see [1] for an overview article. While derivative-based optimization algorithms successively improve a given initial geometry by means of gradient information and are known to converge to a local optimum rather fast, stochastic algorihtms include random effects and are less prone to getting stuck in local optima. In practice, one is usually confronted with several conflicting objective functions thus making multiobjective optimization capabilities for finding a Pareto optimal set of designs important. The extension to a multiobjective setting is more straightforward in the case of many stochastic optimization algorithms, however it can also be achieved in the case of derivative-based methods [2].

In recent years, non-parametric shape optimization methods based on the mathematical concept of shape derivatives [3] (often refered to free-form shape optimization approaches) have become a more and more popular tool for the design optimization of electric machines, see e.g. [4], [5], [6] for approaches using the finite element method or the recent work [7] in the context of isogeometric analysis. In these approaches, the geometry is not parametrized by a finite number of scalar values, but the design variable is a set, e.g. the set of points occupied by ferromagnetic material in the rotor of an electric machine. Starting out from a given initial design, the design is updated by the action of a smooth vector field, thus allowing for any kind of design that is topologically equivalent to the initial design. This way, often new and innovative designs can be obtained.

The purpose of this paper is two-fold: On the one hand, we extend the gradient-based multi-objective optimization method introduced in the case of a parametrized geometry in [2] to the case of free-form shape optimization. This allows to exploit the flexibility of free-form shape optimization methods, as well as their fast convergence properties also in the practically important case of multiple competing objective functions. On the other hand, we employ this method on both, the more standard single-objevtive case and, in the case of two objective functions, to find (Pareto-)optimal designs of a synchronous reluctance machine. Comparing our results with the results obtained by a stochastic parameter optimization confirms the higher degree of flexibility and computational efficiency of our approach compared to parametric design optimization.

The rest of this paper is organized as follows: In Section II we introduce the problem at hand and state the mathematical model. We recall the main ingredients for a free-form shape optimization method and apply the algorithm to our problem in Section III. In Section IV we show an extension of the gradient-based free-form shape optimization algorithm to the case of multiple objective functions before concluding in Section V.

II. Problem description

A. Physical model

We consider the design optimization of a synchronous reluctance machine (SynRM), i.e., a motor that is based solely on the reluctance principle. This motor generates torque exclusively by a difference of reluctance between two axes, namely the d-axis and the q-axis (the location of the axes is defined by the number of poles of the machine). Thus, torque generation is not based on any transient behavior or quantity and a static magnetic field analysis is sufficient. The machine under investigation

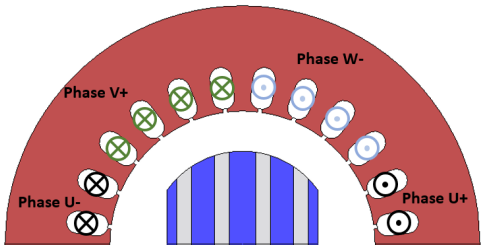

Figure 1. Upper half of synchronous reluctance machine with a three phase, two pole stator. The rotor consists of alternating magnetically conducting (blue) and non-conducting layers (gray).

Table I
EXAMPLE CASE MACHINE DESIGN PARAMETERS.

Parameter	Value
Stator	
Inner radius	26.5 mm
Outer radius	47.5 mm
Number of slots	24
Number of phases	3
Number of poles	2
Axial length	50 mm
Winding type	single-layer distributed
No. of turns per slot	64
Phase resistance $R_{\mathrm{S},20\,^\circ\mathrm{C}}$	7.1 Ω
Rated voltage U_{eff}	230 $\mathrm{V_{ac}}$/ 400 $\mathrm{V_{ac}}$
Connection	star
Rotor	
Outer radius	18.5 mm

is intended for the use in an X-Ray tube for medical applications. The considered rotor will be operated in a vacuum and therefore must be built of solid pieces of metal (as opposed to the commonly used steel sheet structure). Additionally, the air gap of the motor is unusually large (e.g., 10 mm with an outer stator diameter of 130 mm) decreasing the torque capability of the machine. Furthermore, the rotor has to withstand temperatures of up to 450 °C. [10]

The synchronous reluctance machine is particularly suitable for such an application mainly due to its ruggedness and construction simplicity and the absence of rotor windings [11]. As per the operation mode of the machine quick acceleration and subsequent braking of a tungsten disk is required. Typically, this sequence takes at maximum 10 s. Figure 1 shows the machine under investigation. The stator is a three phase stator with one pole pair, the rotor consists of alternating magnetically conducting (blue) and non-conducting layers (gray). The reference design parameters of the machine are stated in Table I.

Figure 2 shows the simplified vector diagram of a synchronous reluctance machine. The d-axis of the machine is the path with least reluctance, the q-axis is the path with the highest reluctance. In the d-q axis theory, the torque is expressed as

$$T = \frac{3N_p}{2}(\lambda_\mathrm{d}\mathrm{I_q} - \lambda_\mathrm{q}\mathrm{I_d}),$$

where N_p denotes the number of pole pairs, λ_d and λ_q are

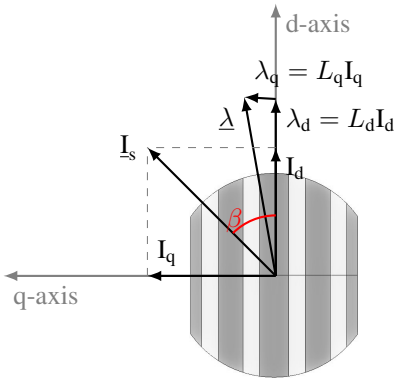

Figure 2. Vector diagram of a synchronous reluctance machine for the simplified model in d-q reference frame [9].

the magnetic flux linkages, and $\mathrm{I_d}$ and $\mathrm{I_q}$ are the currents in d-axis and q-axis direction, respectively. Alternatively, using the inductances L_d and L_q as well as the stator current $\mathrm{I_s}$ and current angle β, the torque is expressed as

$$T = \frac{3N_p}{4}(L_\mathrm{d} - L_\mathrm{q})\mathrm{I_s^2}\sin(2\beta)\,. \tag{1}$$

Evidently, as per (1), assuming linear lossless behaviour and a fixed stator current $\mathrm{I_s}$ the maximum torque can be achieved with a machine current angle β (angle between current vector and d-axis of the machine, Fig. 2) of 45°. [8]

B. Optimization goal

A static analysis is chosen to calculate the reluctance torque. Therefore, a current is impressed on the windings according to Table II. Subsequently, the rotor is rotated and fixed clockwise to create the optimal current angle β of 45°. The objective is to increase the torque with the given stator at a constant current and air gap length at the optimum current angle β. The number of conducting and non-conducting layers remains unchanged. Solely the shape of each individual layer is subject to the optimization as to increase the d-axis inductance L_d while, ideally, decreasing the q-axis inductance L_q at the same time.

Table II
THE CURRENT VALUES FOR EACH WINDING.

U-Phase	V-Phase	W-Phase
12 A	-6 A	-6 A

C. Mathematical model

We consider a two-dimensional cross-section of the machine in the setting of 2D magnetostatics, i.e., $\mathbf{B} = \mathrm{curl}\mathbf{A}$ where the magnetic vector potential is of the form $\mathbf{A} = (0, 0, u(x_1, x_2))^\top$. Let $D \subset \mathbb{R}^2$ denote the computational domain which comprises the two-dimensional cross section of the machine as well as a surrounding air

region, and let $\Omega \subset D$ denote the ferromagnetic parts of the machine. The mathematical design optimization problem reads

$$\max_{\Omega \in \mathcal{A}} T(u) \tag{2}$$

$$\begin{aligned} \text{s.t. } -\operatorname{div}(\nu_\Omega(x, |\nabla u|)\nabla u) &= J_i, \quad x \in D, \\ u &= 0, \quad x \in \partial D, \end{aligned} \tag{3}$$

where T represents the torque for the considered rotor position, $\mathcal{A}$ is a set of admissible shapes, J_i represents the impressed current density and the magnetic reluctivity is defined piecewise as

$$\nu_\Omega(x, s) = \begin{cases} \hat{\nu}(s) & x \in \Omega, \\ \nu_0 & x \in D \setminus \overline{\Omega}. \end{cases}$$

Here, $\hat{\nu}$ is a nonlinear function which represents the magnetic reluctivity of the ferromagnetic material, and ν_0 corresponds to the magnetic reluctivity of air. The partial differential equation (PDE) constraint (3) admits a unique solution under natural assumptions on the nonlinear function $\hat{\nu}$ [12]. Note that the torque T depends on the shape Ω of the ferromagnetic components via the solution to the PDE constraint (3). Denoting the unique solution to (3) for given $\Omega \in \mathcal{A}$ by u_Ω, we define the reduced cost function $\mathcal{T}(\Omega) := T(u_\Omega)$.

III. Free-form shape optimization

We propose a free-form shape optimization algorithm based on the mathematical concept of shape derivatives, which is capable of improving the shape of a given initial geometry without the need of defining geometric parameters. We will outline the main ingredients to the method in the following. We introduce the theory for a general cost function $\mathcal{J}$ and will choose $\mathcal{J} := -\mathcal{T}$ later in Section III-C.

A. Shape derivative

The shape derivative of a general shape function $\mathcal{J} = \mathcal{J}(\Omega)$ represents the sensitivity of $\mathcal{J}$ when the domain Ω is perturbed by the action of a given vector field V. Given a smooth vector field V which is defined on D, let $\Omega_t = (\mathrm{id} + tV)(\Omega)$ denote the perturbed domain for $t > 0$. The shape derivative of $\mathcal{J}$ in the direction given by V is defined as

$$d\mathcal{J}(\Omega; V) := \lim_{t \searrow 0} \frac{\mathcal{J}(\Omega_t) - \mathcal{J}(\Omega)}{t}, \tag{4}$$

provided that this limit exists and the mapping $V \mapsto d\mathcal{J}(\Omega; V)$ is linear and continuous [3].

The shape derivative for problem (2)–(3) can be derived in an analogous way as it was done in [4] and, for a vector field V that is only supported on the rotor, reads

$$\begin{aligned} d\mathcal{J}(\Omega; V) = \\ + \int_D \nu_\Omega(x, |\nabla u|) \left((\operatorname{div} V) I - \partial V^T - \partial V \right) \nabla u \cdot \nabla p \, \mathrm{d}x \\ - \int_D \frac{\partial_s \nu_\Omega(x, |\nabla u|)}{|\nabla u|} (\partial V^T \nabla u \cdot \nabla u)(\nabla u \cdot \nabla p) \, \mathrm{d}x. \end{aligned} \tag{5}$$

Here, p denotes the solution to the adjoint equation which for the case of the maximization of the torque reads in its strong form

$$\begin{aligned} \text{s.t. } -\operatorname{div}(A_\Omega(u)\nabla p) &= \frac{\partial T}{\partial u}, \quad x \in D, \\ p &= 0, \quad x \in \partial D. \end{aligned} \tag{6}$$

with

$$A_\Omega(u) := \nu_\Omega(x, |\nabla u|) I + \frac{\nu_\Omega'(x, |\nabla u|)}{|\nabla u|} \nabla u \otimes \nabla u.$$

B. Descent direction

Given a closed formula for the shape derivative, a descent vector field V can be obtained by solving an auxiliary boundary value problem as follows. Let X be a Hilbert space and $b : X \times X \to \mathbb{R}$ a symmetric and positive definite bilinear form. Then the solution $W \in X$ to the variational problem

$$b(W, V) = -d\mathcal{J}(\Omega; V) \; \forall V \in X \tag{7}$$

is a descent direction since it satisfies by construction

$$d\mathcal{J}(\Omega; W) = -b(W, W) < 0.$$

Thus, it follows from the definition in (4) that perturbing Ω a small distance into the direction W will yield a decrease of the cost function $\mathcal{J}$.

The user has some degrees of freedom in the choice of the bilinear form $b(\cdot, \cdot)$ as well as the space X. Common choices include $X = H^1(D, \mathbb{R}^2)$ and $b(W, V) = \int_D \partial W : \partial V + W \cdot V \mathrm{d}x$ or $b(W, V) = \int_D C\epsilon(W) : \epsilon(V) + W \cdot V \mathrm{d}x$ where $\epsilon(V) = \frac{1}{2}(\partial V + \partial V^\top)$ and C is a fourth-order elasticity tensor. The latter choice is known to preserve mesh quality better compared to other choices of $b(\cdot, \cdot)$ [13]. An alternative strategy for extracting a descent direction which also allows for the extension to multiple objective functions will be discussed in Section IV-A.

C. Numerical results

The procedure outlined in Sections III-A and III-B constitutes the following free-form shape optimization algorithm for minimization of shape function $\mathcal{J} = \mathcal{J}(\Omega)$:

Algorithm 1. *Given initial design Ω_0, cost function $\mathcal{J}$, tolerance tol, $k = 0$.*

1) *Solve state equation* (3) *and adjoint equation* (6)
2) *Compute shape derivative $d\mathcal{J}(\Omega_k; V)$ given in* (5)
3) *Compute shape gradient W as solution to* (7)
4) *If $\|W\| < tol$ then stop*
   else set $\Omega_{k+1} = (id + tW)(\Omega_k)$ where $t = max\{1, \frac{1}{2}, \frac{1}{4}, \frac{1}{8}, \dots\}$ such that $\mathcal{J}(\Omega_{k+1}) < \mathcal{J}(\Omega_k)$.
5) *$k \quad k+1$ and go back to 1)*

In step 4) the parameter t is chosen by a line search in order to guarantee a descent of the cost function $\mathcal{J}$.

We applied Algorithm 1 to problem (2)–(3), i.e. we chose to minimize $\mathcal{J}(\Omega) := -\mathcal{T}(\Omega)$, using the finite

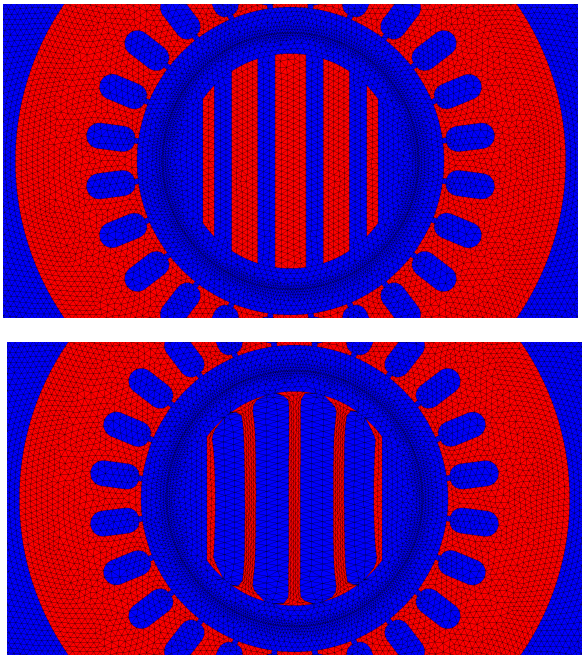

Figure 3. Top: Initial design of rotor, $T = 1.007$ Nm. Bottom: Optimized design obtained after 70 iterations of Algorithm 1, $T = 1.270$ Nm.

element software package NGSolve [14]. In particular, we used the automated shape differentiation capabilities provided by NGSolve which enables the automated computation of the shape derivative $d\mathcal{J}(\Omega; V)$ for a large class of PDE-constrained shape optimization problems [15].

For the space X in (7), we chose the space of all vector-valued H^1 functions defined on the rotor of the machine whose normal component vanishes on the top and bottom boundary parts of the rotor and which vanish at the left and right boundary parts. For the bilinear form $b(\cdot, \cdot)$ we chose the H^1 inner product

$$b(V, W) := \int_{D_{rot}} \partial V : \partial W + \frac{1}{100} V \cdot W \, \mathrm{d}x,$$

where D_{rot} denotes the union of the five iron and four air layers as depicted in Figure 3. The results obtained after 70 iterations of Algorithm 1 are depicted in Figure 3. The torque was increased by about 26% from 1.007 Nm to 1.270 Nm. The computational time to obtain the optimized design was about 10 minutes on a single core.

D. Validation

In this section, we validate the results obtained in our numerical experiments by comparing them to an optimization run in JMAG [16]. Motivated by the results of the gradient-based optimization, see Fig. 3, we parametrized our rotor geometry by means of 14 geometric parameters under symmetry conditions, see Fig. 4, and ran a genetic algorithm which is built into JMAG to maximize the torque. We started with a population size of 300 and ran the algorithm for 50 generations, allowing

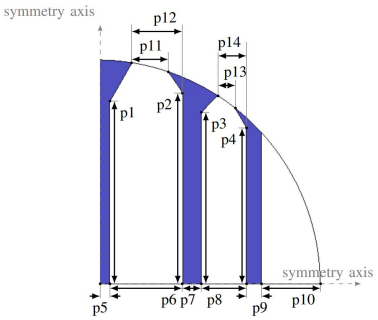

Figure 4. Geometric parameters used for genetic algorithm.

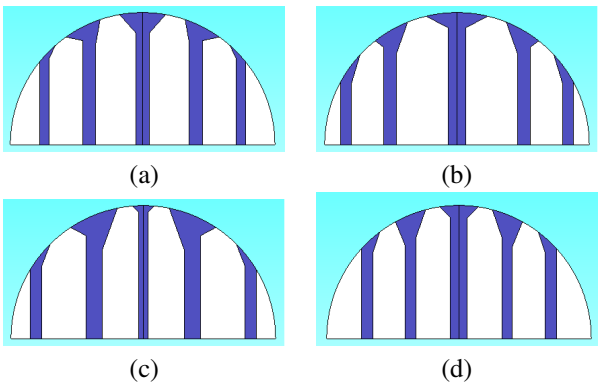

Figure 5. Best results obtained by genetic algorithm in JMAG based on geometric parametrization of Fig. 4 after 300 generations. (a) best design, $T = 1.2119$Nm. (b) second best design, $T = 1.2091$Nm. (c) third best design, $T = 1.2082$Nm. (d) fourth best design, $T = 1.2067$Nm.

for 60 children in each generation. The computational time used by the genetic algorithm was about 19 hours and a total of 15000 designs were examined. The four designs with the highest torque values are depicted in Fig. 5. It can be seen that the best designs are similar to the design we obtained by the gradient-based algorithm (Fig. 3), but also that the torque values were not quite reached. While one might be tempted to explain such a discrepancy by the fact that different simulation tools were used, we mention that the calculated torques in the two simulation softwares (NGSolve and JMAG) showed a good match for the initial geometry. Thus, it seems like the design in Fig. 3 is superior to those obtained by the genetic algorithm in JMAG since more general geometries can be obtained. Of course, the computation time of 19 hours could be reduced by reducing the parameters of the genetic algorithm, however the general order of magnitude remains. Finally note that, since the choice of the geometric parameters was inspired by Fig. 3, the designs in Fig. 5 would have been unlikely to be found without the knowledge provided by the free-form shape optimization algorithm.

IV. Multi-objective shape optimization

In this section we consider an extension of the gradient-based free-form shape optimization method presented in Section III to the setting of multiple objective

functions. We show how to compute a descent vector field W that assures a descent with respect to several objective functions and use this approach in order to obtain an approximation of the Pareto front. We apply the method to the bi-objective free-form shape optimization problem

$$\min_{\Omega} \begin{pmatrix} \mathcal{J}_1(\Omega) \\ \mathcal{J}_2(\Omega) \end{pmatrix}$$

where $\mathcal{J}_1(\Omega) := -\mathcal{T}(\Omega)$ corresponds to the negative of the torque related to Ω and $\mathcal{J}_2(\Omega) := \mathrm{Vol}(\Omega)$ denotes the volume of the ferromagnetic subdomains of the machine.

A. Multi-objective descent direction

Given two shape functions $\mathcal{J}_1$, $\mathcal{J}_2$ and their corresponding shape derivatives $d\mathcal{J}_i(\Omega; V)$, $i = 1, 2$, we want to find a vector field W such that

$$d\mathcal{J}_1(\Omega; W) < 0 \quad \text{and} \quad d\mathcal{J}_2(\Omega; W) < 0.$$

We extend the ideas introduced in the framework of parametric shape optimization in [2] to the setting of free-form shape optimization. For that purpose, we consider a finite element discretization using piecewise linear and globally continuous finite elements on a triangular mesh. Denoting the corresponding hat basis functions by $\varphi_1, \ldots, \varphi_n$ where n is the number of mesh points and $\Phi_i = (\varphi_i, 0)^\top$, and $\Phi_{n+i} = (0, \varphi_i)^\top$, $i = 1, \ldots, n$, we have that

$$\{\Phi_1, \ldots, \Phi_{2n}\}$$

is a basis for the set of all two-dimensional vector fields on the mesh. Thus, after discretization each vector field W_h can be written as $W_h = \sum_{i=1}^{2n} W_i \Phi_i$ with the coefficient vector $\underline{W} := (W_1, \ldots W_{2n})^\top$. Note that we can identify the finite element function W_h with its coefficient vector $\underline{W}$. In order to obtain a discrete bi-descent direction W_h, we solve the auxiliary optimization problem to find $(\rho, \underline{W}) \in \mathbb{R} \times \mathbb{R}^{2n}$

$$\begin{aligned} \min_{\rho, \underline{W}} \ & \rho + \frac{1}{2} \sum_{i=1}^{2n} W_i^2, \\ \text{s.t.} \quad & d\mathcal{J}_1(\Omega; W_h) \leq \rho, \\ & d\mathcal{J}_2(\Omega; W_h) \leq \rho. \end{aligned} \tag{8}$$

Due to the linearity of the shape derivatives $d\mathcal{J}_i(\Omega; W_h)$ with respect to W_h, the solution $(\rho, \underline{W}) = (0, \mathbf{0}) \in \mathbb{R} \times \mathbb{R}^{2n}$ is a feasible point of (8). Therefore, it follows that the solution $(\rho, \underline{W})$ to (8) satisfies $d\mathcal{J}_i(\Omega; W_h) \leq \rho \leq 0$, $i = 1, 2$, thus giving a bi-descent direction W_h whenever the optimal ρ is negative. The second term in the cost function of (8) is meant to keep the norm of W_h bounded.

We remark that, in contrast to the widely used weighted-sum method, this approach is also feasible for finding non-convex parts of a Pareto front [2]. Of course, an extension of this approach to account for more than two cost functions $\mathcal{J}_1, \ldots, \mathcal{J}_N$ is straightforward.

B. Obtaining a Pareto front

Proceeding as described in Section IV-A allows to obtain a bi-descent direction W_h. Thus, starting out from an initial design, iteratively computing a bi-descent vector field and moving the interface a small distance in the direction given by this vector field constitutes a gradient-based free-form shape optimization algorithm for two cost functions. When no further decrease can be obtained, a Pareto optimal point is found.

In order to obtain many Pareto optimal points, one could start with many different initial designs. However, it turns out to be more convenient to proceed as follows: Consider different scalings of the two objective functions, i.e. apply the gradient-based biobjective descent algorithm for the two objective functions $\mathcal{J}_1$ and $w\mathcal{J}_2$ with different values of the weight w, see also [2]. Each choice of the weight w corresponds to a run of the bi-objective descent algorithm and will yield a point on the Pareto front.

C. Numerical results

The proposed algorithm to obtain an approximation of a Pareto front consists in a loop over different weights w where each iteration uses an algorithm similar to Algorithm 1 to obtain an optimized design. In contrast to Algorithm 1, however, here the descent direction is obtained by solving the auxiliary optimization problem (8) rather than an auxiliary boundary value problem of the form (7). The algorithm reads as follows:

Algorithm 2. *Given initial design Ω_0, cost functions $\mathcal{J}_1, \mathcal{J}_2$, tolerance tol, set of weights $\{w_1, \ldots, w_M\}$.*
For $j = 1, \ldots, M$:

1) *If $j > M$ then stop*
   else set $\tilde{\mathcal{J}}_1 \leftarrow \mathcal{J}_1$, $\tilde{\mathcal{J}}_2 \leftarrow w_j \mathcal{J}_2$.
2) *Set $k \leftarrow 0$, $\Omega_0^{(j)} \leftarrow \Omega_0$*
3) *For $k = 0, 1, 2, \ldots$*
   (i) *Solve state equation* (3) *and adjoint equation* (6)
   (ii) *Compute shape derivatives $d\tilde{\mathcal{J}}_1(\Omega_k^{(j)}; V)$, $d\tilde{\mathcal{J}}_2(\Omega_k^{(j)}; V)$*
   (iii) *Compute bi-objective descent direction W_h as solution to* (8) *with $d\tilde{\mathcal{J}}_1(\Omega_k^{(j)}; \cdot)$, $d\tilde{\mathcal{J}}_2(\Omega_k^{(j)}; \cdot)$*
   (iv) *If $\|W_h\| < tol$ then $j \leftarrow j + 1$ and go to 1) else set $\Omega_{k+1}^{(j)} = (id + tW_h)(\Omega_k^{(j)})$ where $t = max\{1, \frac{1}{2}, \frac{1}{4}, \frac{1}{8}, \ldots\}$ such that $\mathcal{J}_i(\Omega_{k+1}^{(j)}) < \mathcal{J}_i(\Omega_k^{(j)})$, $i = 1, 2$.*

In our implementation, we solved the quadratic optimization problem involving linear inequality constraints (8) by means of a sequential least squares programming optimization algorithm using the functionality `scipy.optimize(...)`. In order to reduce computation time, we restricted problem (8) to the degrees of freedom on the material interfaces which are subject to optimization and neglected the interior degrees of freedom. This is motivated by the fact that a movement

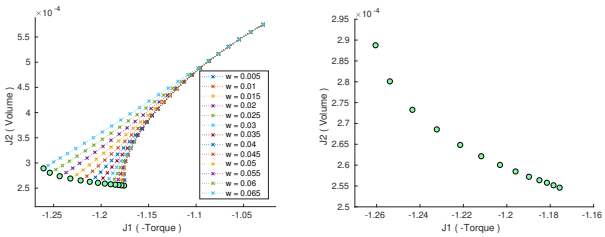

Figure 6. Left: Values of different designs obtained in the course of gradient based two-objective optimization algorithm for different weights w. Right: Zoom on approximated Pareto front.

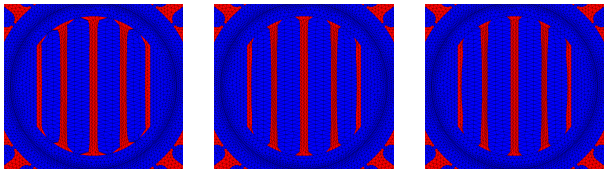

$w = 0.065$	$w = 0.035$	$w = 0.005$
$T = 1.260$	$T = 1.203$	$T = 1.176$
$V = 2.89 \cdot 10^{-4}$	$V = 2.60 \cdot 10^{-4}$	$V = 2.55 \cdot 10^{-4}$

Figure 7. Three different designs obtained on the approximated Pareto front by using different weights w for $\mathcal{J}_2$.

of points inside a subdomain does not alter the shape. Proceeding like this, we obtain a deformation vector field that is only supported on the material interfaces and vanishes on all interior mesh nodes. In order to avoid intersection of the mesh when updating the geometry, we extend the vector field from the interfaces to the whole rotor domain by harmonic extension, i.e., by solving an elliptic PDE. As additional constraints, we imposed the linear equality constraints that the normal component of the vector field on the boundary on the rotor domain vanishes, i.e. $W_x(z)n_x(z) + W_y(z)n_y(z) = 0$ for all mesh points $z \in \partial D_{rot}$. These constraints ensure that the radius of the rotor remains unchanged.

Figure 6 (left) shows the results of the bi-objective descent algorithm for minimizing the negative torque and w times the volume, $\mathcal{J}_1(\Omega) = -\mathcal{T}(\Omega)$ and $w\mathcal{J}_2(\Omega) = w\mathrm{Vol}(\Omega)$, for different choices of the weighting factor w. The right picture of Figure 6 depicts a zoom on the obtained Pareto optimal points. The computational effort for obtaining one Pareto optimal design is comparable to the cost of one single-objective optimization run (see Sec. III-C), amounting to a computational time of about two hours on a single core to obtain the depicted Pareto front. The Pareto optimal designs corresponding to three different choices of w can be seen in Figure 7.

V. Conclusion and Outlook

We addressed the problem of finding the optimal shape of the rotor of a synchronous reluctance machine as used in an X-ray tube by means of a gradient-based free-form shape optimization method which is based on the shape derivative. This approach allowed to obtain an optimized shape which exhibits an increase of the torque by 26% within only several minutes of computation time. The results are confirmed by a geometric parameter optimization in JMAG where the parametrization is motivated by the design obtained by free-form optimization. Moreover, we introduced an extension to the setting of multi-objective shape optimization and showed a way to obtain an approximate Pareto front while significantly decreasing the computation time when compared to evolutionary algorithms.

In this paper we only considered shape optimization approaches which cannot alter the connectivity of the initial design. A next step would be to consider topology optimization methods to additionally allow for changing topologies, in particular in the context of multi-objective optimization. While this was beyond the scope of this paper, it is subject of future work.

Acknowledgments

Alessio Cesarano has been funded by the Austrian Science Fund (FWF) project P 32911.

References

[1] G. Bramerdorfer, J. Tapia, J. Pyrhönen and A. Cavagnino, “Modern Electrical Machine Design Optimization: Techniques, Trends, and Best Practices,”, IEEE Trans. Ind. Electron., vol. 65, pp. 7672–7684, 2018.

[2] O. Doganay, H. Gottschalk, C. Hahn, K. Klamroth, J. Schultes, and M. Stiglmayr, “Gradient based biobjective shape optimization to improve reliability and cost of ceramic components”, Optim. Eng., 2019.

[3] M. Delfour and J.-P. Zolésio, Shapes and geometries, 2nd ed., vol. 22. Advances in Design and Control (SIAM), Philadelphia, 2011.

[4] P. Gangl, U. Langer, A. Laurain, H. Meftahi, and K. Sturm, “Shape optimization of an electric motor subject to nonlinear magnetostatics”, SIAM J. Scient. Comp., 37(6):B1002–B1025, 2015.

[5] E. Kuci, “Shape and topology optimization for electro-mechanical energy converters”, Doctoral dissertation, Université de Liège, Liège, Belgium, 2018.

[6] P. Putek, R. Pulch, A. Bartel, E.J. ter Maten, M. Günther, and K. Gawrylczyk, “Shape and topology optimization of a permanent-magnet machine under uncertainties”, J. Math. Industry vol. 6, 2016.

[7] M. Merkel, P. Gangl, and S. Schöps, “Shape Optimization of Rotating Electric Machines using Isogeometric Analysis and Harmonic Stator-Rotor Coupling”, arXiv eprint 1908.06009, submitted for publication.

[8] C. Spargo, “Synchronous reluctance technology : part I.” *MagNews.*, no. Winter, January 2013. [Online]. Available: http://dro.dur.ac.uk/18579/

[9] A. Binder, *Elektrische Maschinen und Antriebe*. Springer, 2012.

[10] C. Mellak, and K. Krischan and A. Muetze, “Synchronous Reluctance Machines as Drives for Rotary Anode X-Ray Tubes – A Feasibility Study“, ICEM 2018, pp. 2613–2618, 2018.

[11] L. Xu, X. Xu, Xingyi, T. Lipo, and D. Novotny, ”Vector control of a synchronous reluctance motor including saturation and iron loss“, IEEE Trans. Ind. Appl., vol 27(5), pp.977–985, 1991.

[12] C. Pechstein and B. Jüttler, “Monotonicity-preserving interproximation of B-H-curves”, J. Comp. App. Math., 196:45–57, 2006.

[13] J. A. Iglesias, K. Sturm, and F. Wechsung, “Two-dimensional shape optimization with nearly conformal transformations”, SIAM J. Scient. Comp., 40(6):A3807–A3830, 2018.

[14] J. Schöberl, “C++11 implementation of finite elements in NGSolve”, Technical Report 30, Institute for Analysis and Scientific Computing, Vienna University of Technology, 2014.

[15] P. Gangl, K. Sturm, M. Neunteufel, J. Schöberl, “Fully and Semi-Automated Shape Differentiation in NGSolve”, Struct. Multidisc. Optim., accepted.

[16] JSOL-Corporation,“JMAG : Simulation Technology for Electromechanical Design”, http://www.jmag-international.com/.

Enhanced beamforming techniques for cylindrical-substrate microstrip array antennas

Exadaktylos P. Christos (1), Karatzidis I. Dimitrios (1), Zygiridis T. Theodoros (2), Kantartzis V. Nikolaos (1)

(1) Department of Electrical and Computer Engineering, Aristotle University of Thessaloniki, Thessaloniki, Greece
(2) Department of Electrical and Computer Engineering, University of Western Macedonia, Florina, Greece

Purpose:

A class of robust and efficient beamforming methods is developed in this paper for the optimised design of realistic microstrip antennas on arbitrarily curved substrates. More specifically, this paper aims to focus on the formulation of an effective and computationally light beamforming algorithm and its implementation on a novel realistic cylindrical-substrate microstrip array antenna with significantly decreased size, wideband operation and enhanced radiation characteristics.

Design/methodology/approach:

The proposed multi-parametric schemes introduce an efficient null-steering concept, which drastically annihilates the undesired beamformer waveform artefacts, while retaining the real output signal undistorted. In particular, the key objective is the accurate calculation of the appropriate complex feeding weights, required to set nulls along the propagation directions of the unwanted signals and a maximum towards the propagation direction of the desired incoming signal. The featured technique, combined with a modified finite element method, is applied to the design of a new family of cylindrical-substrate microstrip array antennas.

Findings:

Numerical results, mainly concerning customisable three-dimensional radiation patterns and attributes, certify the merits of the algorithm and its limited system demands. The introduced beamforming algorithms are applied to a variety of different inputs (desired radiation patterns), which indicate that the designed cylindrical-substrate antenna overwhelms existing designs in terms of computational cost for the beamforming algorithm, while retaining acceptable values for radiation characteristics, such as gain, directivity and side-lobe suppression. In this manner, the effectiveness of the prior methodology and the benefits of this newly shaped array antenna are comprehensively revealed and substantiated.

Originality/value:

Rigorous beamforming techniques in conjunction with a class of contemporary array antennas are developed for potential use in high-end communication systems, such as 5G configurations. The proposed cylindrical-shaped structures are systematically designed, with an emphasis on space efficiency and wideband radiation effectiveness to offer fully adjustable setups. To this aim, the cylindrical-substrate microstrip antenna, because of its inherent azimuthal symmetry and confined overall dimensions, provides reliable operation and promising performance.

Keywords:

Beamforming methods, Cylindrical structures, Finite elements, Microstrip array antennas,Optimisation, Antenna, Microwaves, Finite element method, Design optimization methodology, Computational electromagnetics

Published in COMPEL - The international journal for computation and mathematics in electrical and electronic engineering, Vol. 41 No. 3, 2022, ISSN 0332-1649, page 766 - 780

Topology Optimization of Synchronous Reluctance Motors Made of Non-Annealed High-Silicon Steel

Arbaaz Khan, Vahid Ghorbanian and David A. Lowther
McGill University, Department of Electrical and Computer Engineering, Montreal, QC, Canada
Email: david.lowther@mcgill.ca

***Abstract*— This paper proposes topology optimization to maximize the torque of a synchronous reluctance motor with a rotor constructed from non-annealed silicon iron material. The process consists of measuring the B-H characteristic of the additively manufactured non-annealed metal powder, importing the measured B-H values to the finite element-based design and optimization software packages, and finally maximizing the torque of a synchronous reluctance motor, which has a rotor made of the tested magnetic material. The same process is performed with a conventional magnetic material, i.e. M19, to compare the results and provide guidelines for future improvements and leverage the proposed free-form optimization of a highly flexible additive manufacturing process. The results of the topology optimization applied to the both materials, M19 and high-silicon steel, reveal that the non-annealed 3D printed material produces less torque due to the smaller flux density levels at similar magnetic fields. The topology optimization is handled using a sequence-based method with implementation through Genetic Algorithm (GA) and Temporal Difference (TD) learning algorithms.**

***Index Terms*— Additive manufacturing, design, finite element method, synchronous reluctance motor, topology optimization.**

I. Introduction

The design optimization of low-frequency electromagnetic devices, such as electric motors, has been extensively studied in the literature [1]. As one of the major aspects and concerns of the existing research, different materials, topologies and the corresponding manufacturing methods have also been investigated in order to come up with an efficient, zero-waste and cost-effective method of manufacturing, which can lead to an optimal motor design [2], [3].

Among the methods, subtractive and additive manufacturing techniques have been proposed [4], [5]. Conventional subtractive methods, although being used as the core method in industry, suffer from a lack of flexibility in manufacturing complex shapes, such as (a) the barriers in synchronous reluctance machines obtained from a free-form topology optimization (TO) routine that guarantees a smooth torque performance, (b) the permanent magnets that remove the ripples in the airgap flux density in motors [6]; and (c) the stator windings that fill up the slots to the maximum capacity in order to get higher fill factors. On the other hand, the additive manufacturing (AM) techniques, also known as 3D printing, have opened appraoches to deal with the mentioned complex shapes and flexible manufacturing for some materials, such as non-magnetic steel, copper, composites and permanent magnets, as well as some devices, such as inductive (used in small, medium and high power applications) and capacitive (used in microelectromechanical systems) electric devices [7].

The AM of non-magnetic materials is now a mature technology, while more research on magnetic materials, mainly soft ones, is required to make sure that the desired characteristics are obtained from the AM process [8]. On the other hand, recent metallurgical advancements in metal powders, such as high-silicon iron, have made it possible to explore and study the possibility of employing AM for electric motors.

With respect to TO and its ability in flexible and complex shape design, TO methods have generated considerable interest in the field due to their capability to provide designers with complex designs that can outperform the templates available in commercial design packages [9]. The combination of TO with a sequence-based controller has led to a faster and an optimized solution that avoids the creation of non-manufacturable structures such as a checkerboard pattern. This TO method [9] neither requires any filtering nor smoothing technique. Further it will not require any modification to the optimization objective function for obtaining manufacturable optimal solutions. The applicability of this TO method is shown through two algorithm which vary a lot in their approach. Although both are based on a heuristic function for optimization, the setup of the problem is very different with the Genetic Algorithm (GA) depending on a randomly generated population and the principle of natural selection to discover useful sets of solution. On the other hand, Temporal Difference (TD) based learning converts the TO problem as a well-defined mathematical framework called the Markov Decision Process (MDP). Further TD learning involves a gradient based update through the learning process whereas GA is a gradient free optimization algorithm.

The concept has been adapted to electric machines as well [10] and has led to theoretically better, while experimentally difficult-to-manufacture, designs. This is where the AM along with the sequence based TO method can solve some of the issues with the manufacturing process.

AM and TO are the focuses of the current work, which (a) characterizes the magnetic behavior (the BH curve as well as the magnetic losses) of a non-annealed high-silicon iron (b) incorporates the characterized material into the finite element (FE) simulation of a synchronous reluctance motor with the stator and the rotor made of the high-silicon iron (c) employs a sequence-based topology optimization (TO) method to first, remove the constraints of template-based designs, and second, propose a shape of barrier that provides a higher torque and (d) compares the results to those of the standard M19 material and

propose guidelines for future improvements in terms of the characteristics of the 3D printed material, and consequently the electric motor made of it.

II. Topology Optimization Process of High-Silicon Iron for Additive Manufacturing of Electric Motors

Fig. 1 illustrates the proposed process which consists of:

- 3D printing of the high-silicon iron powder in the shape of lamination pieces.
- Measure the magnetic properties under sinusoidal excitation at different induction (the magnetic flux density) levels. The performance with PWM excitation can also be measured for an inverter-fed application.
- Perform the TO of the synchronous reluctance rotor using a sequence-based design optimization algorithm.

The assumption here is that the 3D printed material is non-annealed. This is considered the worst case since the annealing heat treatment normally improves the magnetic characteristics of the 3D printed metals. The measurement is also performed, with the same settings, on the M19 lamination.

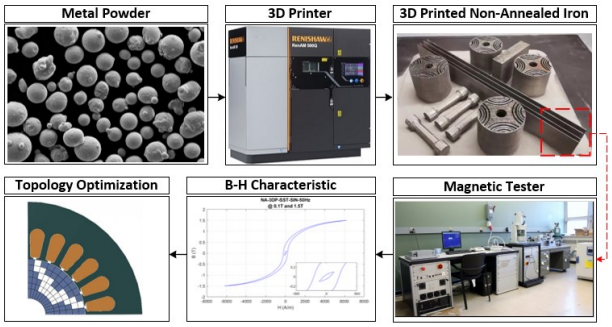

Fig. 1. 3D printing, test and topology optimization process

A. Material Characteristics

Fig. 2 shows and compares the magnetic behavior of the non-annealed high-silicon iron and M19. In this study, FeSi6.5 with 6.5wt% of silicon is used. The average particle size of the metal powder is about 30 µm. The bulk density is 4.17 g/cm^3. A Renishaw Metal 3D printer was utilized to print the metal powder using the Selective Laser Melting (SLM) technology [11]. Some parts were printed, including the lamination pieces, the coupons and some rotors. Only the laminations are used in this paper, while the other parts will be used in future works related to the structural integrity and overall motor drive performance of the 3D printed motor. Next, the laminations were tested using the single sheet tester of the Brockhaus magnetic testing setup [12]. The test consists of:

- A pure sinusoidal excitation
- Multiple frequencies (50, 200 and 400Hz) in order to compute the eddy and hysteresis loss coefficients more accurately
- Magnetic flux density (B) range of [0-1.5]T
- B is regulated while H is adjusted to get the requested B value.

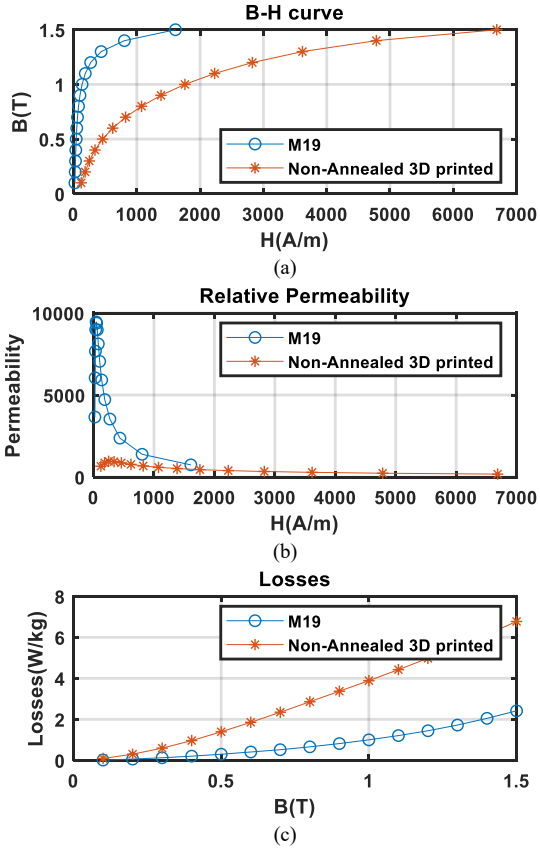

Fig. 2. (a) Magnetization curve (b) Relative permeability (c) Magnetic losses at 50Hz

All the tests were performed at room temperature (approximately 20 deg C). No compressive or tensile stress was applied to the materials. The results of the magnetic test are provided in Fig. 2. According to Fig. 2 (a), the non-annealed 3D printed material possesses a poor BH characteristic considering that for the same H level, M19 shows B values which are almost double. This means that the electric motor made of the 3D printed material needs a larger current to be able to magnetize the stator and rotor cores to the same level as an M19 based structure. As a result, the magnetic losses increase as well, which is clearly shown in Fig. 2 (c). Also, M19 reveals a larger permeability confirming that the statements in terms of the BH curve and the losses are correct. This poor performance is usually dealt with in the literature by means of annealing up to about 1000 °C or above inside a vacuum furnace. However, the authors have considered the worst case in this study to show how different the materials could be and the impact on the design.

III. Problem Description

In the sequence based TO method, a cell in the discretized design space serves as a pointer which can move about in the design space (Fig. 3), one step at a time, and it is referred to as "the controller". The controller is characterized by its size and the material associated with it. The movement of the controller is decided by choosing from a set of available actions (such as left, right, up or down) and the controller leaves behind a trail

of material as it moves in the design space. So, the goal is to search for the sequence of actions for the controller such that its movements result in an optimized material distribution in the design space. Fig. 3 shows the controller moving in a blank grid-based structure. A controller of size 1 fills the design space as it moves around through one action at a time in a sequential manner. The size of the controller can be modified to suit the problem complexity as a larger size reduces the computation burden of the design optimization problem [9].

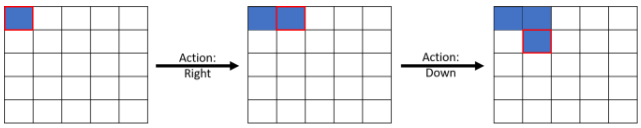

Fig 3. Controller movement

An optimization algorithm is employed to optimize the rotor of a Synchronous Reluctance Motor (SynRM) to maximize the average torque (T_{avg}) experienced. This is done by optimizing the sequence of movements of a controller that consequently results in an optimized material distribution for the rotor of a SynRM. The dimensions of the motor are chosen based on the example considered in [9], as shown in Fig. 4 and listed in Table 1. The optimization problem is formulated in (1) as,

$$\underset{\substack{a_i=\{0,1,2,3\}\\ i=0,1,2,\ldots,m}}{\text{minimize}} \quad T_{avg}(\boldsymbol{a})$$
$$\text{subject to} \quad K1 \le \sum_{j=1}^{n}(p_j = 1) \le K2, \qquad (1)$$

where, $T_{avg}(\boldsymbol{a})$ is the negative magnitude of the average torque experienced by the armature (the negative is imposed to formulate a minimization objective), $\boldsymbol{a}$ is a sequence of actions that governs the movements of the controller in the design space. The material distribution in the design space is represented by a vector p, which is populated by the action vector $\boldsymbol{a}$. The vector p contains the material property of each cell in the discretized design domain, m is the pre-defined sequence length (length of vector $\boldsymbol{a}$) and is representative of the freedom given to the controller to explore the environment, n is the length of the material distribution vector p, and $K1$ & $K2$ are limits on the minimum and maximum number of switched ($p_j: 0 \rightarrow 1$) cells permitted in the design space.

For a SynRM the rotor flux barriers play a vital role in the design optimization of the machine, since they force the main flux through the desired iron paths within a fixed stator geometry. Thus, to improve the performance of SynRM, it is important to optimize the shape of the barrier of the rotor of a SynRM. The objective to be minimized will be $T_{avg}(\boldsymbol{a})$, ithe negative magnitude of the average torque generated by the motor. The material distribution controlled by $\boldsymbol{a}$ is air, which results in a flux barrier in the rotor. The geometry for baseline performance was extracted from MAGNET [13] with the fixed parameters mentioned in Table I and displayed in Fig. 4(a). The baseline SynRM exhibits an average torque of 2.5 N-m. The dimensions of the motor are chosen based on the example considered in [9]. Taking advantage of the symmetry offered by a 4-pole, 3-phase design, only a quarter of the geometry is considered as the design space. The quarter 2-D design space is discretized into 25 (5X5) cells with the initial design filled with iron ($p_i = 1$) and can switch to air ($p_i = 0$), based on the movement of the controller. The cross-section of the discretized design space is shown in Fig 4(b) and the starting position of the controller in Fig 4(c).


Fig. 4. (a) Conventional single barrier SynRM (b) Discretized rotor geometry (c) Controller at start position.

TABLE I
FIXED PARAMETERS

Fixed Parameters	Value	Fixed Parameter	Value
Number of stator slots	24	Number of Poles	4
Stator outer diameter	112 mm	Airgap thickness	0.5 mm
Rotor outer diameter	55 mm	Stack height	50 mm
Rotor inner diameter	16 mm	RMS current density	18 A
Core material	M-19 26 Ga	Barrier material	Air

IV. TOPOLOGY OPTIMIZATION

The sequence based TO method is tested with two significantly different optimization algorithms. First, a Genetic algorithm is used, which is a popular technique in the field of topology optimization. After that a Temporal Difference learning based approach is implemented.

A. Genetic Algorithm

MATLAB's "Global Optimization" [14] is chosen to implement a GA to test the applicability of the proposed environment. Some of the GA's parameters are directly dependent on the TO controller configuration. The number of design variables for the GA is set equal to m. The population size is selected to be a multiple of the number of design variables. A limit on the number of stalled generations is employed to test for convergence. The initial population of the GA is based on a random seeding.

B. Temporal Difference Learning

The key entities of a Markov Decision Process (MDP) are the environment, state, action and reward. The controller interacts with the environment in discrete steps. At each step the controller receives a state from the environment. The state contains sufficient information regarding the current material distribution in the design domain for the controller to interpret and take a rational decision (action). Actions influence the reward as well as the future states and through that future rewards. The algorithm revolves around exploring the environment to learn the transition from one state (s) to another (s'), based on an action (a), ($s \xrightarrow{a} s'$). This transition will result in a reward (r) and the aim is to maximize the reward. The reward in this situation can be directly related to the value of T_{avg}.However, an alternative proxy measure for performance

parameter such as the magnetic field distribution in the air gap can also be used. However, the reward function needs to be scalar. As the controller explores the design space, each state action pair (s, a) has a Value function $(Q(s, a))$ associated with it. The value function is used to account for both the short term and long-term impact of taking an action (a) in a particular state (s). The reward (r) captures the notion of short-term gain. However, for the controller to achieve an optimal geometry, the controller needs to achieve the most reward in all subsequent state trajectories. To complete the description of a finite MDP problem formulation, an episode is defined as the maximum number of steps (m) a controller can take. For a sequence-based controller the environment will be the design space. The state at any step 'n' in an episode is the location of the controller along with the trail of material distribution, as seen in Fig. 3. The set of all possible states is the state space. An action space is the possible movements the controller can make at any step/state. The maximum possible action space a controller can have in the design space (Fig. 3) is four, which are: up, down, left, right, in a global frame of reference. Some states will have a smaller action space due to geometrical constraints. Although the set of states and actions is countable, the value will be very high and is not required for implementation of this algorithm.

TD learning solves for an optimal result by making sequential decisions with a long-term goal to maximize the return $(\sum_1^m r)$. As mentioned earlier, the controller expects a reward after every step and the reward in this problem formulation is the difference of the performance measure between two consecutive steps, that is:

$$r_i = T_{avg}(a_i) - T_{avg}(a_{i-1}); 0 < i < m \qquad (1)$$

Maximizing the rewards over an episode result in minimization of ***f(a)***. The following equation is responsible for updating the Value function $(Q(s, a))$.

$$Q(s, a) \mathrel{+}= lr\left[(r + \max_{a'} Q(s', a')) - Q(s, a)\right] \qquad (2)$$

The above equation is known as the "temporal difference update" and the mathematical proof is described in [9]. Since the TD update equation depends on the maximum action value possible in the next state for all possible actions, the value function of the current state action pair depends on the value of future states. Thus making it possible to account for both short term gain (r) and long term return (through $\max_{a'} Q(s', a')$) .The training process involves hundreds of episodes with value function updates at every step. Once the training is over, the controller has gained sufficient information to traverse through the tree with a greedy policy, which is to rank the possible actions (a) in a state (s) and branch into the option with the highest value function.

An advantage of TD-learning is the freedom of function approximator that can be employed to learn the value function, as long as the value function can be updated incrementally. In this study, a simple tabular method is used for learning the value function. However, much more complex function approximators such as neural networks can also be used. The advantage of tabular function approximator is comparatively faster learning and excellent discriminative property. However, it lacks the generalizability capability for more complex function approximators. As such, two distinct tabular function approximators are used for learning the value function, one for M-19 and other for the printed 3D material.

V. Results and Discussion

For the combination of geometric and excitation parameters mentioned in Table 1, a sequence-based controller is employed on a 5x5 discretized space. The discretized design space (Fig. 4(b)) is filled with non-annealed 3D printed material and the controller is responsible for introducing air (barrier material). A benchmark topology is also created by running the sequence-based controller on a design domain filled with M-19 26 Ga. The optimal design for both the cases is shown in Fig. 5. Both GA and TD learning algorithms converged to the same optimal design and the hyperparameters for the setup of both the algorithms along with the T_{avg} values for the optimal solution are mentioned in Table II.

The optimized geometry obtained with M-19 serves as a benchmark for comparing the performance of the printed high silicon iron. In the second experiment t the design domain is filled with the printed high silicon iron and the controller is responsible for introducing air as the barrier material.

A GA based topological optimization is performed to obtain an optimal flux barrier topology. Fig 5 shows the optimal topologies obtained. With an average torque of 3.40 N-m (M-19 26 Ga) and 3.16 N-m (Non-annealed 3D printed material), the resultant geometry achieves a significant improvement in the average torque as compared to the torque (2.5 N-m) of the conventional design (Fig. 4(a)). It should be noted that the conventional design uses M-19 26 Ga as the iron for rotor material. The average torque (T_{avg}) is obtained through transient 2D Finite Element simulation [7].

TABLE II
Average Torque Results

Environment Type (Genetic Algo)	Design Variables (m)	Pop Size	Stall Genera-tion	Avg Torque [N-m]
5x5 (M-19 26 Ga)	25	25|50	25	3.40
5x5 (3D printed)	25	25|50	25	3.16

Environment Type (TD Learning)	Episode Length (m)	Learning Rate (lr)	Reward Function (r)	Avg Torque [N-m]
5x5 (M-19 26 Ga)	25	0.8	∇T_{avg}	3.40
5x5 (3D printed)	25	0.8	∇T_{avg}	3.16

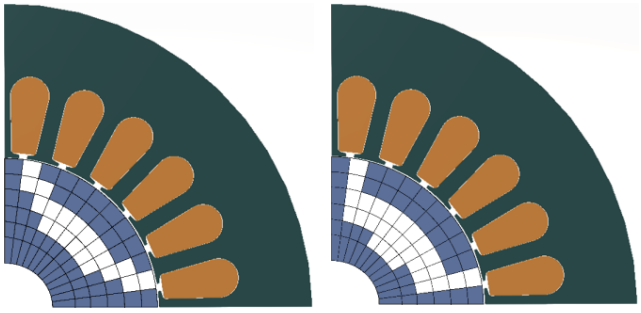

(a) (b)

Fig 5. Optimized geometry for design domain with (a) M-19 26 Ga material, (b) Non-annealed 3D printed material.

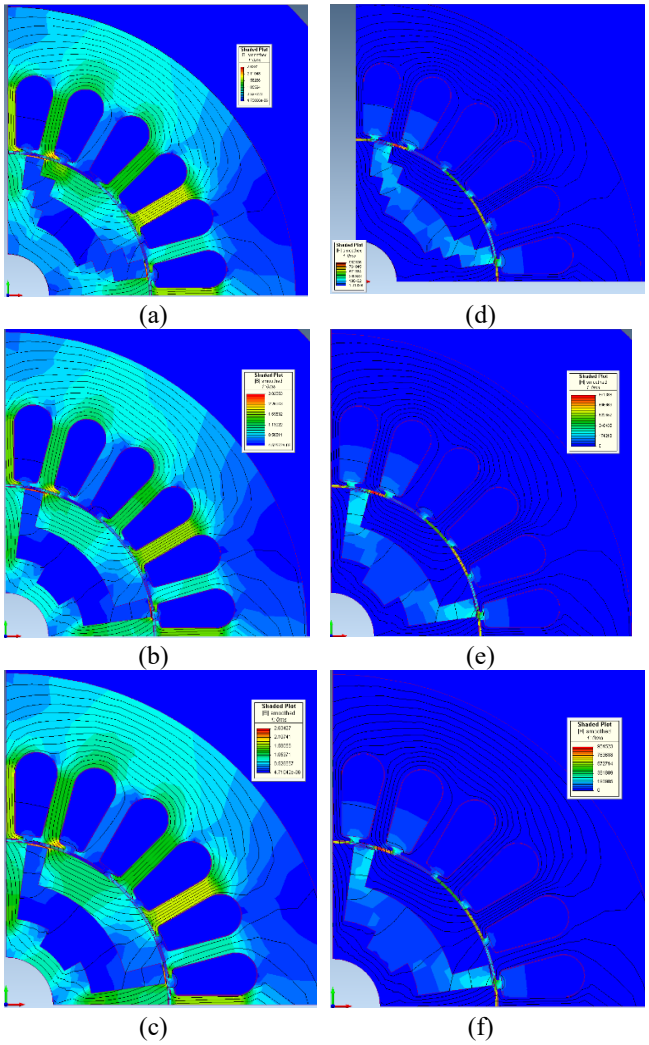

(a) (d)

(b) (e)

(c) (f)

Fig 6. Magnetic flux distribution (B): Optimized geometry for design domain with (a) M-19 26 Ga material (b) Non-annealed 3D printed material (c) Non-annealed 3D printed material replaced with M-19 26 Ga.
Magnetic field strength (H): Optimized geometry for design domain with (a) M-19 26 Ga material (b) Non-annealed 3D printed material (c) Non-annealed 3D printed material replaced with M-19 26 Ga.

With the relatively inferior magnetic properties of the 3D printed material in comparison with M-19 26 Ga, the optimal value of average torque (T_{avg}) differs by a magnitude of 0.24 N-m, a 7% decrease compared to optimal design with M-19 26 Ga. However, the designs are significantly different as can be seen in Fig. 5 and the same can be said for the magnetic flux & field plots in Fig. 6 (a, b, d, e). For a direct comparison between the material M-19 26 Ga and the Non-annealed 3D printed material, the 3D printed material in the optimal design shown in Fig 5(b) is replaced with M-19 26 Ga. With this change in material, the T_{avg} value increases from 3.16 N-m to 3.34 N-m, an increase of 0.18 N-m (approx. 5%). The magnetic flux and field plots with the change of material is shown in Fig. 6 (c) and Fig. 6 (f) respectively.

Furthermore, apart from the advantage of enforced connectivity of material, it is observed that sequence based TO offers computation advantage over the conventional ON/OFF TO method. As can be seen from Table III, the number of FE function evaluations gets reduced by a factor of about 3 for Sequence-based TO with GA and by a factor of 4 when using TD-learning with the Sequence-based TO. This can be attributed to the fact that enforced connectivity reduces the possible solutions in the design space considerably as compared to the ON\OFF methodology. The parameters for both GA and TD-learning were set based on the guidelines provided in [14] and [15] respectively. The computation burden is calculated by the average performance over many independent runs to make a robust comparison. The random seed is the only difference between runs of these algorithms.

The training data for TD-learning is shown in Fig.7 and the convergence criteria are based on a reduction of the standard deviation in the running average, which decreases as the controller exhausts the exploration of the state space and becomes more confident in its value function ($Q(s,a)$).

TABLE III
COMPARISON OF COMPUTATION DEMAND

Environment Type 5x5 (3D printed)	Design Variable/ Eps Length	Pop Size	Stall Gen	FEA function calls
GA – On/Off	25	50	25	12000
GA – Seq based	25	50	25	3800
TD-learning	25	NA	25	3000

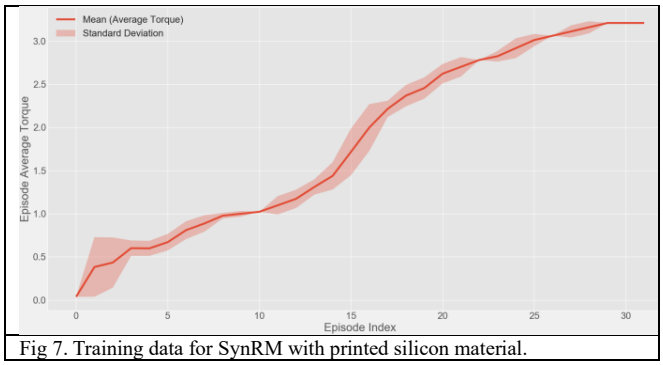

Fig 7. Training data for SynRM with printed silicon material.

VI. CONCLUSION

The topology optimization of a synchronous reluctance motor made of a high-silicon steel material was discussed in this paper. The process consisted of 3D printing the high-silicon steel such that the properties could be measured using a magnetic tester. Next, the results of the measurement were

transferred to the FEA environment in order to enable it to be used to replace the standard steel, M19. The motor topology was then optimized using the GA and reinforcement learning techniques and the average torques of the motors made of the 3D printed material and M19 were compared.

The simulation results reveal that, due to the poor magnetic characteristic of the measured non-annealed high-silicon steel, the corresponding output average torque is less than that of M19. However, it is suggested in the literature that, by means of heat treatment, the characteristics is improved greatly and gets closer to that of the standard materials. This will be the focus of future work, which will also take steps toward testing the optimally designed and 3D printed rotor.

It is noteworthy that, although the non-annealed 3D printed materials possess inferior magnetic properties, the TO approach is able to find the optimal distribution of the materials in the motor structure, that leads to a relatively acceptable average torque level, compared to the standard materials. A more comprehensive work in terms of a multi-objective and multi-physics analysis of 3D printed synchronous reluctance motors will be addressed in future works.

REFERENCES

[1] V. Ghorbanian, A. Salimi and D. A. Lowther, "A Computer-Aided Design Process for Optimizing the Size of Inverter-Fed Permanent Magnet Motors," *IEEE Trans. Ind. Electron.*, vol. 65, no. 2, pp. 1819-1827, Feb. 2018

[2] K. Kellens, R. Mertens, D. Paraskevas, W. Dewulf, and J. R. Duflou, "Environmental Impact of Additive Manufacturing Processes: Does AM Contribute to a More Sustainable Way of Part Manufacturing?," *Procedia CIRP*, vol. 61, no. Section 3, pp. 582–587, 2017.

[3] M. Garibaldi, C. Gerada, I. Ashcroft, and R. Hague, "Free-Form Design of Electrical Machine Rotor Cores for Production Using Additive Manufacturing," *J. Mech. Des.*, vol. 141, no. 7, p. 071401, 2019.

[4] A. Mayr *et al.*, "Electric Motor Production 4.0 - Application Potentials of Industry 4.0 Technologies in the Manufacturing of Electric Motors," *2018 8th Int. Electr. Drives Prod. Conf. EDPC 2018 - Proc.*, 2019.

[5] R. Wrobel and B. C. Mecrow, "A Comprehensive Review of Additive Manufacturing in Construction of Electrical Machines," *IEEE Trans. Energy Convers.*, vol. 1, pp. 15–22, 2020.

[6] F. Wu and A. M. El-refaie, "Towards Fully Additively-Manufactured Permanent Magnet Synchronous Machines : Opportunities and Challenges," pp. 2225–2232, 2019.

[7] S. B. Fuller, E. J. Wilhelm and J. M. Jacobson, "Ink-jet printed nanoparticle microelectromechanical systems," in *Journal of Microelectromechanical Systems*, vol. 11, no. 1, pp. 54-60, Feb. 2002.

[8] M. Garibaldi, I. Ashcroft, M. Simonelli, and R. Hague, "Metallurgy of high-silicon steel parts produced using Selective Laser Melting," *Acta Mater.*, vol. 110, pp. 207–216, 2016.

[9] A. Khan, C. Midha and D. A. Lowther, "Sequence-Based Environment for Topology Optimization," in *IEEE Transactions on Magnetics*, vol. 56, no. 3, pp. 1-4, March 2020, Art no. 7510904.

[10] D. N. Dyck, D. Lowther, "Automated design of magnetic devices by optimizaing material distribution," *IEEE Trans.Magnetics*, vol. 32, no. 3, pp. 1188-1193, 1996.

[11] Renishaw Metal 3D Printer, Available Online: https://www.renishaw.com/en/metal-3d-printing--32084, 2020.

[12] Brockhaus Tester, Available Online: https://brockhaus.com/?lang=en , 2020.

[13] User Manual of MagNet. *Mentor-Infolytica Corporation*. (2018). [Online].Available:https://www.mentor.com/products/mechanical/magnet/magnet/

[14] MathWorks Inc. Global Optimization Toolbox: User's Guide. Accessed: Oct. 3, 2018. [Online] Available: www.mathworks.com

[15] R. S. Sutton, A. G. Barto, "Introduction to reinforcement learning," *MIT press*, Vol 135, Mar 1998.

Sensitivity analysis for automotive EMC measurements using quasistatic Darwin model

Bingler Arnold (1,2), Sándor Bilicz (1) Márk Csörnyei (2)

(1) Department of Broadband Infocommunications and Electromagnetic Theory, Budapest University of Technology and Economics, Budapest, Hungary
(2) PS-PE, Robert Bosch Kft, Budapest, Hungary

Purpose:

The purpose of this paper is performing a global sensitivity analysis for automotive electromagnetic compatibility (EMC) measurements related to the CISPR 25 setup in order to examine the effect of the setup uncertainties on the resonance phenomenon.

Design/methodology/approach:

An integral equation formulation is combined with Darwin model and special Green's functions to model the configuration. The method of Sobol' indices is used to gain sensitivity factors enhanced with a polynomial chaos metamodel.

Findings:

The proposed model resulted in by orders of magnitude lower number of degrees of freedom and runtime compared to popular numerical methods, e.g. finite element method. The result of the sensitivity study is in good agreement with the underlying physical phenomena and improves the understanding of the resonances.

Originality/value:

The proposed method is original in the sense of combining a polynomial chaos metamodel with a low-cost integral equation model to reduce the computational demand for the sensitivity study.

Keywords:

Electromagnetic compatibility, Quasistatic Darwin model, Integral equation, Sensitivity analysis

Published in COMPEL - The international journal for computation and mathematics in electrical and electronic engineering, Vol. 41 No. 3, 2022, ISSN 0332-1649, page 781 - 793

Finite-Element Simulation of Inter-Turn Fault in Switched Reluctance Motors

Jawad Faiz, Shahin Imanzadeh
Center of Excellence on Applied Electromagnetic Systems, School of Electrical and Computer Engineering,
College of Engineering, University of Tehran, Tehran, Iran

Abstract— This paper addresses inter-turn fault in stator winding of switched reluctance motors (SRMs) . The winding of SRMs is concentrated type and such fault is more scalable in it. Finite element-based Maxwell software is used to predict the performance of SRM under the fault. The obtained results show the effect of the fault upon the phase currents, supply current and developed torque. The phase current pattern can be used for the fault detection. The advantage of using the current is that the current sensors fixed in the SRM control system can be used to this fault diagnosis.

***Index Terms*—Switched reluctance motor, inter-turn fault, finite element method, Maxwell software.**

I. INTRODUCTION

To study the behavior of switched reluctance motor (SRM), its analysis under different operating conditions is essential. In some cases, extracting behavior features of SRM is not practically possible. A number of these cases are as follows:

- Studying the behavior of the motor which is not in the prototyping stage.
- Checking motor parameters variations and environmental conditions and their impacts on the behavior of SRM.

Also, in the fault diagnosis process, either it is not practically possible to test a faulty SRM or the test may seriously damage the motor causing high operating cost. In such a case, analytical modeling and/or simulation of the motor can be implemented. Among them, until the motor is analytically investigated and its behavior predicted by a series of linear/non-linear algebraic or differential equations, this procedure is preferred. Normally, this prediction method is very difficult to implement for the dynamic operation if the motor and/or taking into account the nonlinearity of the magnetization characteristic and sometime its accuracy is questionable.

Since a precise and reliable modeling for prediction and investigation of SRM performance is required, simulation of the motor under proposed conditions is essential. FEM is one of the best techniques for SRM modeling. If the FEM is carefully applied, accuracy of the predicted performance is generally close to the experimental results. Both two-dimensional (2D) and three-dimensional (3D) FEM can be applied for simulation of the motor. Obviously, 3D-FEM is superior to 2D-FEM, because it can model the structural curvatures and end-winding effect considering the motor stack length. Besides, 3D-FEM can determine the magnetic field pattern around the SRM frame. Hiwever, 3D-FEM has computational burden and its simulation time is too long. Using some acceptable approcimations, the 2D-FEM can provide reasonable results. Parameters of SRM including magnetic flux density, flux-linkage, windings inductance and output torque can be estimated by both 2D and 3D simulations.

In this paper, first specifications of the proposed SRM are given and simulation results using Ansys Maxwell FE software are employed to investigate its behavior in the healthy case and with inter-turn. Meanwhile, this method contains less simplifying assumptions and higher prediction accuracy. Applying some variations such as load variations and inter-turn fault in SRM will be easier.

II. PROPOSED SRM

SRMs have different configurations, phase numbers and pole numbers, each has its own advantages. Generally, SRMs with low numbers of phase are used over high speed and high number of poles over low speed. Although by increasing the number of phases, the developed torque variations also reduce, and more required electronic components leads to high cost drive.

By increasing the number of poles or phases, the windings space decreases and therefore a more complicated structure such as multi-layer SRMs have been proposed [1]. In addition, higher number of poles leads to a higher stroke frequency as follows:

$$f_1=N_r(rpm)/60 \quad (1)$$

$$f=mf_1 \quad (2)$$

This increases the switching speed leading to more losses. In (1) and (2), f_1, N_r, f and m are the base frequency of the phase current, rotor pole number, strokes per second and number of phases respectively.

The impact nature of these motors is important factor in choosing this motor. The number of strokes per revolution of the motor S is:

$$S=mN_r \quad (3)$$

and the stroke angle ε also is as follows:

$$\varepsilon=2\pi/S=2\pi/mN_r \quad (4)$$

Among these, conventional three-phase SRMs such as 6/4 and 12/8 motors have received more attention because they need less power electronics components and have minimum requirements expected from a motor such as capability of changing the direction of rotation. Four-pole 12/8 SRM are widely used in practice. The reasons include lower torque ripples due to smaller stroke angle, lower copper losses due to shorter end-winding and lower core losses due to a shorter magnetic flux path [2]. Therefore, a 12/8 SRM is

TABLE I
MAIN PARAMETERS OF 12/8 SRM

Parameter	Value
No. of phases	3
Turns per pole	33
Rated voltage (V)	70
Rated power (W)	750
Rated speed (rpm)	1500
Rotor outer diameter (mm)	55
Rotor inner diameter (mm)	30
Stator outer diameter (mm)	102.5
Stator inner diameter (mm)	55.5
Stack length (mm)	80
Stator pole arc (°)	16
Rotor pole arc (°)	14

considered here. Table I gives its main parameters [3].

III. FE SIMULATION OF 12/8 SRM

Simulation of electrical motor is a convenient procedure to address its behavior in different operating points. FE simulation of the motor by enhancing the accuracy makes it possible to apply proposed operating conditions to SRMs. By applying FEM, the structure of SRM is broken into small parts and each part is separately computed to solve electrical and magnetic equations. Ultimately, the final output results including electric current, magnetic flux and torque are determined by sum-up of a set of the results.

To simulate the SRM, first specifications of the motor are entered to the Ansys RMxprt and then the type of material in different parts of the SRM such as iron, copper and shaft are specified. After completing the schematic drawing of the motor, the designed motor is transferred to the Maxwell software. For final simulation of SRM, 2D-FEM model of the motor is employed to shorten the computation time. The reasons are need for investigating different cases and large number of simulations. Fig. 1 presents different parts of the simulated SRM including stator, rotor, shaft and winding of phases. It also shows the arrangement of phases of the stator and direction of their currents to specify magnetic flux pattern. Fig. 2 presents the magnetic fluxes path when phase A is excited at starting it is aligned with the rotor pole.

Fig. 3 and Fig. 4 exhibit inductance of phases against rotor position and flux-linkage versus current and angular position of the rotor in static mode which is a very important in SRM phase excitation and its control.

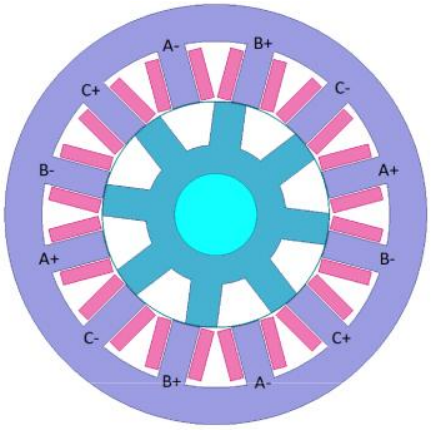

Fig. 1. Simulated SRM by Maxwell software.

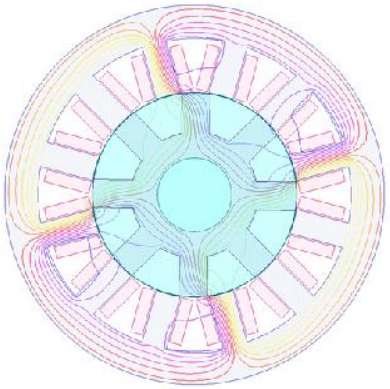

Fig. 2. Magnetic fluxes path caused by excitation of phase A.

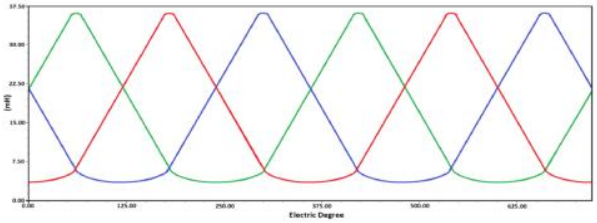

Fig. 3. Phase inductance versus rotor position of simulated SRM.

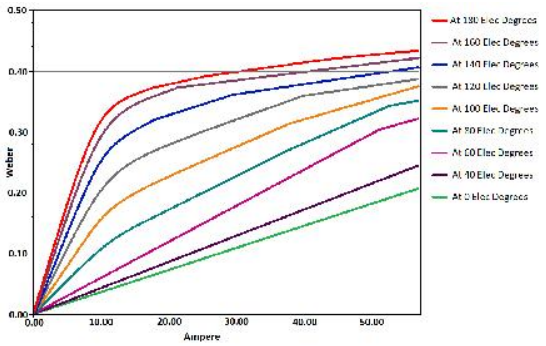

Fig. 4. Flux-linkage versus current of simulated SRM.

III. MESHING OF SRM

Increasing the number of the meshes in solving the proposed problem leads to a higher accuracy. However, this results in a long computational time. Therefore, the attempt has been made to achieve accurate results with minimum number of meshes. So, meshing does not merely implement with a fixed scale but meshes in the airgap region are very fine as seen in Fig. 5.

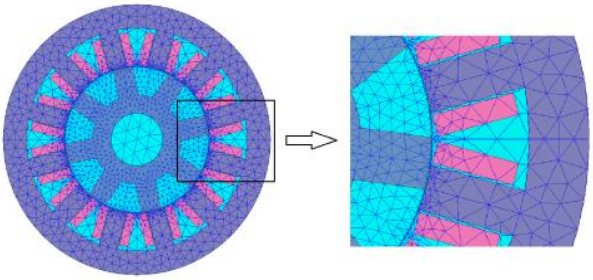

Fig. 5. Meshing of different parts of SRM.

IV. Simulation of Drive of SRM using Ansys TwinBuilder

Linear modeling for control of the SRM drive, which has good dynamic performance, is not sufficient. To excite the phases of the motor and control it, TwinBuilder software is used to design the drive and then communicates with the Maxwell simulated motor. Therefore, by a multi-simulation, the impact of switching of drive on the performance of the motor, effects of magnetic saturation and spatial harmonics of motor upon the drive are fully taken into account. Fig. 6 presents the block diagram of connection of the two softwares indicating the exchange data between two parts.

Fig. 7 shows the complete schematic circuit with its different parts which is described in the next sections.

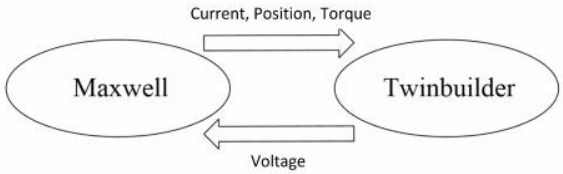

Fig. 6. Block diagram of connection of two TwinBuilder and Maxwell software.

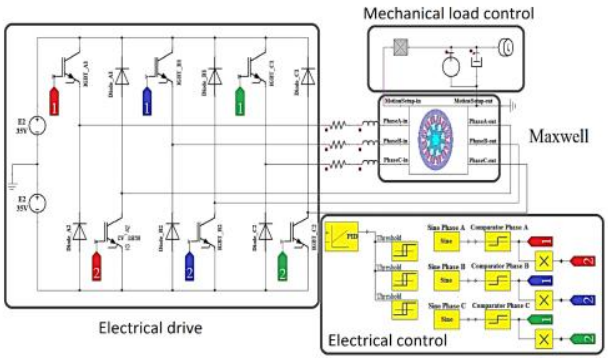

Fig. 7. Simulated drive circuit using TwinBuilder software.

A. Drive Circuit Structure

The SRMs drive must be capable to provide the following two basic requirements:

- Every phase of the motor is independently excited.
- Before entering the generating mode, the phase current tends to zero.

In recent years, drives of SRMs have been widely studied and different models suggested. The differences between these drives include number of electronic components, infallibility level and efficiency. Although asymmetrical half-bridge converter uses more components, it is widely employed due to its capability of full separately excited phases [4]. Therefore, this converter is used here. Fig. 8 presents the current path in one phase of the drive circuit during different switching stages.

B. SRM Control

As shown in Fig. 8, the SRM control consists of:

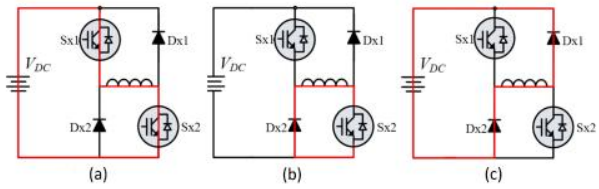

Fig. 8. Circuit of asymmetrical half-bridge converter: (a) phase excitation mode, (b) freewheeling, (c) demagnetization mode.

1) phase excitation mode,
2) freewheeling mode and
3) demagnetization mode.

In the excitation stage, both switches are on and voltage is applied to the phase. In the 2nd mode, one switch is off and voltage is zero and soft switching is applied. In the last mode, both switches are off and current returns to the supply by diodes and a negative voltage is applied to the phase for full quick discharge (demagnetization). The motor is controlled by a speed controller and soft switching current hysteresis controller. Fig. 9 shows the block diagram of the motor control.

To control the SRM, an encoder detects the rotor position and each phase is excited at proper time and position based on the phase inductance diagram and position dictated by the encoder. This prevents entering the machine to the generating mode. The speed is the time derivative of the rotor position and it is compared with the reference speed by a PI control block. The output is the input of the hysteresis block to determine the proper current range. Therefore, soft switching of different phases is determined without considering the rotor position and the phase excited at that instant.

In low speeds range, the freewheeling mode is used to

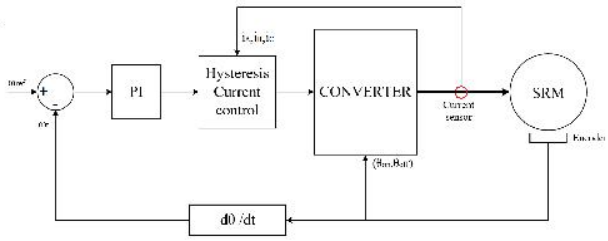

Fig. 9. Block diagram of SRM control.

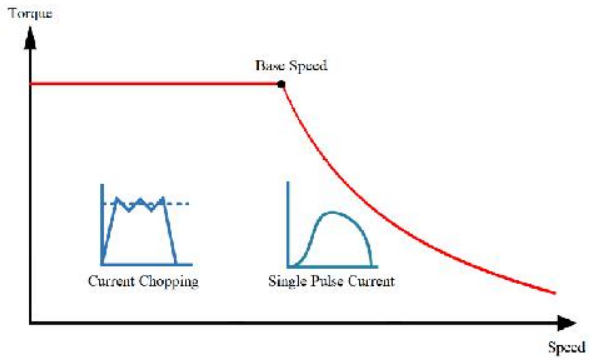

Fig. 10. Torque-speed diagram and switching procedure in SRM over different regions.

control the speed and develop the torque; by rising speed the back-emf increases and required time approaching a higher current will be shorter. Therefore, hysteresis control does not apply and the motor is controlled by single-pulse. Fig. 10 shows the torque-speed diagram over different regions.

VI. Simulation Results for Healthy SRM

After entering the specifications of SRM and drive in two softwares and their connection, the motor is simulated. Considering behavior and output characteristics of the motor in different operating points, control blocks of Twinbuilder software are used and the required parameters such as speed and load of the SRM are adjusted in this software and the results are collected.

Since the switching of drive depends on different operating points, simulation in different points must be done as such that they obtained results provide overall performance of the SRM. Fig. 11 shows the motor phases current of the healthy motor in different operating points. Fig. 12 presents supply current of healthy SRM at full-load.

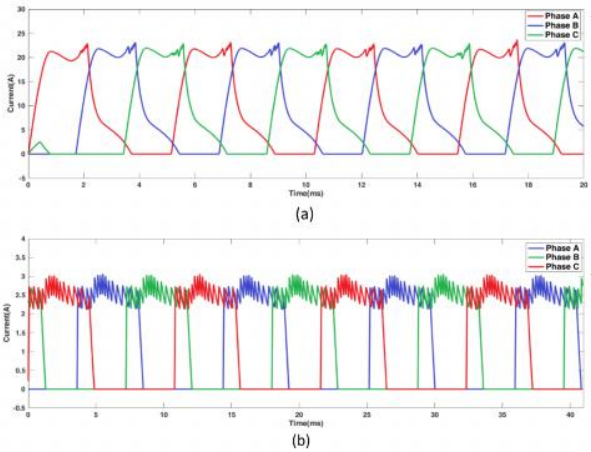

Fig. 11. Phases current waveforms of healthy SRM: (a) full-load at speed of 1500 rpm, (b) no-load at speed 600 rpm.

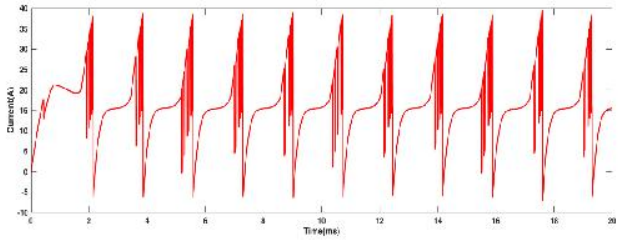

Fig. 12. Supply current of healthy SRM at full-load.

According to these figures, in lower speeds, current is controlled using hysteresis block. As shown in Fig. 10 in this region, switching frequency, proportional with hysteresis adjustments, is higher compared with a high-speed motor. Since the SRM is healthy, there is no asymmetry in the motor phase's currents and supply current. Fig. 13 presents the output torque of motor at full-load and speed of 1500 rpm. The output torque of the SRM is symmetrical; however, torque oscillation is inherent nature of the motor.

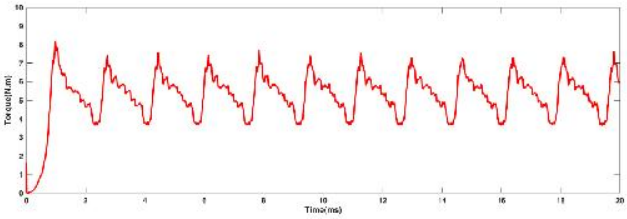

Fig. 13. Output torque of SRM at full-load and speed of 1500 rpm.

6. Inter-turn Fault Simulation of SRM

A. Simulation using Maxwell Software

After inter-turn fault in SRM, each winding is divided to two parts. The 1st part is the healthy coils and 2nd part is the faulty coils or short-circuited coils. They are shown in Fig. 14. The cross-section of the faulty and healthy winding is proportional with their number of turns. The phase A winding divided into two parts which must be properly connected as shown in the next section.

B. Simulation using TwinBuilder

In the healthy SRM, every phase of the motor was considered as a single winding in the TwinBuilder. In the software, phase A winding of the faulty motor is divided into faulty coils and healthy coils. Fig. 15 shows the simulation circuit for inter-turn fault for phase A of the SRM.

The path of the phase A current in healthy SRM has been shown by red color in Fig. 15. The inter-turn fault is applied by connecting switch S. A part of winding is short-circuited and circulating SC current flows in the faulty part and switch.

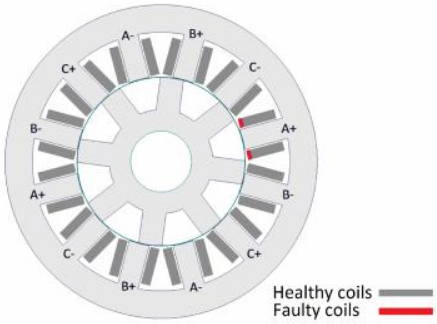

Fig. 14. Simulation of inter-turn fault of winding using Maxwell software.

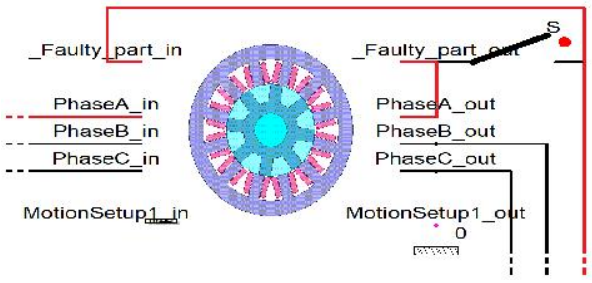

Fig. 15. Simulation circuit for inter-turn fault in phase A of SRM.

7. Simulation Results of Faulty SRM

The results for SC fault in different operating points are obtained. Fig. 16 presents the phases current in the faulty SRM with one-turn SC in two operating points.

Fig. 17 and Fig. 18 present the supply current and output SRM waveforms repectively.

Fig. 18 exhibits the fault effect on the output torque T, estimated by the following equation:

$$T = \sum_{n=1}^{N} \frac{1}{2} i_n^2 \frac{dL_n(i_n^-)}{d^-} \tag{5}$$

where N is the number of phases, i_n is the phase current, $L_n(i_n, \theta)$ is the phase inductance.

The circulating current i_c in the faulty case passing the faulty turn can be obtained as follows:

$$i_c = \frac{-d^{\cdot\cdot} / dt}{r_{pt}} \tag{6}$$

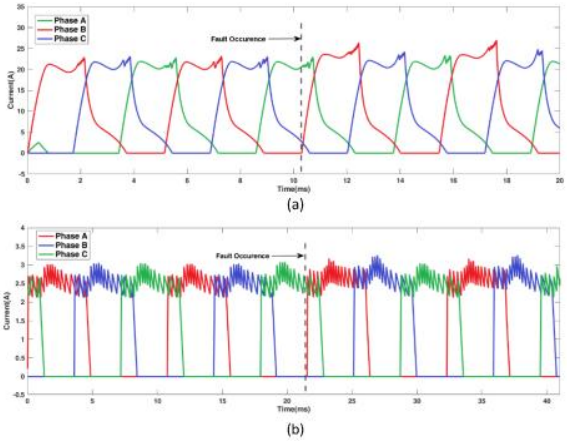

Fig. 16. Phase currents of faulty SRM: (a) full-load at 1500 rpm speed, (b) no-load at 600 rpm.

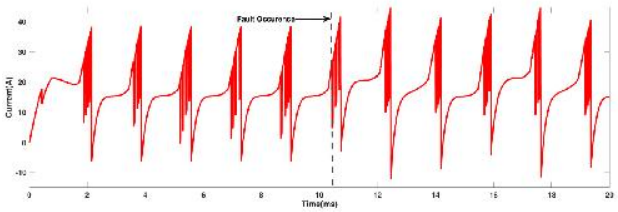

Fig. 17. Supply current of SRM following inter-turn fault in phase A.

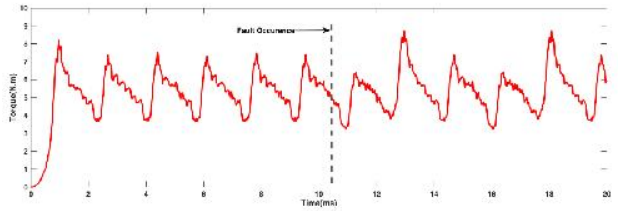

Fig. 18. Output torque of faulty SRM at full-load and speed on 1500 rpm.

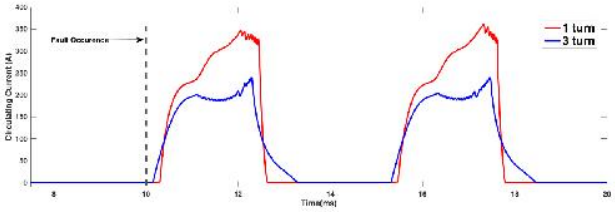

Fig. 19. Circulating current waveform in SC coils.

where r_{pt} is the resistance/turn of the winding. The current is limited only by the resistance of the faulty turn. A low number of SC turns leads to a higher current. Fig. 19 presents the current waveform which indicates that the peak current is very higher than the peak current of the phase at its operating point (20 A). This high current causes temperature rise which may damage the winding insulation and increase the number of faulty turns.

8. Conclusion

To analyze the performance of the SRM under inter-turn, it was simulated by FE Ansys Maxwell software. The simulation results indicated the serious fault impact on the phase currents, supply current and torque. It was shown that the phase current pattern can be used for fault diagnosis. The advantage of using the current waveform is that there is no need to employ an additional sensor, because the current sensors of the control system of the SRM is also useable for fault detection.

References

[1] N. Zabihi, and R. Gouws, “A review on switched reluctance machines for electric vehicles”, IEEE 25th International Symposium on Industrial Electronics (ISIE), 8-10 June 2016, Santa Clara, CA, USA.

[2] T. J. E. Miller, “Electric Control of Switched reluctance Machines,” Newnes Press, UK, 2001.

[3] C. Gan, J. H. Wu, N. Wang, Y. H. Hu, W. P. Cao, and S. Y. Yang, “Independent Current Control of Dual Parallel SRM Drive Using a Public Current Sensor”, *IEEE/ASME Trans. Mechatronics*, vol. 22, no. 1, pp. 392-401, Feb. 2017.

[4] O. Ellabban, and H. Abu-Rub, “Switched Reluctance Motor Converter Topologies: A review”, IEEE International Conference on Industrial Technology (ICIT), 26 Feb. -1 March 2014, Busan, South Korea..

Influence of soil model simplifications on the surface potential distribution of earthing systems

Benjamin Jauk*, Robert Schürhuber*, and Katrin Friedl*

*Graz University of Technology, Institute of Electrical Power Systems, Inffeldgasse 18/I, A-8010 Graz
E-mail: benjamin.jauk@tugraz.at

***Abstract*—The soil resistivity is a main parameter in the dimensioning process of earthing systems. For analytical calculations in typical earthing systems evaluation software, the soil is considered uniform or layered, but in reality it has an arbitrary shaped resistivity distribution. In order to get the resistivity distribution an Electrical Resistivity Tomography (ERT) of a test area is performed, using Wenner's array configuration. The found apparent resistivity data is then used as an input parameter for the inversion modelling process to find the resistivity distribution of the test area. The goal is to compare the effects on the surface potential distribution on different simplified soil models of this reference model. The surface potential distribution of two half spherical shaped earthing electrodes is analysed using the finite element method (FEM) software ANSYS Maxwell 3D.**
Using the minimum apparent resistivity for a homogeneous soil and the layered model showed the smallest deviation of the surface potential distribution, compared to the reference model.
Further investigations will show the effect of different soil structures on the behaviour of the earthing system.

***Index Terms*—Arbitrary Soil Resistivity Distribution, Earthing System, FEM, Pseudo 3D Soil Resistivity Measurement**

I. Introduction

Earthing systems play an essential role in personal safety and power systems reliability. If fault currents occur, earthing systems have to be capable of distributing these currents into ground and ensure that no harmful potentials (e.g. touch voltage, step voltage) arise, which will cause hazardous body currents. Limits are stated in international and national requirements, e.g. [7], [9]. One of the main factors which influences the quality of the earthing system is the resistivity of soil. The dependency of this value according to the moisture, chemical content and temperature is for example shown in [7]. Due to this, the behaviour of the soil is not constant over time and unique to its location.

In earthing systems analysing tools, homogeneous or layered soil is often assumed [7], [8]. But, natural soil is neither homogeneous nor layered. The resistivity distribution is arbitrary in shape. Using a homogeneous or layered model provides the possibility to use analytical methods for calculation. For arbitrary resistivity distributed soil models the complexity is raising and numerical methods are preferred for calculation.

For geophysical surveys different measuring methods are used for detailed ground investigations, namely:

- Electrical resistivity methods
- Electromagnetic methods
- Seismic methods

In this work, Wenner's method [4], [6], an electrical resistivity method, is used to measure a test area. As shown in Fig. 1, the array uses four electrodes per measurement. Two for current injection and two for potential measurement. In electrical power engineering most of the measurements are performed at specific points with different electrodes spacing, where in ERT all the electrodes are placed before the measurement and the measurement unit starts an automatic measuring routine. This detailed soil investigations can provide the information for building this arbitrary soil model. The reference model is built with the measured data by solving this inverse problem.

To analyse the influence on the surface potential distribution of an embedded earthing system, several simplified soil models of this test area are built. The earthing system consists of two half-spherical shaped electrodes.

For the simulation the FEM analysis software ANSYS Maxwell 3D is used, applying only a static current field.

II. Measurement

A. Theory

The partial derivative equation (PDE) for the static current field is:

$$\vec{\nabla} \cdot \left(\frac{1}{\rho} \vec{\nabla} \varphi \right) = 0 \tag{1}$$

Where ρ is the resistivity, φ is the electric scalar potential.

When assuming a spherical shaped electrode with isolated supply, where the excitation current enters this problem region, the current I is:

$$I = \int_{\Gamma} \vec{J} \cdot d\vec{\Gamma} = \frac{J}{4r^2\pi} \tag{2}$$

Where $\vec{J}$ is the current density vector, $\vec{\Gamma}$ the surface vector and r is the radial distance.

The electric scalar potential in infinite half space comes to:

$$\varphi(r) = \frac{\rho I}{2r\pi} \tag{3}$$

By adding the sink, it follows by the principle of superposition:

$$\varphi(r) = \frac{\rho I}{2\pi}\left(\frac{1}{r_{\mathrm{C1}}} - \frac{1}{r_{\mathrm{C2}}}\right) \tag{4}$$

Where r_{C1} is the distance to source and r_{C2} is the distance to sink.

In ERT four electrodes are used and the potential between the two potential electrodes is [1]:

$$U_{\mathrm{P}} = \frac{\rho_{\mathrm{a}} I_{\mathrm{C}}}{2\pi}\left(\frac{1}{r_{\mathrm{C1P1}}} - \frac{1}{r_{\mathrm{C2P1}}} - \frac{1}{r_{\mathrm{C1P2}}} + \frac{1}{r_{\mathrm{C2P2}}}\right) \tag{5}$$

Where U_{P} is the electrical potential difference between the "P" electrodes, I_{C} is the current injected into the "C1" electrode, ρ_{a} is the apparent resistivity and r_{CiPj} is the distance between "Ci" and "Pj" electrode, with $\{\mathrm{i},\mathrm{j}\} = \{1, 2\}$.

Since, all distances between the electrodes of a Wenner array are equal to a, (5) can be rewritten to:

$$U_{\mathrm{P}} = \frac{\rho_{\mathrm{a}} I_{\mathrm{C}}}{2a\pi} \tag{6}$$

B. Method

For the measurement of soil characteristics a geophysical earth resistivity measurement unit is used to measure the apparent resistivity of the test area. This area is investigated using six survey lines with 24 electrodes each and a distance of $a = 3\,\mathrm{m}$. The distance between the survey lines is also $3\,\mathrm{m}$. The used electrode configuration is Wenner-α, as shown in Fig. 1.

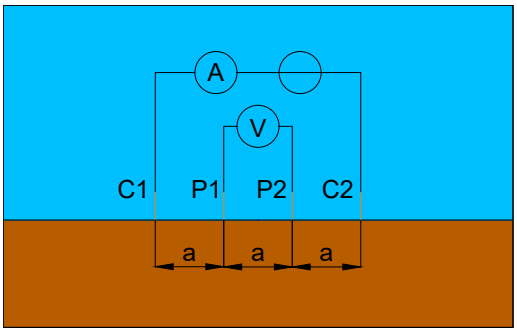

Fig. 1: Wenner electrode configuration [11]

To get the data point deeper in the soil, the distance between the used electrodes for measuring is increased. For the first depth level, the distance between the electrodes is equal to a, the second level is achieved by a distance equal to $2a$, for the third level: $3a$, and so on. This switching of the electrodes is done in an automatic manner directly by the measuring unit. The measurement is performed line by line, so there is only information of the soil resistivity in the direction of the survey line. According to [1] this is called a Pseudo 3D investigation, category 4. The obtained data points are corrected by the median value of the sensitivity function of the Wenner electrode configuration [1], [2].

C. Results

Fig. 2 depicts the 3D apparent resistivity distribution, already with corrected depth values. The "V" shape in X direction is caused by the fact, that the data point is in the middle of the used electrodes to generate this point. So the wider the electrodes distance, the less data points are available for the inversion.

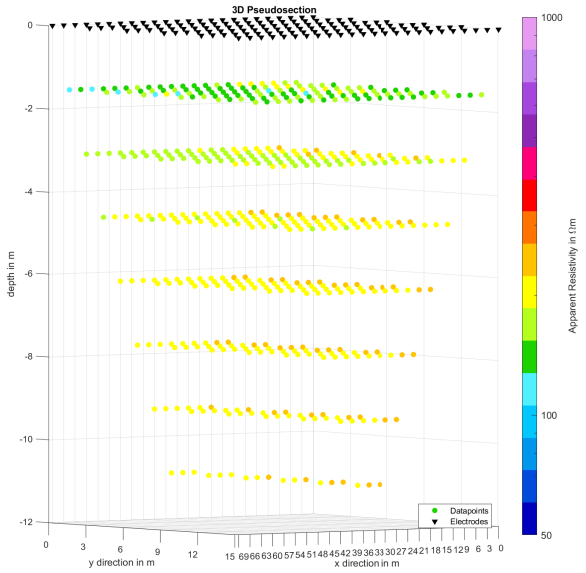

Fig. 2: 3D Apparent Resistivity Data

III. Soil Modelling

There are different soil models which can be used, as illustrated in Fig. 3-5. For earthing system design often a homogeneous (Fig. 3) or layered model (Fig. 4) are used. The current distribution in these models can be both, calculated in an analytical manner or simulated using a FEM approach. Where for arbitrary shaped resistivity distributed soil models (Fig. 5) only numerical approaches can be practically used.

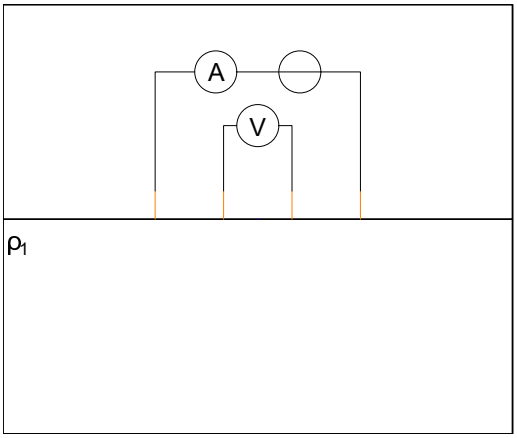

Fig. 3: Homogeneous soil model [11]

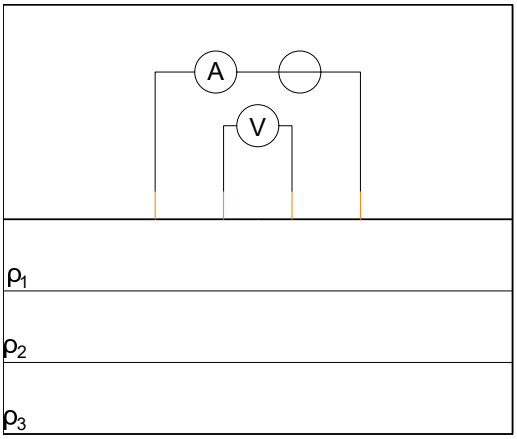

Fig. 4: Horizontal layered soil model [11]

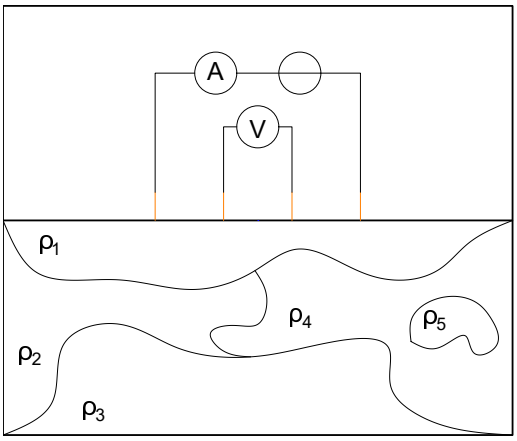

Fig. 5: Arbitrary soil model [11]

A. Theory

Since there is only observed data available for the soil model, an inversion is proceeded to find the "real" resistivity distribution. The used software minimises the error between the observed and model response data, with the following expression [1], [3]:

$$\vec{q}_{k+1} = \vec{q}_k + \left(\mathbf{J^T J} + \lambda \mathbf{F}\right)^{-1} \left(\mathbf{J^T}\vec{g} - \lambda \mathbf{F}\vec{q_k}\right) \quad (7)$$

Where $\vec{q}$ is the model parameter vector, $\mathbf{J}$ is the Jacobian, λ is the damping factor, $\mathbf{F}$ is the filter matrix and $\vec{g}$ is the discrepancy vector.

B. Method

For this inversion, the geophysical software RES3DINV [3] is used. The following parameters are set to solve the inversion:

- Type of forward modelling: FEM
- Horizontal Mesh Size: 4nodes
- Vertical Mesh Size: Ultra-Fine (4nodes)
- Mesh Boundary: medium extended
- Error Change convergence: $2\,\%$
- Thickness of first layer: $1.35\,\mathrm{m}$

The following, different, models are analysed:

1) Inversion model resistivity
   This soil model is representing the "real" soil resistivity distribution. Meaning it is the reference model with the closest match to the investigated area.
2) Layered model
   Layered soil model which consists only of two layers, the resistivity values are calculated with the Soil Resistivity Analysis (SRA) tool from XGSLab™ [5]. XGSLab™ uses the trust region method (TRM) to solve the squared error function and also weights the input parameters [5].
3) Apparent resistivity Average
   Homogeneous soil model with the average of all apparent resistivity values.
4) Apparent resistivity Minimum
   Homogeneous soil model representing the lower end of the apparent resistivity range.
5) Apparent resistivity Maximum
   Homogeneous soil model representing the upper end of the apparent resistivity range.

The layered and homogeneous average soil model are calculated as suggested in IEEE Std. 80 [7]. Both, the homogeneous Minimum and Maximum models represent the end of the measurement values. If only single measurements, or in an extreme case, only one measurement is performed, it would be also possible to get one of these values.

C. Results

Fig. 6 depicts the inversion result with the resistivity values. The "V" shape isn't present anymore, the missing points are calculated by the inversion software. The different depth values are caused by the chosen software parameters.

The finite cubes, as given in Fig. 7, which represent the smallest volume in this soil model, are homogeneous isotropic in their resistivity distribution.

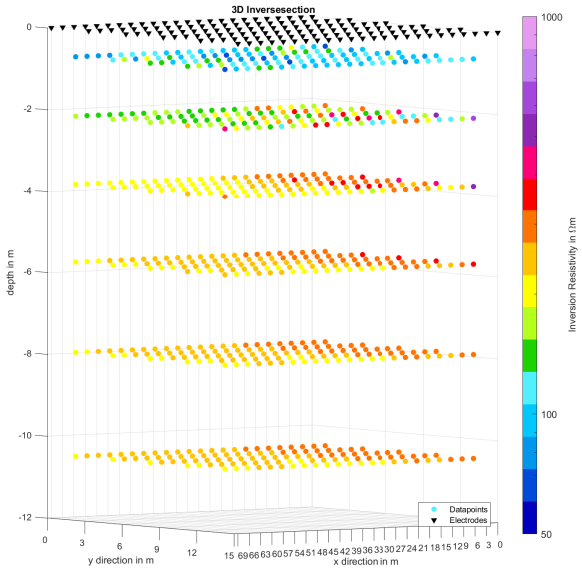

Fig. 6: 3D Inversion Model

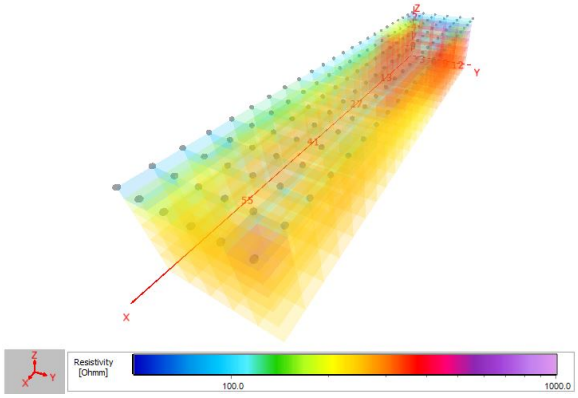

Fig. 7: 3D Inversion Model - cubes in transparent view

IV. FEM Simulation

A. Method

The FEM simulation is carried out with ANSYS Maxwell 3D in DC Conduction solution type. The modelled earthing system consists of two half-spherical shaped electrodes with $r = 0.5\,\mathrm{m}$. The electrodes are placed at the following positions $(X/Y/Z)$ and the injected excitation current is $10\,\mathrm{A}$:

- Source: $34.5\,\mathrm{m}$ / $7.5\,\mathrm{m}$ / $0\,\mathrm{m}$
- Sink: $334.5\,\mathrm{m}$ / $7.5\,\mathrm{m}$ / $0\,\mathrm{m}$

The analysed soil model is embedded in an volume with homogeneous soil with a resistivity of $100\,\Omega\mathrm{m}$. The edges of the surrounding are $400\,\mathrm{m}$ apart from the soil model to reduce the effects of the boundary and the electrodes on each other.

As shown in Fig. 8 the excitation current flows from the electrode in the middle of the soil model through the surrounding volume in Y direction to the sink electrode, $300\,\mathrm{m}$ apart. The surface potential distribution is analysed

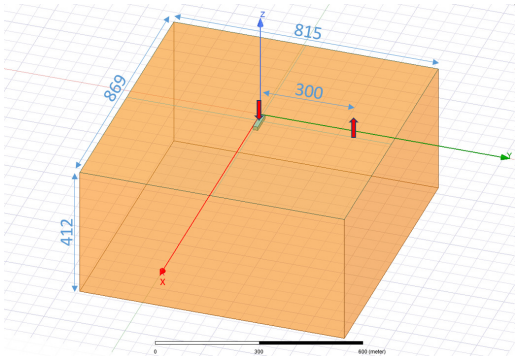

(a)

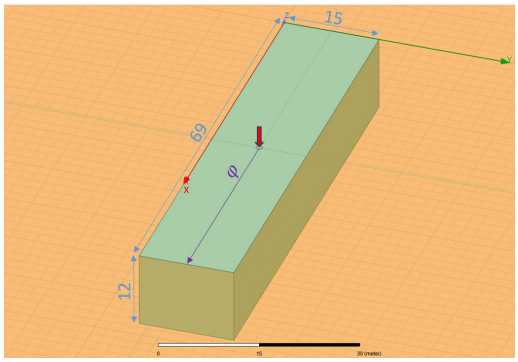

(b)

Fig. 8: (a) Overview of the FEM model, (b) Detailed view on the FEM model

in X direction, orthogonal to the current flow. The surface potential distribution is plotted from the electrode to the end of the soil model.

The error E of the surface potential φ related to the Inversion model is calculated as follows:

$$E = 100\,\% \cdot \frac{\varphi_{\mathrm{i}}(x) - \varphi_{\mathrm{Inv}}(x)}{U_{\mathrm{E,Inv}}} \tag{8}$$

Where $\varphi_{\mathrm{i}}(x)$ is the surface potential distribution of the i^{th} model, $\varphi_{\mathrm{Inv}}(x)$ is the surface potential from the inversion model and $U_{\mathrm{E,Inv}}$ is the earth potential rise (EPR) of the inversion model.

To be able to compare the error, the quantity "Area Under the Curve (AUC)" is introduced. AUC is calculated with trapezoidal numerical integration. It is used to determine the deviation to the reference model. The value doesn't take into account, if the curve is positive or negative varied to the reference model.

Before analysing the models with the FEM tool ANSYS Maxwell 3D, a comparison between an analytical calculation and the FEM simulation is made. Therefore a homogeneous model with a resistivity $\rho = 100\,\Omega\mathrm{m}$ is built. The result is shown in Fig. 9. It is noticeable that there is a deviation between the surface potential distribution of the analytical and the simulated solution, shown by the solid and dash-dotted lines. The reason for this is, that the analytical expression from (4) is valid for infinite half space, but the simulated model is only

69 m x 15 m x 12 m in dimension. When enlarging the soil model dimensions it can be seen, that the simulated solution fits better to the analytical solution, shown by the dashed line.

For this reason, the soil model is embedded in the surrounding homogeneous soil.

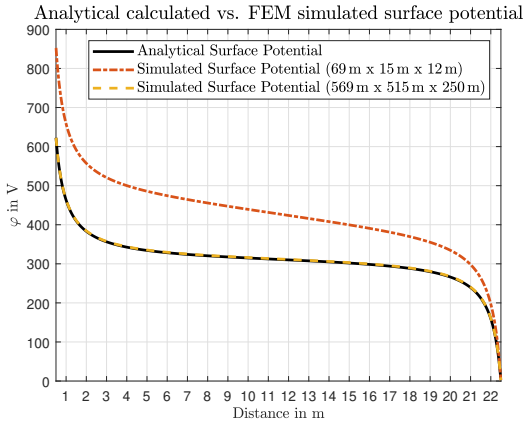

Fig. 9: Simulated vs. analytical solved solution [11]

B. Results

Fig. 10 depicts the surface potential distribution along the evaluated direction. The different EPR's can be already seen. More in detail, Fig. 11 shows the error related to the inversion model. It can be seen, that the homogeneous model with the minimum soil resistivity value of the measurement shows the closest match to the reference model. The layered model has an error of around 40 % to the EPR of the reference model. Also by comparing the AUC, as shown in Tab. II, it can be seen, that the soil model with the minimum resistivity value has also a better match with the reference model than the other soil models.

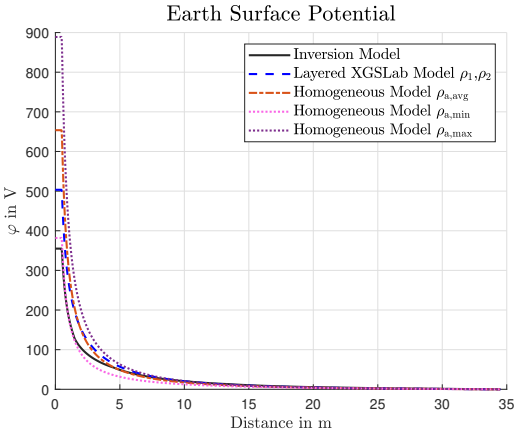

(a)

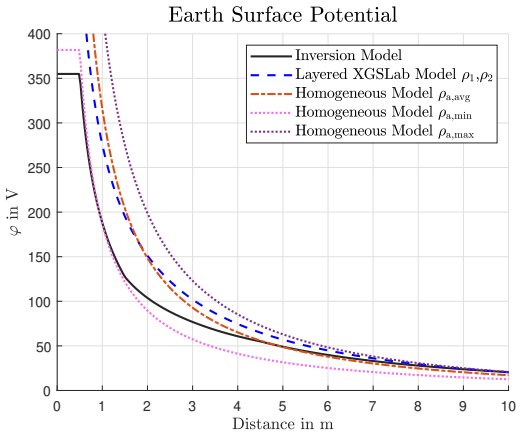

(b)

Fig. 10: (a) Total U_{E} along the line, (b) Detailed view on U_{E}

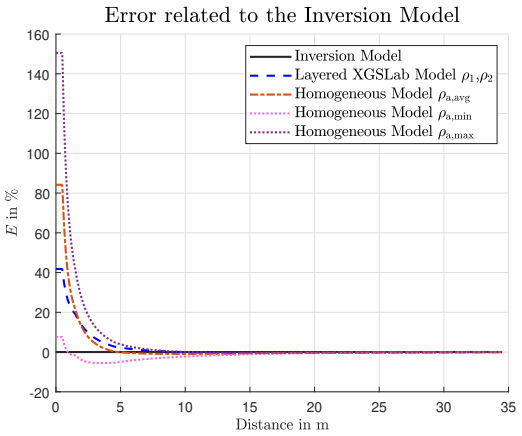

(a)

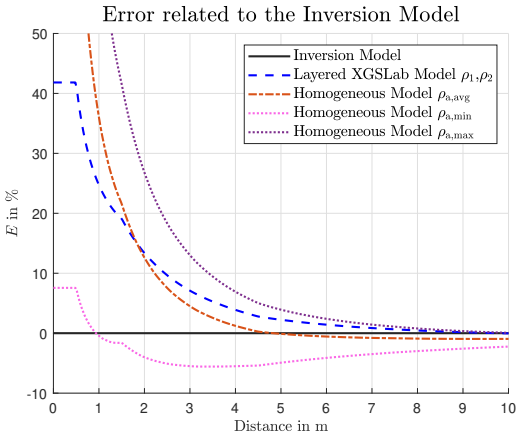

(b)

Fig. 11: (a) Total E along the line, (b) Detailed view on E

TABLE I: Resistivity values for the layered and homogeneous soil models

Simulated model	ρ Ωm
XGSLab Layered	137 (1 m) 283 (11 m)
Homogeneous avg.	211
Homogeneous min.	122
Homogeneous max.	287

TABLE II: U_{E}, E and AUC for simulated cases

Simulated model	U_{E} V	E %	AUC -
Inversion	355	0	0
XGSLab Layered	504	41.8	0.82
Homogeneous avg.	654	84.2	1.15
Homogeneous min.	382	7.6	0.55
Homogeneous max.	889	150	2.13

V. Conclusion

The authors showed the possibility to use an applied geophysical application for earthing system design. This procedure gives new opportunities to show the behaviour of the earthing system on different soil structures. It was shown for a very simple electrode configuration, that there are significant differences between the earth surface potential distribution of the analysed models.

It is shown that using the minimum measured resistivity value showed the best match with the reference model for this test area, according to AUC. The error in this model is negative for a majority of the progression. This is crucial for safety considerations, because the surface potential distribution is expected lower than it really would be. The AUC value is only for comparing the deviation of the different soil models suitable and can not be used for safety considerations. Another quantitative value has to be stated.

This work only showed the deviation between the reference soil model and the other, simplified soil models. But, there is no information about the deviation between the reference model and the real resistivity distribution of the test area.

VI. Outlook

More fundamental research in this field is planned. This includes generating a synthetic soil model to show also the deviation of the reference model which is generated by the inversion process. Also more modelling work to evaluate the different impacts on the behaviour of the soil model, like the temperature and moisture content is planned. Further investigations of the whole process, from the measurement, through the inversion, to the FEM simulation, with its error propagation is currently in the planning process.

Since, most of the electrical power systems are not working with direct current, the simulation and measurement shall use alternating current as well.

In addition to this planned work, a key question is the influence of the soil model on the overall risk, since the European standard EN 50522 [9] defines only limiting values for worst case assumptions. Quantified risk analysis is only mentioned in British annex of EN 50522 [9] and CIGRE Technical Brochure 749 [10].

References

[1] M. H. Loke, “Tutorial: 2-D and 3-D electrical imaging surveys”, Loke Oct. 2019

[2] A. Roy and A. Apparao, “Depth of Investigation in Direct Current Methods”, GEOPHYSICS, Vol. 36, No. 5, Oct. 1971

[3] Geotomo Software Sdn Bhd, Res3DInv ‘3-D Resistivity Inversion Modelling Program’

[4] A. Eriksen J. Milsom, “Field Geophysics, Fourth Edition”, John Wiley and Sons Ltd. 2011

[5] SINT srl, XGSLab^{TM} ‘Electromagnetic Simulation for Power, Grounding and Lightning Protection Systems’

[6] F. Wenner, ”A Method of Measuring Earth Resistivity”, in Bulletin of the Bureau of Standards, Jul. 1915. [Online].

[7] IEEE Guide for Safety in AC Substation Grounding, IEEE Std. 80-2013, 2013

[8] IEEE Guide for Measuring Earth Resistivity, Ground Impedance, and Earth Surface Potentials of a Grounding System, IEEE Std. 81-2012, 2012

[9] Earthing of power installations exceeding 1 kV a.c., ÖVE/ÖNORM EN 50522, 2011

[10] CIGRE Technical Brochure B3/CIRED Substation earthing system design optimisation through the application of quantified risk analysis, Reference 749, 2018

[11] B. Jauk, “Influence of arbitrary resistivity distribution of ground on the behaviour of the surface potential”, Master Thesis, Institute of Electrical Power Systems, Graz University of Technology, Graz, Austria, 2020.

Multiphysics Models of Innovative Actuators of LV and MV Vacuum Circuit Breakers and Contactors

[1]Yevgen I. Bajda, [2]Markus Clemens, [1]Michael G. Pantelyat,
[1]Olena G. Korol, [1]Mykola A. Lelyuk and [1]Serhii V. Vyrovets
[1]Department for Electrical Apparatus, National Technical University "Kharkiv Polytechnic Institute",
Kyrpychova Str. 2, UA-61002 Kharkiv, Ukraine
[2]Chair of Electromagnetic Theory, University of Wuppertal,
Rainer-Gruenter-Str. 21, D-42119 Wuppertal, Germany
E-mail: baida.kpi@gmail.com, clemens@uni-wuppertal.de, m150462@yahoo.com

Abstract—**The paper is devoted to the development and comparative analysis of various techniques for calculating the dynamic characteristics of driving electromagnets of electrical devices: by the method of "electrical analogy" based on solving a system of ordinary differential equations for magnetic, electrical and mechanical circuits with lumped parameters; using the "hybrid" method which is based on the static calculation of electromagnets' magnetic field by the Finite Element Method with the subsequent use of the obtained data to calculate the dynamics; by the "pure" transient field-circuit calculation of dynamics in axisymmetrical formulation. The paper provides examples of calculation of LV and MV vacuum circuit breakers' and contactors' electromagnets by each of these techniques, presents a mathematical description of the methods and the numerical results obtained. The advantages and disadvantages of each of the considered methods are analyzed.**

***Index Terms*—Actuator, circuit breaker, computer simulation, multiphysics.**

I. Introduction

The rapid development of innovative technologies in recent years also affects the design and production as electrical apparatus and also manifested itself in the emergence of new apparatus, such as vacuum contactors, vacuum circuit breakers, etc. Actuators based on DC electromagnets are used as driving elements in such devices as they are more reliable and durable. Such electromagnets include forced electromagnetic systems, as well as monostable and bistable polarized and non-polarized electromagnets [1-7].

When designing such devices, variant and optimization calculations of both static and dynamic characteristics of electromagnetic mechanisms are required, which are carried out on the basis of appropriate mathematical models. There are several techniques for calculating the characteristics of electromagnetic mechanisms [8-12], such as e.g.: 1) the method of "electrical analogy" using Kirchhoff lumped parameter models; 2) the method of integral equations; 3) volume discretization type methods such as e.g. the Finite Difference Method, the Finite Element Method, the Finite Volume Method, the Finite Integration Technique and related techniques using primal-dual grid pairs as e.g. the Cell method or the Method of Generalized Finite Differences; 4) combined or "hybrid" methods. Another class of asymptotic techniques for the description of electromagnetic field distributions such as e.g. the ray tracing method is rather reserved for problems at (near-) optical frequencies.

The goal of this paper is investigation, application and comparative analysis of various techniques for calculating electromagnets of LV and MV vacuum circuit breakers and contactors.

II. A Method of "Electrical Analogy" using Lumped Parameter and Circuit Models

Forced electromagnetic systems which include the electromagnet itself and the control circuit are widely used in LV, MV and HV electrical devices, in particular in vacuum contactors. A feature of such systems is that in the process of operation (closing-opening of the contacts of the main circuit), the connection circuit of the electromagnet windings changes, and also changes occur

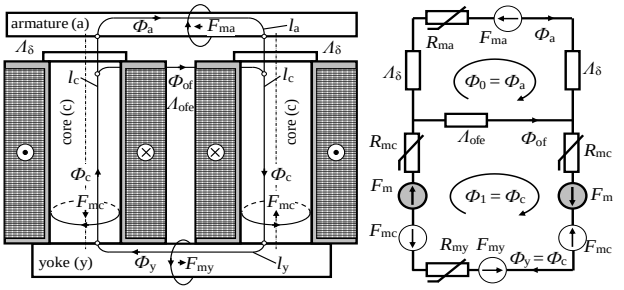

Figure 1: A sketch of a double-rod electromagnet and its equivalent circuit, where Φ_i are the magnetic fluxes of the armature and cores; F_m is the magnetomotive force (MMF) of the coils; R_m is the magnetic resistance of the corresponding section of the magnetic circuit; F_{mc},F_{ma} are the "eddy" counter-MMFs; Λ_δ are the magnetic conductivities of air gaps; Λ_{ofe} is the magnetic conductivity of scattering fluxes.

in the electrical control circuit. In addition, in the process of operation, the opposing force which has a stepwise character and the mass of the moving parts change, too. All these changes must be taken into account together with the equations describing the magnetic processes in the magnetic circuit. Consequently, the system of equations describing the dynamics of the electromagnet must include the equations of the electric control circuit, the equations of motion of the moving masses reduced to the armature of the electromagnet, and the equations of the electromagnetic field. A rigorous solution of the problem of calculating the electromagnetic field of an electromagnet is based on Maxwell equations. However, the implementation of such methods in the case of calculating 3D models encounters significant difficulties. In cases where the air gaps are small compared to the dimensions of the magnetic circuit, and the design of the magnetic system is relatively simple, it is possible to use established, simple modeling techniques, supplementing them with new capabilities of modern computer codes. One of such techniques is the method of "electrical analogy", the essence of which lies in the fact that the magnetic system is "divided" into small sections, within which the magnetic parameters of the circuit do not change. The change in magnetic parameters (magnetic resistance, magnetomotive force, magnetic flux) occurs

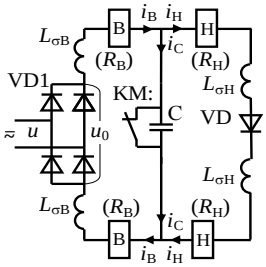

Figure 2: Forced control circuit used in LV and MV vacuum contactors, where u is the instantaneous voltage value at the bridge input; u_0 is the voltage at the bridge output.

during the transition from section to section. As an example, the model of the forced electromagnet of the vacuum contactor is presented in Fig. 1. As a control circuit for the coils, a well-known one that is most often used for forced control of electromagnets (see Fig. 2) is chosen.

The circuit can operate from both a DC and an AC voltage source. The operation of the circuit consists in the fact that when the contactor is triggered, the contacts KM open, connecting in series to the booster (B) winding the holding (H) one. Here, the current of the windings decreases to the value admissible under the heating conditions.

The kinematic diagram is a classic kinematic one of a contactor with a stepwise opposing characteristic and a changing mass of moving bodies depending on the armature stroke.

Therefore, the calculation differential equations of the dynamics of a forced electromagnetic system can be written as follows:

$$-G_a \cdot \frac{\mathrm{d}\Phi_0}{\mathrm{d}t} = H(\Phi_0 / S_a) \cdot l_a + \frac{2 \cdot \Phi_2}{\Lambda_\delta} - (\Phi_1 - \Phi_0) / \Lambda_{ofe};$$

$$2 \cdot i_B \cdot w_B + 2 \cdot i_H \cdot w_H - (2 \cdot G_c + G_y) \cdot \frac{\mathrm{d}\Phi_1}{\mathrm{d}t} = \quad (1)$$

$$= H(\Phi_1 / S_y) \cdot l_y + 2 \cdot H(\Phi_1 / S_c) \cdot l_c + (\Phi_1 - \Phi_0) / \Lambda_{ofe},$$

where G is the equivalent magnetic conductivity; $H(B)$ is the magnetization curve; S are the cross-sections of the corresponding sections of the magnetic circuit; l is the lengths of the sections;

$$u_0 = 2 \cdot R_B \cdot i_B + 2 \cdot L_{\sigma B} \cdot \frac{\mathrm{d}i_B}{\mathrm{d}t} + 2 \cdot w_B \cdot \frac{\mathrm{d}\Phi_0}{\mathrm{d}t} + u_C; \quad (2)$$

$$u_C = 2 \cdot R_H \cdot i_H + 2 \cdot L_{\sigma H} \cdot \frac{\mathrm{d}i_H}{\mathrm{d}t} + 2 \cdot w_H \cdot \frac{\mathrm{d}\Phi_0}{\mathrm{d}t} + u_d(i_H); \quad (3)$$

$$C \cdot \frac{\mathrm{d}u_C}{\mathrm{d}t} = i_B - i_H, \quad (4)$$

where N_B, N_H are the number of turns of the booster and holding windings, respectively.

Here, the capacitance of the capacitor is a stepwise function that depends on the stroke of the armature:

$$C = \begin{cases} C_M & \text{at } s \le s_a; \\ C_0 & \text{at } s > s_a. \end{cases} \quad (5)$$

The system (1)-(5) should be supplemented with the equations of motion of the dynamics of a body with variable mass:

$$\frac{\mathrm{d}}{\mathrm{d}t}(m \cdot v) = F - F_r; \quad (6)$$

$$\frac{\mathrm{d}s}{\mathrm{d}t} = v, \quad (7)$$

where m is the moving mass reduced to the armature; v is the speed; s is the path; F is the electromagnetic force; F_r is the opposing force.

The opposing force is determined as

$$F_r = \begin{cases} F_1 + \dfrac{F_2 - F_1}{s_c} \cdot s & \text{at } s < s_c; \\ F_3 + \dfrac{F_4 - F_3}{s_k - s_c} \cdot (s - s_c) & \text{at } s \ge s_c., \end{cases} \quad (8)$$

where s_c is the moment of contact closure.

Since in (6) it is required to calculate the derivative of the reduced mass, its change is approximated by a smoothed function with continuous first and second derivatives.

The model (1)-(8) is used to calculate the dynamics of the vacuum contactor in the environment of the computer code Maple [13, 14]. The adequacy of this model is confirmed by experimental studies, which showed a good agreement between the calculated and experimental data (see Fig. 3).

III. A "Hybrid" Field-Circuit Method

One of the alternative techniques for calculating the dynamics of electromagnetic mechanisms is a method that was first proposed back in 1989 [5]. A similar method is used in [12, 15] but without taking into account eddy currents in the magnetic circuit. The essence of the method proposed in [5] and improved by the authors of this paper lies in the assumption that the dynamic calculation of electromagnetic actuators is based on the static characteristics of the electromagnet, taking into account eddy currents in the magnetic circuit, as well as the equations of the electric circuit and equations of motion. Since the calculation of the dynamics is based on the calculation of the static characteristics of the electromagnet (the flux reduced by flux linkage and the

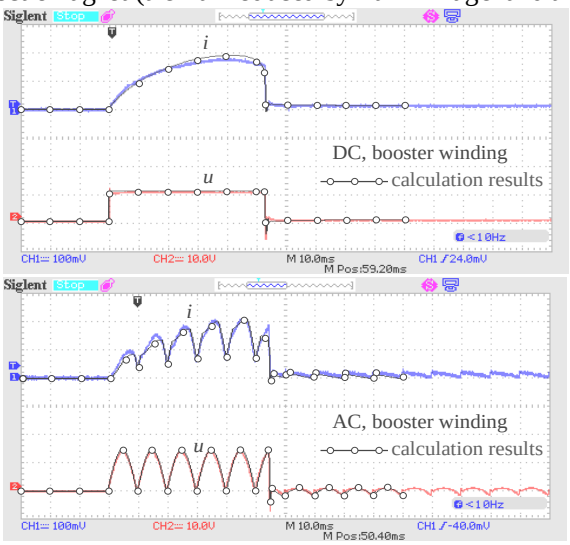

Figure 3: Comparison of numerical and experimental results obtained for a serially manufactured vacuum contactor: current and voltage of the booster winding during switching ON.

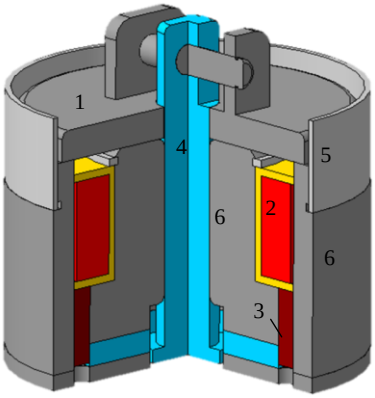

Figure 4: Bistable polarized electromagnet in the "ON" position, where 1 is the armature; 2 is the coil; 3 are the permanent magnets located along the perimeter; 4 are the non-magnetic elements; 5 is the shunt; 6 is the case.

electromagnetic force are determined from the results of the static calculation as a function of the armature stroke and the MMF of the coil), having determined these values, the dynamics of the electromagnetic actuator can be calculated independently of the design of the magnetic system of the electromagnet based on the equations of the electric circuit and the equations of motion.

In this case, the calculation algorithm can be as follows: 1) the static calculation of the electromagnet is carried out for a number of values of the armature stroke (from the initial to the final one) and a number of the coil's MMF (from zero to the maximum possible value); 2) the results of the calculation data are entered into a file in the form of a table; 3) based on the output data of the static calculation, supplemented by the equations of transient processes in the electric circuit, magnetic circuit and the equations of motion, the dynamic characteristics of the electromagnet are calculated.

As an example, consider the application of this technique to the calculation of a bistable polarized electromagnet (see Fig. 4).

The calculation of the static characteristics of the electromagnet is carried out by the Finite Element Method using commercial or open access software codes (in this case, FEMM 4.2 [16] is used).

The calculation model in the cylindrical coordinate system is shown in Fig. 5.

The static calculation equation in terms of the magnetic vector potential in the most general form (the specific form of the equation depends on the computational subdomain) can be written as

$$\nabla\times\left(\frac{1}{\mu(|B|)}\cdot(\nabla\times\vec{A}-\vec{B}_r)\right)=\vec{J}, \qquad (9)$$

where $\mu(|B|)$ is the magnetic permeability as a function of the modulus of magnetic flux density; $\vec{A}$ is the vector magnetic potential; $\vec{B}_r$ is the remanent magnetic flux density of a permanent magnet; $\vec{J}$ is the current density in the winding.

Equation (9) should be supplemented with boundary conditions: equality to zero of the field at the outer boundary

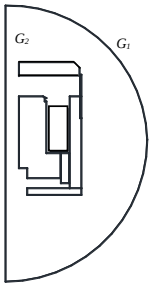

Figure 5: Calculation model of an electromagnet with permanent magnets.

of the computational domain and zero value of the normal component of the field on the axis of symmetry.

Calculation of the magnetic flux reduced by flux linkage, i.e., associated with all turns of the coil and the electromagnetic force is carried out for fixed values of the stroke $\delta[l]\in[0;\ 12]$ mm with a step H_δ = 1 mm and fixed values of the coil MMF $F[j]\in[0;\ 8000]$ A with a step H_F = 1000 A. The calculation of a 2D array with the dimensions 13 x 9 is carried out using the procedure described in [16]. The results of static calculation are presented as the magnetic flux reduced by flux linkage as well as electromagnetic force in the form of tables

$$\Phi_\Psi[l,j];\ Q_\Psi[l,j], \qquad (10)$$

obtained for a number of discrete values of the armature stroke $\delta[l]$ and MMF of the system $F[j]$, the graphic representation of which is shown in Fig. 6.

The calculation of the dynamics requires continuous values of the magnetic flux and electromagnetic force; therefore, the analytical dependencies of the local approximation of the data array (10) are obtained using the functions

$$\begin{aligned}\Phi&=a_0+a_1\cdot(s-\delta[l])+a_2\cdot(iw-F[j])+a_3\cdot(s-\delta[l])\cdot(iw-F[j])\\ Q&=b_0+b_1\cdot(s-\delta[l])+b_2\cdot(iw-F[j])+b_3\cdot(s-\delta[l])\cdot(iw-F[j])\end{aligned} \qquad (11)$$

where iw, s are the current values of MMF and armature stroke which, as a rule, do not coincide with the values of the force and magnetic flux at nodal points; Φ is the current magnetic flux value; Q is the current value of the electromagnetic force.

The unknown coefficients a_i, b_i in (11) are determined based on the solution of the system of equations using the values of the magnetic flux $\Phi_\Psi[l,j]$ and force $Q_\Psi[l,j]$ at the nodal points and depending on the current values of the stroke s and MMF iw as follows. If the current values of iw, s are in the range $\delta[l]\le s\le\delta[l+1]$, $F[j]\le iw\le F[j+1]$, then the unknown coefficients a_i are determined based on the solution of the system of equations

$$\begin{cases}\Phi_\Psi[l,j]=a_0;\\ \Phi_\Psi[l+1,j]=a_0+a_1\cdot H_\delta;\\ \Phi_\Psi[l,j+1]=a_0+a_2\cdot H_F;\\ \Phi_\Psi[l+1,j+1]=a_0+a_1\cdot H_\delta+a_2\cdot H_F+a_3\cdot H_\delta\cdot H_F,\end{cases} \qquad (12)$$

where $\Phi_\Psi[l,j]$ are the values of the magnetic fluxes at the nodal points.

The coefficients b_i are calculated in a similar way. It follows from system (12) that when the current values of the armature stroke and MMF change, the coefficients $a_0..a_3$ in

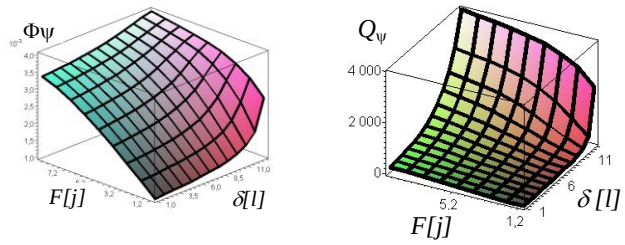

a *b*

Figure 6: Calculated surfaces of the magnetic flux reduced by flux linkage and electromagnetic force: *a* – the magnetic flux; *b* – the electromagnetic force.

the system (12) and, accordingly, the coefficients $b_0 \ldots b_3$ also change.

Further consideration of the problem of the dynamics of the electromagnet is impossible without a description of the electrical circuit for connecting the coil to the power source (see Fig. 7).

The equations describing the processes in the circuit in Fig. 7 have the form

$$\begin{cases} U_0 - \dfrac{q}{C} = L \cdot \dfrac{di_1}{dt} + r \cdot i_1 + w \cdot \dfrac{d\Phi}{dt} + R_K(t) \cdot (i_1 + i_2); \\ U_0 - \dfrac{q}{C} = \left(R_{VD}(i_2) + R\right) \cdot i_2 + R_K(t) \cdot (i_1 + i_2); \\ \dfrac{dq}{dt} = i_1 + i_2, \end{cases} \quad (13)$$

where U_0 is the initial voltage on the capacitor; C is the capacitance; i_1 is the coil current; i_2 is the diode current; R_K is the key's nonlinear resistance; R_{VD} is the diode's nonlinear resistance; R is the additional resistance; q is the electric charge; L is the leakage inductance; r is the resistance of the coil.

The system (13) must be supplemented by the equations of magnetic flux and the MMF of the system:

$$\begin{cases} \Phi = a_0 + a_1 \cdot \left(x - \delta[l]\right) + a_2 \cdot \left(iw - F[j]\right) + \\ a_3 \cdot \left(x - \delta[l]\right) \cdot \left(iw - F[j]\right); \\ iw = w \cdot i_1 - \dfrac{1}{R_f} \cdot \dfrac{d\Phi}{dt}, \end{cases} \quad (14)$$

where R_f is the magnetic resistance to eddy currents in the magnetic circuit; iw is the total MMF of the system.

The open system of equations (13), (14) must be supplemented by the equations of motion and the equation for the electromagnetic force.

$$\begin{cases} m(s) \cdot \dfrac{dv}{dt} + \dfrac{dm}{ds} \cdot v^2 = Q - F_r; \\ \dfrac{ds}{dt} = v; \\ Q = b_0 + b_1 \cdot \left(x - \delta[l]\right) + b_2 \cdot \left(iw - F[j]\right) + \\ b_3 \cdot \left(x - \delta[l]\right) \cdot \left(iw - F[j]\right), \end{cases} \quad (15)$$

where $m(s)$ is the reduced mass depending on the position of the contacts; Q is the electromagnetic force; F_r is the opposing force reduced to the armature; v is the speed of the armature.

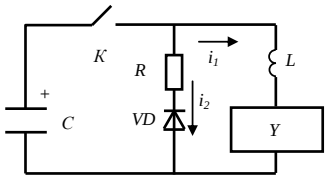

Figure 7: Electrical circuit for connecting the coil to the power source, where *C* is the capacitor; *K* is the key; *R* is the resistor; *VD* is the diode; *Y* is the electromagnet's coil; *L* is the inductance.

To be solved, the system (13)–(15) is written in finite-difference form on a discrete time mesh for $(k+1)$-th and k-th time steps:

$$U_0 - \frac{q^k}{C} = r \cdot i_1^{k+1} + L \cdot \frac{i_1^{k+1} - i_1^k}{\Delta t} + w \cdot \frac{\Phi^{k+1} - \Phi^k}{\Delta t}$$
$$+ R_K(t^k) \cdot (i_1^{k+1} + i_2^{k+1});$$
$$U_0 - \frac{q^k}{C} = \left(R_{VD}(i_2^k) + R\right) \cdot i_2^{k+1} + R_K(t^k) \cdot (i_1^{k+1} + i_2^{k+1});$$
$$\frac{q^{k+1} - q^k}{\Delta t} = i_1^{k+1} + i_2^{k+1}; \quad (16)$$
$$\Phi^{k+1} = a_0 + a_1 \cdot \left(s^k - \delta[l]\right) + a_2 \cdot \left(iw^{k+1} - F[j]\right) +$$
$$a_3 \cdot \left(s^k - \delta[l]\right) \cdot \left(iw^{k+1} - F[j]\right);$$
$$iw^{k+1} = w \cdot i_1^{k+1} - \frac{1}{R_f} \cdot \frac{\Phi^{k+1} - \Phi^k}{\Delta t};$$

$$v^{k+1} = v^k + \frac{\Delta t}{m\left(s^k\right)} \cdot (Q^{k+1}(s^k, iw^{k+1}) - F_r(s^k) -$$
$$\left.\frac{dm}{ds}\right|_{s=s^k} \cdot (v^k)^2);$$
$$s^{k+1} = s^k + \Delta t \cdot v^{k+1}; \quad (17)$$
$$Q^{k+1} = b_0 + b_1 \cdot \left(s^k - \delta[l]\right) + b_2 \cdot \left(iw^{k+1} - F[j]\right) +$$
$$b_3 \cdot \left(s^k - \delta[l]\right) \cdot \left(iw^{k+1} - F[j]\right).$$

The solution of the system (16), (17) allows to obtain the values of the sought parameters i_1^{k+1}, i_2^{k+1}, q^{k+1}, Φ^{k+1}, iw^{k+1}, v^{k+1}, s^{k+1}, Q^{k+1}, which determine the dynamic processes in the electrical, magnetic and mechanical circuits. An algorithm is the following: 1) Localization of constants l, j in tables $\Phi_\Psi[l, j]$ and $Q_\Phi[l, j]$ is determined for values x^k, iw^k; 2) Using formulas (7), for discrete values $\Phi_\Psi[l, j]$ the coefficients a_i, b_i in (6) are determined; 3) According to (16), (17), the sought values at $(k+1)$-th time step are determined, namely currents, magnetic flux, MMF, speed and stroke; 4) The condition for termination the calculation (the traction characteristic reaches the steady-state value of the force due to the drop in the total flux (magnets together with coil) after the coil is de-energized) is checked, and if the calculation continues, we redefine the variables and return to item 1).

The calculation of the dynamics is carried out for a serially manufactured vacuum contactor: the coil's resistance in a cold state is 85 Ω; the number of turns is 1850; the contacts' stroke is 12 mm; the capacitor's

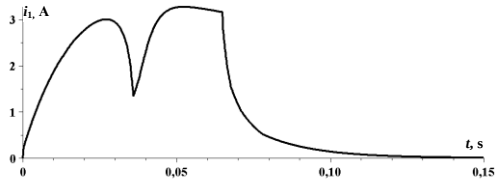

Figure 8: Capacitor's current time variation.

capacitance is 3000 μF; the voltage on the capacitor is 320 V. The results obtained for time variation of the capacitor's current, electromagnet armature's displacement and speed as well as forces acting on the electromagnet's armature are presented in Fig. 8-11.

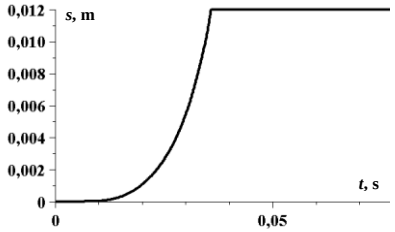

Figure 9: Electromagnet armature's displacement time variation.

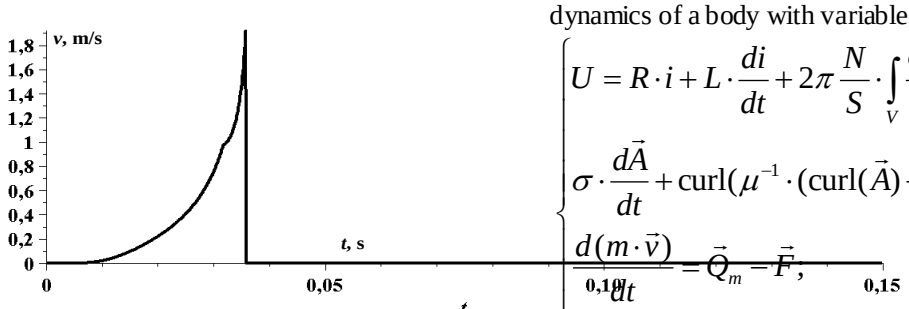

Figure 10: Electromagnet armature's speed time variation.

From the results obtained it is follows that at the moment of time 0.65 s, the position sensor disconnects the capacitor from the electromagnet's coil. Holding the armature of the electromagnet in the attracted position after the coil is disconnected is carried out by permanent magnets. The change in the nature of the speed dependence is associated with a change in the moving mass reduced to the armature of the electromagnet.

From the results presented it follows that the electromagnetic force, both in the operation mode of the electromagnet and in the mode of holding the armature in the attracted position is clearly redundant and the design needs to be optimized.

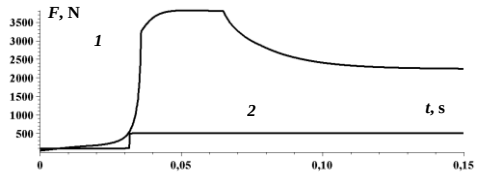

Figure 11: Forces acting on the electromagnet's armature: 1 – electromagnetic force; 2 – opposing force.

IV. A Coupled Field-Circuit Approach

A rigorous numerical solution of the problem of calculating the dynamics of electromagnets is based, first of all, on Maxwell equations describing transient electromagnetic field distribution [11]. As applied to the calculations of electromagnets, the system of Maxwell equations in the differential form [11] should be simplified based on the following considerations: 1) the design of many electromagnets is such that it is convenient to carry out calculations in axi-symmetrical formulation in a cylindrical coordinate system in terms of magnetic vector potential; 2) the frequency of electromagnetic oscillations is low and the radiation of electromagnetic energy and displacement currents in the dielectrics can be neglected; 3) the conduction currents in the conductors are much higher than the displacement currents. Such calculations can be carried out using in-house or commercial applied computer codes such as ANSYS [17], COMSOL Multiphysics [18], etc.

The proposed model is a system of differential equations describing physical processes: in a non-linear electrical circuit, an electromagnetic field in a non-linear conducting moving medium taking into account permanent magnets, and mechanical equations of the dynamics of a body with variable mass:

$$\begin{cases} U = R\cdot i + L\cdot\dfrac{di}{dt} + 2\pi\dfrac{N}{S}\cdot\int\limits_V \dfrac{\partial A_\varphi(r,z,t)}{\partial t}\cdot dV; \\ \sigma\cdot\dfrac{d\vec{A}}{dt} + \mathrm{curl}(\mu^{-1}\cdot(\mathrm{curl}(\vec{A}) - \vec{B}_r) = \dfrac{i\cdot N}{S}\cdot\vec{1}_\varphi; \\ \dfrac{d(m\cdot\vec{v})}{dt} = \vec{Q}_m = \vec{F}; \\ \dfrac{ds}{dt} = \vec{v}, \end{cases} \tag{18}$$

where the above notation has been used.

In the case of a moving medium or a moving object in a stationary medium:

$$\frac{d\vec{A}}{dt} = \frac{\partial\vec{A}}{\partial t} - \vec{v}\times\left(\nabla\times\vec{A}\right) = \frac{\partial\vec{A}}{\partial t} - \vec{v}\times\vec{B}. \tag{19}$$

Based on the above model (18), (19) numerical solution, a bistable electromagnet with two armatures and permanent magnets (see Fig. 12) is calculated.

The electromagnet contains (see Fig. 12) movable armatures (1), a ferromagnetic shunt (2), a winding (3), a winding frame (4), a core (5), a case (6), permanent magnets (7) located along the inner perimeter of the case, and base (8). The design of the bistable electromagnet has a central non-magnetic rod, which is connected through the levers of the shaft with moving contacts, and also connects the upper and lower armatures, which ensures synchronization of the movement of the armatures when the electromagnet is triggered (not shown in Fig. 12).

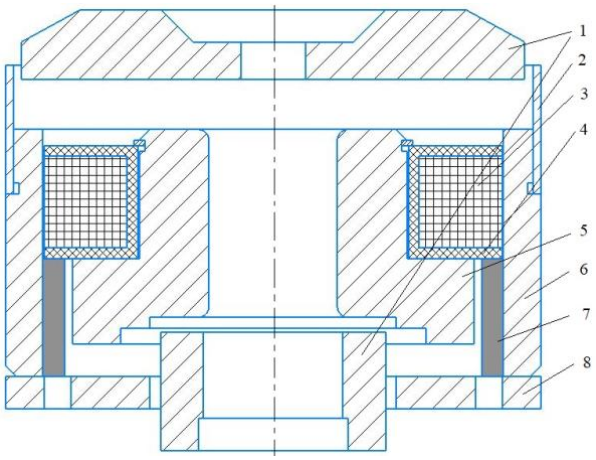

Figure 12: A sketch of a bistable electromagnet.

This electromagnet is a driving mechanism for a MV vacuum circuit breaker and must provide a contact pressure of at least 6000 N (2000 N per pole) due to permanent magnets with de-energized coils. The coils are powered by a capacitor with capacitance of 60000 μF and charged up to voltage of 100 V. A feature of the operation of the electromagnet power supply circuit is that the capacitor is switched off by the command of the microprocessor after it is triggered.

The results of calculating the characteristics of a bistable electromagnet are presented in Fig. 13, 14.

Figure 13 shows the distributions of the electromagnetic field of half of the electromagnet cross-section in the initial and final positions of the armature with de-energized coils. The maximum values of magnetic flux density in the electromagnet are approximately equal and amount to about 1.4 T.

The dynamic characteristics are obtained on the basis of static calculations as initial conditions, taking into account the deformation of the computational finite element mesh during the movement of the electromagnet armatures. In this case, the total value of the force acting on the armature of the electromagnet when the circuit breaker is switched shown in Fig. 14 is of particular interest.

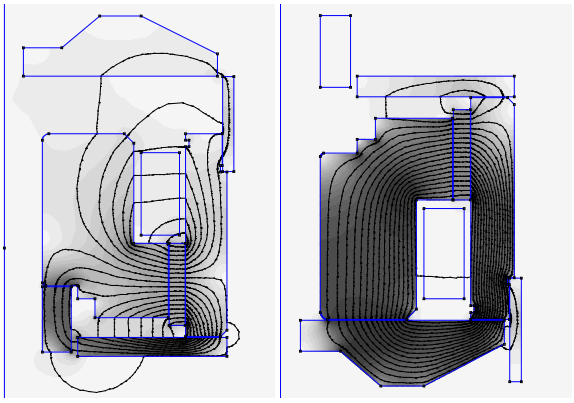

a *b*

Figure 13: Electromagnetic field distribution in initial (*a*) and final (*b*) positions of the armature.

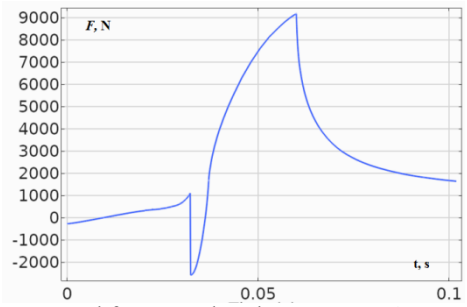

Figure 14: Total force on the electromagnet's armatures when the circuit breaker is switched ON.

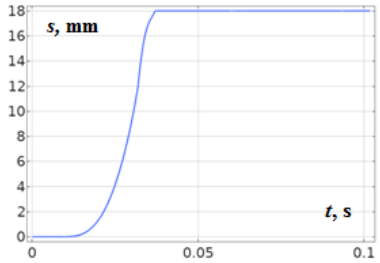

Figure 15: Armature's stroke time variation.

As follows from Fig. 14, at the moment of closing the contacts, the force takes on negative values, but due to the kinetic energy, the system passes this position and the circuit breaker is successfully switched ON. After 60 ms, the capacitor is disconnected from the coil and the electromagnetic force drops to values determined by the permanent magnets. From Fig. 14 it can be seen that the steady-state value of this force is approximately 1000 N, which ensures the normal operation of the circuit breaker contacts in the ON state.

Figure 15 shows the value of the stroke of the armature of the electromagnet as a function of time.

Figure 16 shows the distribution of the modulus of the magnetic flux density and eddy currents in the magnetic circuit at time of 0.01 s (immediately before the armature starts to move). From the graphs it follows that: at the initial moments of time, the magnetic flux density and eddy currents are concentrated along the inner perimeter of the same structure being distributed over the section over time; in the same structural elements, magnetic flux density and eddy currents can have different directions.

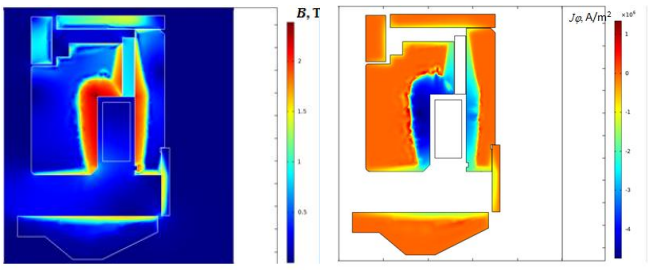

a *b*

Figure 16: Distributions of the magnetic flux density module (*a*) and eddy currents (*b*) at 0.01 s (immediately before the armature starts to move).

V. Conclusions

Each of the methods for calculating the dynamics of electromagnets described in the paper has its own advantages and disadvantages. The simplest method presented for dynamic calculations of neutral electromagnets was the method of "electrical analogy" using lumped parameter and circuit models. In the case of small (compared to the size of the magnetic circuit) air gaps and simple designs of electromagnets, this approach gave good results. The resulting differential equations are solved by numerical integration methods of second and third order of accuracy. The difficulty of this approach was determining the values of the resistances of the solid sections of the magnetic circuit, in which the eddy currents are distributed extremely non-uniformly, as well as the equivalent conductivities of the air gaps.

The "hybrid" method combines static field calculations by the Finite Element Method of complex designs of polarized electromagnets with analytical methods for calculating the coils' power supply circuits and motion dynamics. For these designs free computer codes based on the Finite Element Method were used for calculating electromagnetic systems. Disadvantages of this approach were shown to be similar to the previous technique, i.e., their origin was the difficulty in determining the equivalent resistances to eddy currents in the magnetic conductor.

The most accurate results in the calculation of the dynamics of electromagnetic systems were achieved by using the Finite Element Method models using commercial computer codes at the cost of extended simulation times.

References

[1] J.-S. Ro, S.-K. Hong, and H.-K. Jung, "Characteristic analysis and design of a novel permanent magnetic actuator for a vacuum circuit breaker," *IET Electric Power Applications*, vol. 7, No. 2, pp. 87-96, Feb. 2013.

[2] J. Zhang, Ch. Cai, and Ch. Wu, "Design and analysis of a new permanent magnet actuator for medium voltage vacuum circuit breakers," *Applied Mechanics and Materials*, vol. 313-314, pp. 20-26, March 2013.

[3] A. Bissal, J. Magnusson, E. Salinas, and G. Engdahl, "Multiphysics modeling and experimental verification of ultra-fast electro-mechanical actuators," International Journal of *Applied Electromagnetics and Mechanics*", vol. 49, pp. 51-59, 2015.

[4] https://new.abb.com/medium-voltage/apparatus/circuit-breakers

[5] B.V. Klymenko, *Electric Apparatus. The Introductory Course: Textbook*, 2nd ed., Kharkiv: Tochka Publishing House, 2013 (in Ukrainian).

[6] B.V. Klymenko, A.M. Grechko, V.M. Bugaichuk, and S.V. Vyrovets, "Fast acting electromagnetic actuator with magnetic field displacement for medium voltage vacuum circuit breaker," *Electrical Engineering & Electromechanics*, No. 2, pp. 22-26, 2006 (in Russian).

[7] B.V. Klymenko, V.M. Bugaichuk, and A.M. Grechko, "Electromagnetic actuator for medium voltage vacuum circuit breakers," *Bulletin of NTU "KhPI"*, No. 42, pp. 73-80, 2004 (in Russian).

[8] A.G. Nikitenko, *Computer-aided Design of Electrical Devices*, Moscow: High School, 1983 (in Russian).

[9] R. Wait and A.R. Mitchell, *Finite Element Analysis and Applications*, Wiley, 1985.

[10] L.J. Segerlind, *Applied Finite Element Analysis*, 2nd ed., Wiley, 1984.

[11] P.P. Silvester and R.L. Ferrari, *Finite Elements for Electrical Engineers*, 3rd ed., Cambridge University Press, 1996.

[12] L. Sun, S. He, Yi. Feng, and Zh. Lu, "A permanent magnetic actuator for 126 kV vacuum circuit breakers," *IEEE Transactions on Magnetics*, vol. 50, No. 3, pp. 129-135, March 2014.

[13] https://www.maplesoft.com/

[14] Ye.I. Baida, M. Clemens, B.V. Klymenko, O.G. Korol, M.G. Pantelyat, and P.Ye. Pustovoitov, "Peculiarities of calculating stationary heating of winding operating in complex forced control systems," *Electrical Engineering & Electromechanics*, No. 5, pp. 12-19, 2019.

[15] I. Yatchev, K. Hinov, and V. Gueorgiev, "Dynamics characteristics of a bistable linear actuator with moving permanent magnet," *Serbian Journal of Electrical Engineering*, vol. 1, No. 2, pp. 207-214, June 2004.

[16] http://www.femm.info/wiki/HomePage

[17] https://www.ansys.com/products/electronics/ansys-maxwell

[18] https://www.comsol.com/

Reduced order field-circuit modeling of squirrel cage induction machines for automotive applications

Bíró Dániel (1), Diwoky Franz (1), Schmidt Erich (2)

(1) Advanced Simulation Technologies (AST), AVL List GmbH, Graz, Austria
(2) Institute of Energy Systems and Electric Drives, Vienna University of Technology, Wien, Austria

Purpose:

The aim of the paper is to investigate the impacts of simplifications of a reduced-order simulation model of squirrel cage induction machines (SCIMs) by numerical experiments.

Design/methodology/approach:

Design of setups to isolate the main influences on the results of the reduced-order model of SCIMs. Results of time-stepping finite element calculations are used as benchmark.

Findings:

Whereas neglecting eddy current effects and the assumption of a sinusoidal rotor current distribution leads to acceptable deviations in regular inverter operation, the sampling and interpolation of the machine parameters in a two-axis coordinate system considerably deteriorate the model accuracy. Using a polar coordinate system for this purpose is expected to significantly improve the model quality.

Originality/value:

Preparing the ground for a successful, both fast and accurate simulation model of SCIMs as parts of electrified drivetrains.

Keywords:

Electrical machine, Finite element analysis, Induction machine modeling, Multiphysics, Reduced-order model, Space vector theory

Published in COMPEL - The international journal for computation and mathematics in electrical and electronic engineering, Vol. 41 No. 3, 2022, ISSN 0332-1649, page 794 - 806

Sensorless metal object detection for wireless power transfer using machine learning

Gong Yunyi, Otomo Yoshitsugu, Igarashi Hajime

Graduate School of Information Science and Technology, Hokkaido University, Sapporo, Japan

Purpose:

This study aims to realize a sensorless metal object detection (MOD) using machine learning, to prevent the wireless power transfer (WPT) system from the risks of electric discharge and fire accidents caused by foreign metal objects.

Design/methodology/approach:

The data constructed by analyzing the input impedance using the finite element method are used in machine learning. From the loci of the input impedance of systems, the trained neural network (NN), support vector machine and naive Bayes classifier judge if a metal object exists. Then the proposed method is tested by experiments too.

Findings:

In the test using simulated data, all of the three machine learning methods show high accuracy of over 80
Originality/value:

This work provides a new sensorless MOD method for WPT using three machine learning methods. And it shows that NNs obtain high accuracy than the others in both simulated and experimental verifications.

Keywords:

Machine learning, Metal object detection, Wireless power transfer, Support vector machines

Published in COMPEL - The international journal for computation and mathematics in electrical and electronic engineering, Vol. 41 No. 3, 2022, ISSN 0332-1649, page 807 - 823

Bayesian inference of multi-sensors impedance cardiography for detection of aortic dissection

Badeli Vahid (1), Ranftl Sascha (2), Melito Marco Gian (3), Reinbacher-Köstinger Alice (1), Linden Der Von Wolfgang (2), Ellermann Katrin (3), Biro Oszkar (1)

(1) Institute of Fundamentals and Theory of Electrical Engineering, Graz University of Technology, Graz, Austria
(2) Institute of Theoretical and Computational Physics, Graz University of Technology, Graz, Austria
(3) Institute of Mechanics, Graz University of Technology, Graz, Austria

Purpose:

This paper aims to introduce a non-invasive and convenient method to detect a life-threatening disease called aortic dissection. A Bayesian inference based on enhanced multi-sensors impedance cardiography (ICG) method has been applied to classify signals from healthy and sick patients.

Design/methodology/approach:

A 3D numerical model consisting of simplified organ geometries is used to simulate the electrical impedance changes in the ICG-relevant domain of the human torso. The Bayesian probability theory is used for detecting an aortic dissection, which provides information about the probabilities for both cases, a dissected and a healthy aorta. Thus, the reliability and the uncertainty of the disease identification are found by this method and may indicate further diagnostic clarification.

Findings:

The Bayesian classification shows that the enhanced multi-sensors ICG is more reliable in detecting aortic dissection than conventional ICG. Bayesian probability theory allows a rigorous quantification of all uncertainties to draw reliable conclusions for the medical treatment of aortic dissection.

Originality/value:

This paper presents a non-invasive and reliable method based on a numerical simulation that could be beneficial for the medical management of aortic dissection patients. With this method, clinicians would be able to monitor the patient's status and make better decisions in the treatment procedure of each patient.

Keywords:

Numerical analysis, Finite element method, Sensors, Impedance, Bioelectromagnetics,Uncertainties in electromagnetics, Bayesian inference, Probability theory, Impedance cardiography,Aortic dissection

Published in COMPEL - The international journal for computation and mathematics in electrical and electronic engineering, Vol. 41 No. 3, 2022, ISSN 0332-1649, page 824 - 839

Comparison of 2 to 6 layered soil models using evolutionary methods for parameters' determination

*Marko Jesenik, *Anton Hamler, *Mislav Trbušić and *Mladen Trlep
*Faculty of Electrical Engineering and Computer Scinece, Koroška cesta 46, 2000 Maribor, Slovenia

***Abstract*— Grounding systems are used to protect people and devices, therefore, it is important to dimension them properly. The Finite Element Method is often used for the dimensioning of the grounding systems and the properties of the soil are needed for that. The parameters of a horizontally layered soil model can be determined using evolutionary methods based on the Wenner's method measurements. Different soil structures are used in the paper to analyse the applicability of the horizontally layered soil model. Different evolutionary methods are tested, with the aim to get the most appropriate one, between those selected, for the presented problem.**

***Index Terms*— Evolutionary methods, Finite Element Method, Grounding system.**

I. INTRODUCTION

Grounding systems are an important part of protection systems, and often the Finite Element Method (FEM) [1, 2] is used for their effective dimensioning. FEM analysis can't be done without data about soil properties. These data can be obtained using measurements. Usually, the Wenner four-electrode method [3, 4] is used to get the dependence of apparent resistivity upon the distance of the electrodes. This set of data is interpreted using inversion methods, often optimisation methods, to find an equivalent horizontally layered soil that best fits the data set obtained using Wenner's method. The applicability of a horizontally layered soil model [5, 6] is analysed for different soil structures. An FEM model of soil structure is made to get sets of apparent resistivity versus electrode spacing. 2-6 layered models (LMs) are tested. Also, three different optimisation methods are used for soil parameters` determination, which are Differential Evolution (DE) [7-9], Teaching Learning Based Optimization (TLBO) [10, 11] and Artificial Bee Colony (ABC) [12, 13], with the aim to select the most appropriate for the presented problem.

II. WENNER'S METHOD

The basis for the soil determination are the measurements using the Wenner four electrodes method presented in Figure 1.

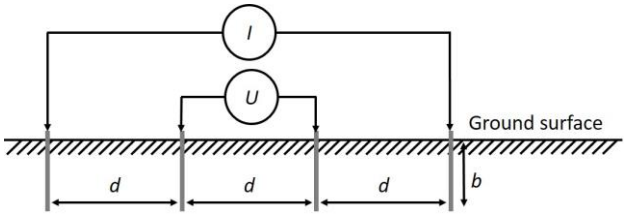

Figure 1: Wenner's method.

Four electrodes are placed at the same distance *d*. The current is injected between the outer electrodes and voltage is measured between the inner electrodes. In practice, depth b, presented in Figure1, is less than 0.1, *d*, and apparent resistivity can be calculated using (1) [4].

$$\rho = \frac{2 \cdot \pi \cdot d \cdot U}{I} \tag{1}$$

I is the injected current, *U* is the measured voltage and *d* is the distance between the electrodes. In Wenner's method, the distance *d* is increased and a set of data is obtained containing apparent resistivity versus distance between the electrodes.

III. TEST MODELS

In the analysis of soil models with different numbers of layers, it is very useful if the structure of the soil is known. Using Flux 3D software, the FEM models are made and, with that, the soil structure is known. The FEM model made using Altair Flux software, which simulates the Wenner's method measurements, is presented in Figure 2.

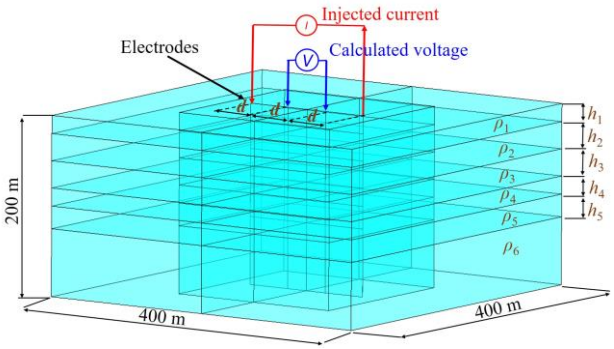

Figure 2: FEM model used for Wenner's method simulation.

In the FEM model four electrodes are also modelled, in a line at the same distance (according to Wenner's method). For data test sets the distance *d* is changed between 0.5 to 80 metres. More information about deeper soil is obtained at higher distances. The depth of the FEM model is 200 m, because the penetration depth of the current field is much smaller.

In Figure 2 a 6-layered model is presented, but as test data sets three different models were made, which are marked as Model A, Model B and Model C, as presented in Figure 3.

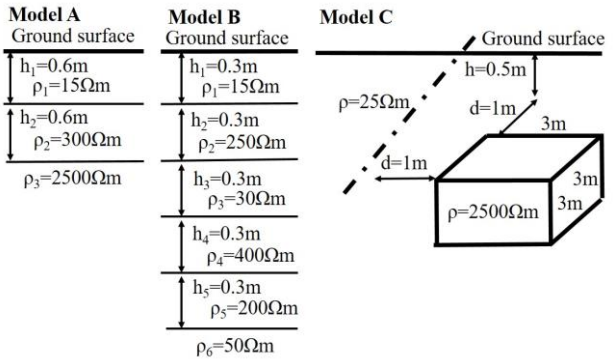

Figure 3: Soil parameters of FEM models.

Model A is a 2-layered soil model which was made to analyse multi-layered soil models in the case of 2-layered soil. Model B is a 6-layered soil model, which was made to analyse soil models with a lower number of layers in the case of 6-layered soil model. Model C is a model with inhomogeneity, which was made to analyse the usefulness of horizontally layered soil models in cases of soil with inhomogeneity.

IV. Analytical Soil Models

Horizontally multi-layered analytical soil models were used for the presentation of the soil properties. The parameters of the analytical soil model were set so that the model best fitted the data set obtained using Wenner's method. The *N*-layered soil model is presented in Figure 4.

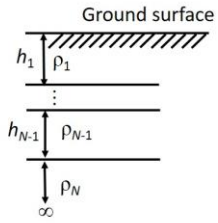

Figure 4: *N*-layered analytical soil model.

We tested a 2-layered soil model, which has 3 parameters, a 3-layered soil model, which has 5 parameters, a 4-layered soil model, which has 7 parameters, 5-layered soil model, which has 9 parameters, and a 6-layered soil model, which has 11 parameters.

The apparent resistivity was calculated using (2) [5].

$$\rho = \rho_1 \left(1 + 2d \int_0^\infty f(\lambda) \cdot \left[\mathrm{J}_0(\lambda d) - \mathrm{J}_0(2\lambda d) \right] d\lambda \right) \quad (2)$$

ρ_1 is the specific resistivity of the first layer, d is the distance between the electrodes, and J_0 is a Bessel function.

Function $f(\lambda)$ was determined with (3).

$$f(\lambda) = \alpha_1(\lambda) - 1 \quad (3)$$

α1 for the N-layered model was calculated as a sequence of the expressions presented in (4).

$$K_{N-1}(\lambda) = \frac{\rho_N - \rho_{N-1}}{\rho_N + \rho_{N-1}}$$

$$\alpha_{N-1} = 1 + \frac{2K_{N-1}e^{-2\lambda h_{N-1}}}{1 - K_{N-1}e^{-2\lambda h_{N-1}}}$$

$$K_{N-2}(\lambda) = \frac{\rho_{N-1}\alpha_{N-1}(\lambda) - \rho_{N-2}}{\rho_{N-1}\alpha_{N-1}(\lambda) + \rho_{N-2}}$$

$$\alpha_{N-1} = 1 + \frac{2K_{N-2}e^{-2\lambda h_{N-2}}}{1 - K_{N-2}e^{-2\lambda h_{N-2}}} \quad (4)$$

$$\dots$$

$$K_1(\lambda) = \frac{\rho_2\alpha_2(\lambda) - \rho_1}{\rho_2\alpha_2(\lambda) + \rho_1}$$

$$\alpha_1 = 1 + \frac{2K_1e^{-2\lambda h_1}}{1 - K_1e^{-2\lambda h_1}}$$

Numerical calculation should be used to calculate apparent resistivity using (2). The integration stopped when the value of the integrated function was 10 times successively smaller than $1 \cdot 10^{-6}$; only once was not enough due to the oscillating character of the integrated function.

V. Used Optimisation Methods and Objective Function

As mentioned, we were searching for the parameters of a multi layered soil model that best fit the data sets (Models A, B and C) obtained using the FEM model. It is an inverse problem, which is also an optimisation problem and we were using a direct approach to solve it.

We selected three evolutionary optimisation methods to solve the presented problem, which were DE, TLBO and ABC. DE is an evolutionary optimisation method often used in the case of engineering problems. The strategy used was DE/rand/1/exp, the crossover probability rate was set to 0.8 and amplification of differential variation was set to 0.6.

TLBO is a newer evolutionary optimisation method. It is a parameter free method. TLBO has two phases, which are a teaching phase and a learning phase. Therefore, the number of Fitness Evaluations in the scope of one iteration is two times the number of Fitness Evaluations in the scope of one iteration in the case of DE.

ABC is also a newer method. The control parameter Limit was set to 100. In the case of ABC, dynamic counting of Fitness Evaluations should be done, because the number of Fitness Evaluations in the scope of one iteration is not the same for all iterations.

The Objective Function (OF) is written in (5).

$$\mathrm{OF} = \frac{1}{n} \sum_{i=1}^{n} \left| \frac{\rho_\mathrm{c} - \rho_\mathrm{m}}{\rho_\mathrm{m}} \right| \cdot 100 \ (\%) \quad (5)$$

Where ρ_c are apparent resistivity calculated values using the soil model. and ρ_m are the values obtained using

the FEM model (Wenner's method).

For each method 30 independent runs were made, and the limits of the specific soil resistance were between 5 and 3500 Ωm, due to the physical properties of the soil.

The number of parameters for the 2, 3, 4, 5 and 6-layered models was 3, 5, 7, 9 and 11. The used population was 6 times the number of the parameters.

To ensure fair comparison of the optimisation methods and models, the same stopping criteria were used for all tests, which was 41,580 Fitness Evaluations.

The parameters used in the case of 2 LM are presented in Table I, in the case of 3 LM are presented in Table III, in the case of 4 LM in Table IV, in the case of 5 LM in Table V, and in the case of 6 LM in Table VI.

TABLE I
PARAMETERS USED IN THE CASE OF 2 LM

2 layered model	DE	TLBO	ABC
Number of parameters (P)	3	3	3
Population number (P x 6)	18	18	18
Number of iterations (ITER)	2310	1155	≤2310
Fitness Evaluations (FEs = NP x ITER)	41580	41580	max. 41580

TABLE II
PARAMETERS USED IN THE CASE OF 3 LM

3 layered model	DE	TLBO	ABC
Number of parameters (P)	5	5	5
Population number (P x 6)	30	30	30
Number of iterations (ITER)	1386	693	≤1386
Fitness Evaluations (FEs = NP x ITER)	41580	41580	max. 41580

TABLE III
PARAMETERS USED IN THE CASE OF 4 LM

4 layered model	DE	TLBO	ABC
Number of parameters (P)	7	7	7
Population number (P x 6)	42	42	42
Number of iterations (ITER)	990	495	≤990
Fitness Evaluations (FEs = NP x ITER)	41580	41580	max. 41580

TABLE IV
PARAMETERS USED IN THE CASE OF 5 LM

5 layered model	DE	TLBO	ABC
Number of parameters (P)	9	9	9
Population number (P x 6)	54	54	54
Number of iterations (ITER)	770	385	≤770
Fitness Evaluations (FEs = NP x ITER)	41580	41580	max. 41580

TABLE V
PARAMETERS USED IN THE CASE OF 6 LM

6 layered model	DE	TLBO	ABC
Number of parameters (P)	11	11	11
Population number (P x 6)	66	66	66
Number of iterations (ITER)	630	315	≤630
Fitness Evaluations (FEs = NP x ITER)	41580	41580	max. 41580

VI. RESULTS FOR MODEL A

The best value (B), the worst value (W), mean value (M) and Standard Deviation (SD) of the Objective Function (OF) for Model A are presented in Table VI. The designation LM means Layered Model.

TABLE VI
B, W, M AND SD FOR 30 INDEPENDENT RUNS FOR MODEL A

Model		ABC	TLBO	DE
2 LM	B	2.1677	1.9600	1.9600
	W	9.4339	1.9600	45.7095
	M	4.1160	1.9600	7.8748
	SD	2.2425	$8.88\cdot10^{-16}$	14.84
3 LM	B	1.9710	1.6568	1.6568
	W	8.1920	1.6571	5.8447
	M	2.5715	1.6569	1.8656
	SD	1.2286	$7.63\cdot10^{-5}$	$7.65\cdot10^{-1}$
4 LM	B	1.8356	1.6411	,1.6410
	W	8.1017	1.6569	2.2232
	M	3.0843	1.6501	1.6900
	SD	1.7008	$7.51\cdot10^{-3}$	$1.39\cdot10^{-1}$
5 LM	B	1.7042	1.6412	1.6410
	W	2.2478	1.6585	1.6568
	M	1.9265	1.6497	1.6485
	SD	$1.74\cdot10^{-1}$	$6.74\cdot10^{-3}$	$7.69\cdot10^{-3}$
6 LM	B	1.6888	1.6417	1.6410
	W	3.5144	1.6847	1.6653
	M	1.9917	1.6529	1.6495
	SD	$3.42\cdot10^{-1}$	$9.02\cdot10^{-3}$	$7.93\cdot10^{-3}$

The calculated parameters for the 2 to 6 layered models for the best solution using ABC are presented in Table VII.

TABLE VII
CALCULATED PARAMETERS FOR THE 2 TO 6 LAYERED MODEL FOR THE BEST SOLUTION USING ABC FOR MODEL A

Par.	2 Lay.	3 Lay.	4 Lay.	5 Lay.	6 Lay.
ρ_1	15.519	15.272	15.375	15.372	15.351
h_1	0.667	0.645	0.655	0.655	0.653
ρ_2	3468.1	2267.9	3500	3500	3500
h_2		7.098	2.740	2.578	1.598
ρ_3		3500	775.91	1357.7	2865.9
h_3			1.179	2.294	1.249
ρ_4			3500	3498.5	159.38
h_4				23.159	0.106
ρ_5				3500	1552.9
h_5					1.261
ρ_6					3500

The apparent resistances, calculated using parameters from Table VII, are presented in Figure 5.

Based on Table VI it can be seen that 2-LM was not appropriate using ABC (M was 4.1160%), and using DE (M was 7.8748%). All other soil models (3-6 LMs) were appropriate combined with any of used methods (ABC, TLBO and DE).

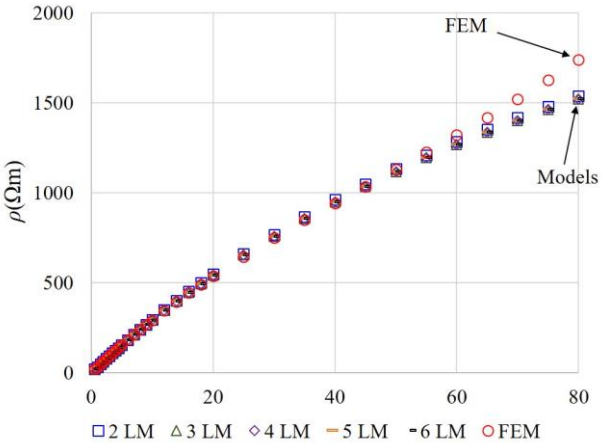

Figure 5: Calculated apparent resistances for 2-6 layered models using the parameters from Table VII.

VII. Results for Model B

B, W, M and SD of the Objective Function (OF) for Model B are presented in Table VIII.

TABLE VIII
B, W, M and SD for 30 Independent Runs for Model B

Model		ABC	TLBO	DE
2 LM	B	10.1095	10.1095	10.1095
	W	10.1095	10.1095	14.0390
	M	10.1095	10.1095	10.7365
	SD	$1.72 \cdot 10^{-5}$	$3.40 \cdot 10^{-8}$	1.2479
3 LM	B	2.1091	2.3463	8.0107
	W	4.2378	8.3189	8.3163
	M	2.6428	7.7526	8.1123
	SD	$4.27 \cdot 10^{-1}$	1.4266	$1.44 \cdot 10^{-1}$
4 LM	B	1.9321	1.9505	2.0321
	W	4.9352	8.7380	8.3655
	M	2.7831	7.7380	7.9122
	SD	$6.84 \cdot 10^{-1}$	1.7881	1.1023
5 LM	B	1.7417	2.8652	7.6502
	W	5.1072	8.9843	8.6392
	M	2.8546	7.7721	7.9863
	SD	$7.72 \cdot 10^{-1}$	1.3939	$3.4386 \cdot 10^{-1}$
6 LM	B	0.6745	2.5605	0.6701
	W	7.1928	8.7376	8.3304
	M	2.6912	8.2404	7.4560
	SD	1.2804	1.1230	1.5591

The calculated parameters for the 2 to 6 layered models for the best solution using ABC are presented in Table IX.

Based on Table VIII, it can be seen that, in the case of TLBO and DE, none of models was appropriate (M was more than 7%). DE and TLBO got stuck at the local minimum.

In the case of ABC 2 LM was not appropriate (M was more than 10%). All other models, 3-6 LMs, were appropriate (M was less than 3%), and ABC was able to avoid the local minimum.

TABLE IX
Calculated Parameters for the 2 to 6 Layered Models for the Best Solution Using ABC for Model B

Par.	2 Lay.	3 Lay.	4 Lay.	5 Lay.	6 Lay.
ρ_1	69.790	5.707	10.567	5.479	18.234
h_1	6.123	0.100	0.172	0.126	0.304
ρ_2	53.048	104.87	89.833	1488.6	94.834
h_2		2.263	3.835	0.102	2.716
ρ_3		35.346	48.834	58.147	53.663
h_3			29.133	16.050	19.655
ρ_4			65.355	5.001	37.238
h_4				1.072	20
ρ_5				66.677	65.491
h_5					19.226
ρ_6					117.45

Apparent resistances, calculated using the parameters from Table IX, are presented in Figure 6.

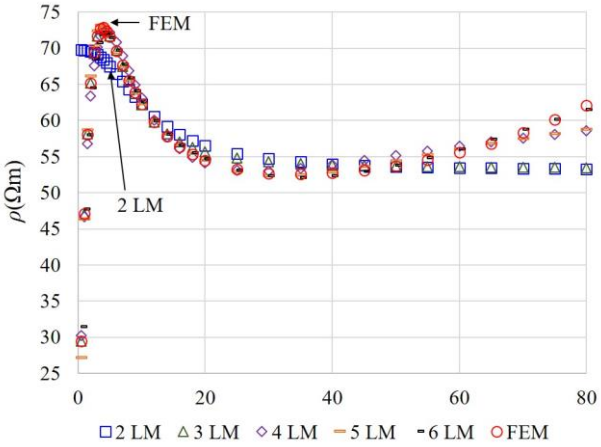

Figure 6: Calculated apparent resistances for the 2-6 layered models using the parameters from Table IX.

VIII. Results for Model C

The B, W, M and SD of the Objective Function (OF) for Model B are presented in Table X. The calculated parameters for the 2 to 6 layered models for the best solution using ABC are presented in Table XI. Apparent resistances, calculated using the parameters from Table XI, are presented in Figure 7.

Based on Table X, mean OFs were much higher than in case of 3-6 LMs, and, based on Figure 7, it can be seen that 2 LM was not appropriate. Due to the mean OFs from Table X for 3-6 LMs, which were up to 1.3% for all used methods, it can be concluded that 3-6 LMs are appropriate for the presented case.

IX. Conclusions

Although only three test cases were made, certain conclusions can be drawn about the different layered soil models used, and about the evolutionary methods used. It is not only important which soil model we use, but also which method we use to calculate the coefficients.

TABLE X
B, W, M AND SD FOR 30 INDEPENDENT RUNS FOR MODEL C

Model		ABC	TLBO	DE
2 LM	B	2.2799	2.2791	2.2791
	W	3.7331	2.2791	5.8416
	M	2.4762	2.2791	2.7835
	SD	$3.23\cdot10^{-1}$	$4.44\cdot10^{-16}$	1.2098
3 LM	B	0.9372	0.9334	0.9334
	W	1.1326	1.3278	5.3698
	M	0.9721	1.1024	1.2816
	SD	$3.63\cdot10^{-2}$	$1.32\cdot10^{-1}$	$8.69\cdot10^{-1}$
4 LM	B	0.8989	0.7721	0.7579
	W	1.2224	1.2822	3.2130
	M	1.0970	1.2200	1.2251
	SD	$8.07\cdot10^{-2}$	$1.03\cdot10^{-1}$	$6.17\cdot10^{-1}$
5 LM	B	0.6854	0.6806	0.6515
	W	1.2398	1.3941	5.5177
	M	0.9391	1.2001	1.2083
	SD	$1.37\cdot10^{-1}$	$1.19\cdot10^{-1}$	$9.17\cdot10^{-1}$
6 LM	B	0.7090	0.6829	0.6911
	W	1.3539	1.8351	3.3727
	M	0.9742	1.1621	1.2612
	SD	$1.82\cdot10^{-1}$	$2.48\cdot10^{-1}$	$6.91\cdot10^{-1}$

TABLE XI
CALCULATED PARAMETERS FOR 2 TO 6 LAYERED MODEL FOR THE BEST SOLUTION USING ABC FOR MODEL C

Par.	2 Lay.	3 Lay.	4 Lay.	5 Lay.	6 Lay.
ρ_1	25.695	26.564	26.645	26.673	26.682
h_1	100	8.817	5.748	11.841	13.135
ρ_2	126.04	23.919	25.177	5	5.136
h_2		50	33.399	0.786	1.891
ρ_3		51.445	5.070	31.062	185.96
h_3			5.114	25	3.391
ρ_4			70.308	6.627	5.154
h_4				15.554	14.233
ρ_5				3407.3	646.57
h_5					19.091
ρ_6					1598.2

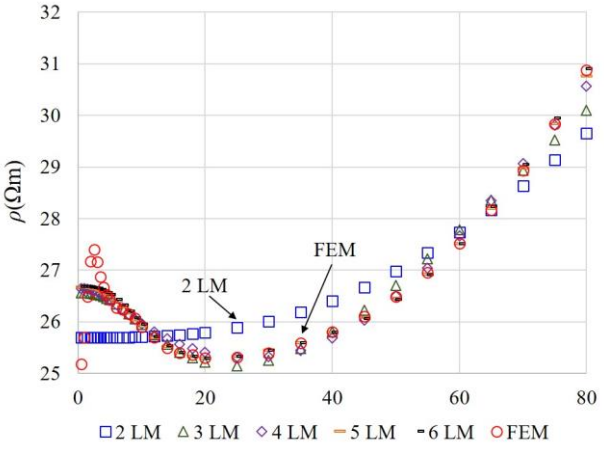

Figure 7: Calculated apparent resistances for the 2-6 layered models using the parameters from Table XI.

An optimisation method that is not appropriate for the presented problem can lead to incorrectly calculated coefficients, as was seen in the case of TLBO and DE, which got stuck in the local minimum.

Based on the presented tests, it was found out that, due to the local minima, which appeared in the case of Model B, only ABC were suitable method for all tested soil models, and it can be suggested for general use.

Based on the presented analysis, it was found out that only 3, 4, 5 and 6 LMs were suitable as universal models, and they can be suggested for general use. The 2 LM was not appropriate.

In the case of inhomogeneity, the case Model C, the horizontally layered model was able to produce results; OF was smaller than 1.5%. We could conclude that the horizontally layered model was also appropriate for inhomogeneity.

Nevertheless, in reality, it could have happened that the grounding system was appropriate in the area of the soil, but not appropriate in the area of inhomogeneity.

REFERENCES

[1] M. Trlep, A. Hamler, M. Jesenik, B. Štumberger, "The FEM-BEM analysis of complex grounding systems," IEEE Trans. Magn. vol. 39, no. 3, pp. 1155-1158, May 2003. May 2012.

[2] F. Bruckner, C. Vogler, M. Feisch, D. Praetorius, B. Bergmair, T. Hubner, M. Fuger, D. Suess, "3D FEM-BEM-coupling method to solve magnetostatic Maxwell equations," J. Magn. Magn. Mater, vol 324, pp. 1862-1866,

[3] G. R.D. Southey, M Siahrang, S. fortin, F.P. Dawalibi, "Using fall-of-potential measurements to improve deep soil resistivity estimates," *IEEE Trans. Ind. Appl.*, vol. 51, no. 6, pp. 5023-5029, Nov. 2015.

[4] IEEE Power and Energy Society, IEEE Guide for Measuring Earth Resistivity, Ground Impedance, and Earth Surface Potentials of Grounding Systems, The Institute of Electrical and Electronics Engineers, Inc, New York, 2012.

[5] B. Zhang, X. Cui, L. Li, J. He, "Parameter estimation of horizontal multilayer earth by complex image method", IEEE Trans. Power Delivery, vol. 20, no. 2, pp. 1394-1401, Apr. 2005.

[6] I.F. Gonos, I.A. Stathopulos, "Estimation of multilayer soil parameters using genetic algorithms," IEEE Trans. Power Deliv. vol. 20, no 1, pp. 100-106, Jan. 2005.

[7] R.J. He, Z.Y. Yang, "Differential evolution with adaptive mutation and parameter control using Levy probability distribution," J. Comput. Sci. Tech., vol. 27, no. 5, pp. 1035-1055, Nov. 2012.

[8] N. Veček, M. Črepinšek, M. Mernik, "On the influence of the number of algorithms, problems, and independent runs in the comparison of evolutionary algorithms," Appl. Soft Comput., vol. 54, pp. 23-45, May 2017

[9] R. Mallipeddi, P.N. Suganthan, Q.K. Pan, M.F. Tasgetiren, "Differential evolution algorithm with ensemble of parameters and mutation strategies," Appl. Soft Comput., vol. 11, pp. 1679-1696, Mar. 2011.

[10] R.V. Rao, V.J. Savsani, D.P. Vakharia, "Teaching-learning-based optimization: A novel method for constrained mechanical design optimization problems,", Comput. Aided Des., vol. 43, pp. 303-315, Mar. 2011.

[11] J.K. Pickard, J.A. Carretero, V.C. Bhavsar, "On the convergence and original bias of the teaching-learning-based-optimization algorithm," Appl. Soft Comput., vol. 46, pp. 115-127, Sept. 2016.

[12] D. Karaboga, B. Basturk, "A powerful and efficient algorithm for numerical function optimization: artificial bee colony (ABC) algorithm," J. Global Optim., vol. 39, no. 3, pp. 459-471, Apr. 2007.

[13] M. Jesenik, M. Beković, A. Hamler, M. Trlep, "Analytical modelling of a magnetization curve obtained by the measurements of magnetic materials' properties using evolutionary algorithms," Appl. Soft Comput., vol. 52, pp. 387-408, Mar. 2017.

Empirical Damping of Nonlinear Spring-Mass Systems

*Gergely Koczka and *Gerald Leber
*Siemens Energy Austria, Elingasse 3, A-8160 Weiz, Austria

***Abstract*—The simplified modelling of many physical processes results in a 2nd order ordinary differential equation system (ODE). Often the damping of these resonating systems cannot be defined in the same simplified way as the other parameters due to the complexity of the physical effects. Measurements show that empirical logarithmic damping of the resonating system is satisfying accurate in the most cases. The logarithmic damping method can be efficiently applied for linear 2nd order ODE but fails if nonlinear problems must be solved. In this paper a method will be shown, how to use the logarithmic damping method for nonlinear 2nd order ODE in time domain.**

***Index Terms*—logarithmic decrement, nonlinear ODE, short circuit forces.**

I. INTRODUCTION

Short circuit withstand of the large power transformers is crucial for the stability of the electric grid. To ensure this withstand the magnetic forces in the transformer windings must be calculated. As the windings in the large power transformers are cylindrical, a two-dimensional (2D) axisymmetric field calculation approach is satisfying accurate. During the design process the Lorentz forces [1] of the windings will be calculated for each winding disc.

The forces acting on insulation materials can be determined with the help of a spring-mass system considering the masses of the winding discs and the elastic properties of the insulation materials. The springs are highly nonlinear, as the Young's modulus of the insulation increasing with the pressure on it. Also, the insulation materials cannot transfer tensile forces, so the material model has a non-continuous characteristic (Fig. 1).

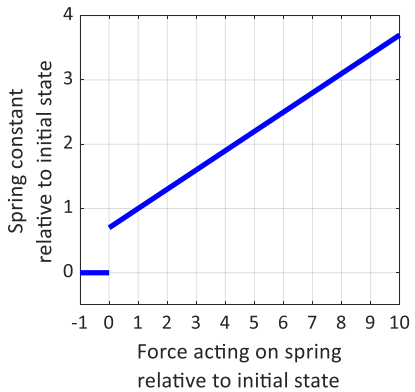

Fig. 1: Force depending spring characteristic

As the damping of the spring mass system comes from the winding disc movements in the surrounding fluid and from the fluid itself, which is pressed out from the insulation materials, it cannot be defined exactly. However, measurements show that the damping can be estimated and defined by a logarithmic decrement [2] of the resonance frequencies.

In this paper a technique will be introduced, which allows to generate the unknown damping matrix according to the predefined logarithmic decrement.

II. SPRING-MASS SYSTEM

The approximation for the dynamic winding force calculation is a quasi-one-dimensional spring-mass-system where only the axial component of the Lorentz forces is considered. Each disc of a winding can be assumed as one mass, the insulation materials between the discs are the springs. A practical force distribution in a two winding transformer is shown in Fig. 2.

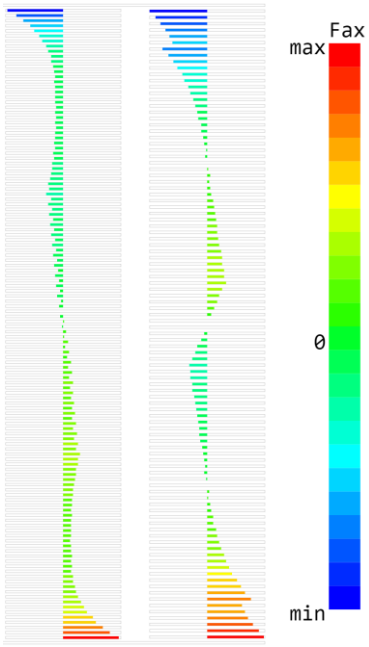

Fig. 2: Axial electromagnetic force distribution on each disc of a two winding transformer

The nonlinear ODE corresponding to the spring-mass system can be written as following:

$$\mathbf{M}\ddot{x} + \mathbf{D}\dot{x} + \mathbf{K}_{NL}x = F_{Lorentz}\,, \qquad (1)$$

where x is the displacement of the masses, $\mathbf{M}$ is a diagonal matrix containing the masses, $\mathbf{D}$ is the damping matrix, $\mathbf{K}_{NL}$ is the time dependent nonlinear spring matrix and $F_{Lorentz}$ contains the axial component of the Lorenz forces acting on each disc. $\mathbf{K}_{NL}$ depends on the nonlinear spring characteristics, and can be determined as:

$$\mathbf{K}_{NL} = \mathbf{T}^T \left[k\left(F_{sp}\right) \right] \mathbf{T} , \tag{2}$$

where **T** is the incidence matrix, $\left[k\left(F_{sp}\right) \right]$ is a diagonal matrix containing the spring parameters and F_{sp} are the forces, acting on the springs. F_{sp} depends on the momentary displacement of the masses, the spring constants and the initial (clamping) force. It can be determined as

$$F_{sp} = \left[k\left(F_{sp}\right) \right] \mathbf{T} x + F_0 , \tag{3}$$

where F_0 is the initial force acting on the springs, practically known as preclamping force.

The ODE shown in (1), is still not completely described, as the damping matrix (**D**) is still unknown. The classical damping method is the mass damping, which means that each mass has a damping coefficient. This damping method has the advantage, that the **D** matrix becomes diagonal, so the system matrix will be sparse, therefore the inversion of the system matrix is very simple and fast. The disadvantage of this damping technique is that the higher resonances won't be damped and therefore nonphysical high harmonics will be visible in the solution during the time-stepping method. To overcome this difficulty an empirical damping could be used, which damps all resonance frequencies of the system. The problem with this approach is that a nonlinear system has no defined resonances, therefore the damping must be determined on a linearized state of the original problem. This linear state can be, for example the initial state of the system where only the clamping forces are acting on the windings.

III. Linear Problem

The initial state of the problem is, where there is no displacement and therefore the spacer forces are equal to the initial forces.

$$F_{sp}\big|_{t=t_0} = F_0 , \tag{4}$$

where t_0 is the initial time, where the time-stepping method starts. The spring constants are also fixed for this timestep and the spring matrix can be written as

$$\mathbf{K} = \mathbf{K}_{NL}\big|_{t=t_0} = \mathbf{T}^T \left[k\left(F_0\right) \right] \mathbf{T} . \tag{5}$$

The linear and undamped problem has the following form:

$$\mathbf{M}\ddot{x} + \mathbf{K}x = F_{Lorentz} \tag{6}$$

As our goal is to write an equivalent ODE, which has the property that every Eigenvalue is damped with a logarithmic decrement, we need to determine the Eigenvalues and Eigenvectors of the undamped system.

$$\lambda_i^2 \mathbf{M} v_i + \mathbf{K} v_i = 0 \qquad 1 \le i \le m , \tag{7}$$

where λ_i and v_i are the i-th Eigenvalue and Eigenvector and m is the number of the Eigenvectors and Eigenvalues. As **M** and **K** are both positive definite matrixes, the Eigenvectors are real, and the Eigenvalues have the following form

$$\lambda_i = \pm j\omega_i , \tag{8}$$

where $j = \sqrt{-1}$ is the imaginary unit and ω_i is the angular frequency of the i-th resonance. Defining a logarithmic decrement [2] $0<\delta_i<1$ for every Eigenvalues, they can be modified with the help of

$$\zeta_i = \frac{\ln \delta_i}{2\pi} \tag{9}$$

as

$$\tilde{\lambda}_i = \zeta_i \omega_i \pm \frac{j\omega_i}{\sqrt{1+\zeta_i^2}} . \tag{10}$$

The 2nd order Eigenvalue problem, which corresponds to the modified Eigenvalues can be written as:

$$\tilde{\lambda}_i^2 \mathbf{M} v_i + \tilde{\lambda}_i \tilde{\mathbf{D}} v_i + \tilde{\mathbf{K}} v_i = 0 , \tag{11}$$

where $\tilde{\mathbf{D}}$ is the damping matrix and $\tilde{\mathbf{K}}$ is the modified spring matrix. (11) can be written in matrix form by introducing the matrixes

$$V = \left[v_1 \ldots v_m \right] \tag{12}$$

containing all Eigenvectors of (7), and

$$\left[\tilde{\lambda} \right] = \begin{bmatrix} \tilde{\lambda}_1 & & \\ & \ddots & \\ & & \tilde{\lambda}_m \end{bmatrix} \tag{13}$$

a diagonal matrix containing all Eigenvectors of (7). Using (12) and (13) then equation (11) has the following form:

$$\mathbf{M} V \left[\tilde{\lambda} \right]^2 + \tilde{\mathbf{D}} V \left[\tilde{\lambda} \right] + \tilde{\mathbf{K}} V = 0 . \tag{14}$$

Multiplying (14) from right with V^T and using the condition $\tilde{\mathbf{D}}$ and $\tilde{\mathbf{K}}$ are real symmetric matrixes, an iterative residual method can be written as show in Table I.

TABLE I
PSEUDO CODE TO DETERMINE THE DAMPING MATRIX

1	$s=0 \qquad \tilde{\mathbf{D}}^{(0)}=0 \qquad \tilde{\mathbf{K}}^{(0)}=\mathbf{K}$
2	$\tilde{\mathbf{D}}^{(s+1)}=-re\left(\left(\mathbf{M}V\left[\tilde{\lambda}\right]^2V^T+\tilde{\mathbf{K}}^{(s)}VV^T\right)\left(V\left[\tilde{\lambda}\right]V^T\right)^{-1}\right)$
3	$\tilde{\mathbf{K}}^{(s+1)}=-re\left(\left(\mathbf{M}V\left[\tilde{\lambda}\right]^2V^T+\tilde{\mathbf{D}}^{(s+1)}V\left[\tilde{\lambda}\right]V^T\right)\left(VV^T\right)^{-1}\right)$
4	$s:=s+1$
5	If not converged, continue by step 2.

As the left and right Eigenvectors of a symmetric Eigenvalue problem are the transposed of each other, it can be shown, that the resulting $\tilde{\mathbf{D}}$ and $\tilde{\mathbf{K}}$ matrixes are symmetric [3]. The equivalent modified linear ODE can be written as

$$\mathbf{M}\ddot{x}+\tilde{\mathbf{D}}\dot{x}+\tilde{\mathbf{K}}x=F_{Lorentz} \tag{15}$$

The empirical damping method can be used without determine the equivalent modified ODE, if e.g. the Duhamel's integral [4] is used for solving a linear ODE. To use other analytical linear ODE solvers (e.g. the method of variation of parameters [5]) the determination of the damping matrix could be necessary. The nonlinear ODE cannot be solved analytically therefore the determination of the equivalent ODE is also necessary.

IV. NONLINEAR PROBLEM

After determining the damping matrix and the modified spring matrix, the nonlinear 2nd order ODE can be formulated as

$$\mathbf{M}\ddot{x}+\tilde{\mathbf{D}}\dot{x}+\left(\tilde{\mathbf{K}}-\mathbf{K}+\mathbf{K}_{NL}\right)x=F_{Lorentz}\,. \tag{16}$$

A disadvantage of the empirical damping method, that both the damping matrix and the modified spring matrix is a full dense matrix. Due to the non-continuous spring characteristics a Newton-Raphson iteration for the nonlinearity cannot be applied. The nonlinearity is handled with fixed point method. To overcome the unnecessary expensive system matrix inversion a sparse fixed-point damping matrix ($\mathbf{D}_{FP}$) and a sparse fixed-point spring matrix ($\mathbf{K}_{FP}$) will be introduced. The reformulated ODE has the following form:

$$\begin{aligned}\mathbf{M}\ddot{x}+\mathbf{D}_{FP}\dot{x}+\mathbf{K}_{FP}x=F_{Lorentz}+\\ \left(\mathbf{D}_{FP}-\tilde{\mathbf{D}}\right)\dot{x}+\\ \left(\mathbf{K}_{FP}-\tilde{\mathbf{K}}+\mathbf{K}-\mathbf{K}_{NL}\right)x\end{aligned} \tag{17}$$

Practical calculations have shown that the contraction property of the fixed-point method can be ensured if the fixed-point matrixes are chosen as follows:

1) The fixed-point damping matrix

The fixed-point damping matrix with the same sparse structure as the initial spring matrix, but with the values of the damping matrix:

$$\mathbf{D}_{FP,ij}=\begin{cases}\tilde{\mathbf{D}}_{ij} & \mathbf{K}_{ij}\neq 0\\ 0 & \mathbf{K}_{ij}=0\end{cases} \tag{18}$$

2) The fixed-point spring matrix

To ensure the convergence of the fixed-point iteration the fixed-point spring matrix should be recalculated in each time-step as follows:

$$\mathbf{K}_{FP}(t)=\mathbf{T}^T\left[k\left(\max_{q\in[t_0,t]}\left\{F_{SP}(q)\right\}\right)\right]\mathbf{T}\,, \tag{19}$$

i.e. using for each spring its maximal parameter, which appeared during the time-stepping method until the actual timestep.

To solve the 2nd order ODE in (17) the Newmark method [6] was applied.

V. NUMERICAL RESULTS

In this chapter the already mentioned and explained two damping methods (mass damping and the empirical damping) will be compared in one numerical example.

The example, which was used for the comparison, was a 300MVA, 60Hz generator step-up transformer with a low-voltage (LV) and a high-voltage (HV) winding. The spring-mass model contains 430 masses. The peaks of axial force distribution of the windings were already shown in Fig. 2. The exciting forces are determined by the time-functions of currents in the winding discs and the magnetic flux density in the conductors. In steady state the forces have double frequency of the currents, although at the beginning for worst-case calculation the transient effect will be considered (see Fig 3.)

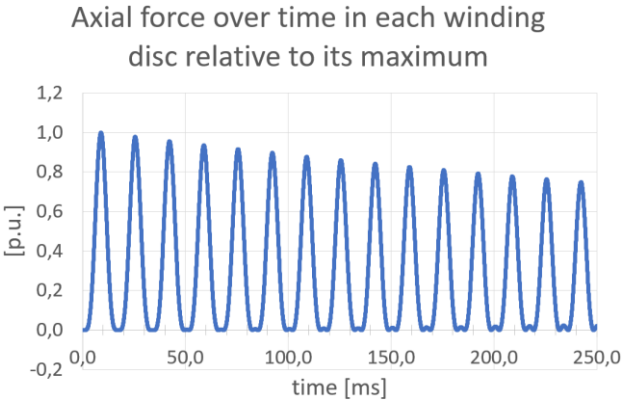

Fig. 3: Force functions over time

Each force function over time has a similar form. It can slightly change due to the phase of the current, depending on the current distribution in parallel conductors.

1) Mass damping

As already mentioned, the mass damping has only sparse matrixes, but the resonances are damped poorly in the high frequency range. The frequency depending logarithmic decrement is plotted in Fig. 4.

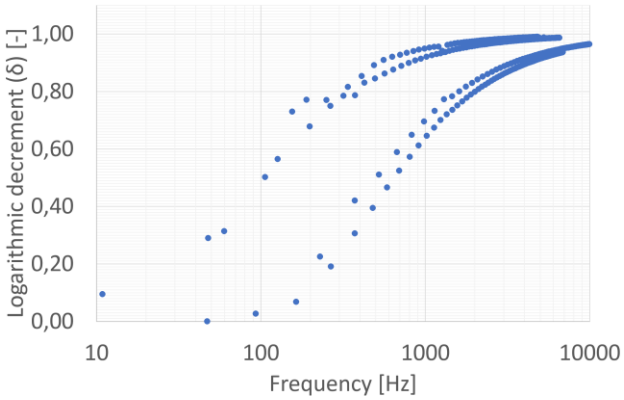

Fig. 4: Logarithmic decrement of the mass damping method depending on resonance frequencies

The disadvantage of this method is clearly visible. Due to the non-continuous spring characteristic of the insulation materials each resonance will be excited during the time-stepping method. The higher frequencies are not damped, so unphysically oscillation will be visible in the resulting time functions.

2) Empirical damping

The time consuming matrix inversion has been overcome with the introduction of the fixed-point damping matrix and the fixed-point spring-matrix. However, on the right-hand-side a dense matrix-vector multiplication must be carried out in each iteration step. Even so, due to the well-damped high frequencies, the overall solution time of the nonlinear ODE is more than 2.5 times faster as the mass damping method.

For both damping method 5 periods of the base-frequency (60Hz) have been calculated (83.33ms) and the logarithmic decrement of 0.6 was chosen for the empirical damping. The run-times and the iteration numbers of the time-stepping methods are compared in Table II.

TABLE II
COMPARISON OF DAMPING METHODS

	Mass damping	Empirical damping
No. time steps	115 200	28 800
No. fixed-point iterations	1 091 774	359 559
Average fixed-point iteration per time step	9.48	12.48
Rum-time [s]	537.0	201.8

To show the differences in the results of the two damping methods, the displacement of the winding end support structure (Fig. 5) and the force acting on the insulation materials in the axial center of the outer winding (HV) (Fig. 6) will be compared.

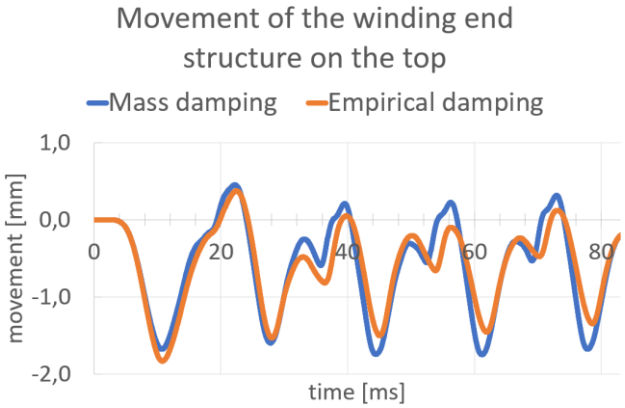

Fig. 5: displacement of the common structure over the windings

The movement of the winding end support structure is very similar from the two calculations. The main resonances are the same and the peak values have also maximal 3,16% difference.

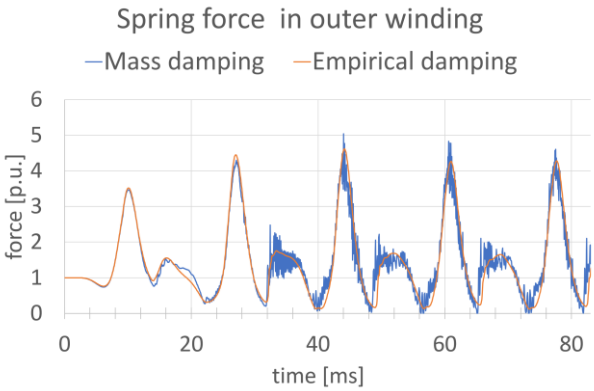

Fig. 6: forces acting at the axial center in the outer (HV) winding relative to the clamping force

The comparison of the forces between the two method shows that after the first period (16.67ms) the poorly damped high frequencies in the mass damping method are dominating during the calculation. Whereas the empirical damping has a smooth result during the whole calculation period. The high frequency resonances are not only visible in the time-domain, but also across the windings too. Fig. 7 demonstrates the spring forces across the windings at the 66.67ms.

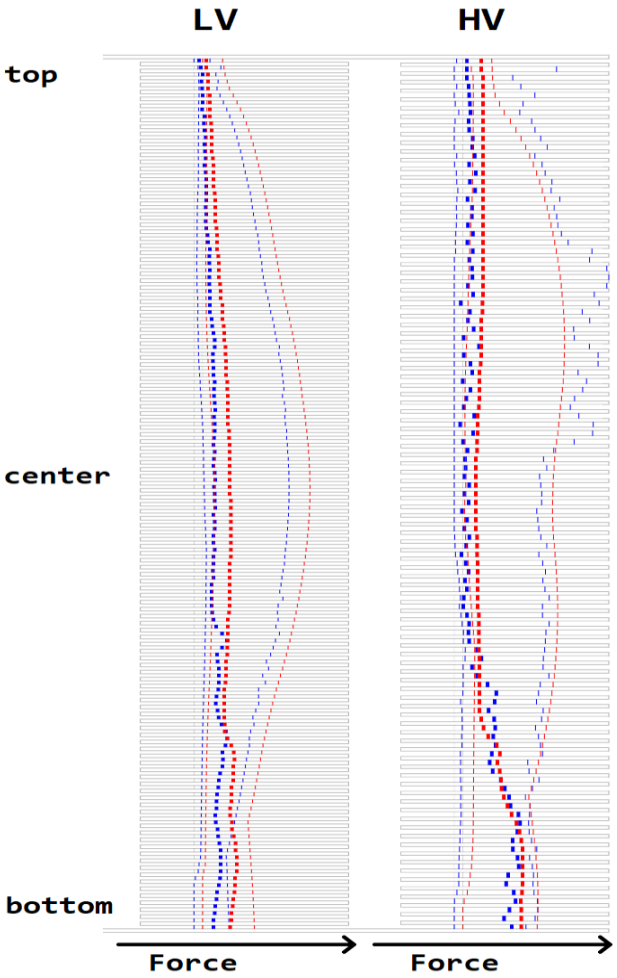

Fig. 7: spring (spacer) forces along the windings at 66,67ms
Bold blue lines: the spacer forces of mass damping method
Thin blue lines: the minimum and maximum spacer forces over the calculation period of mass damping
Bold red lines: the spacer forces of empirical damping method
Thin red lines: the minimum and maximum spacer forces over the calculation period of empirical damping

VI. Conclusion

A new numerical approach was presented to define a damping for nonlinear spring-mass systems, where the damping of the simplified model cannot be determined. The results were compared to a classical mass damping method. It was shown, that from engineering point of view, the results have small deviations. Due to the mathematical properties of the empirical damping, it is more efficient, it does not need as fine time-discretization compared to the mass damping method.

References

[1] Griffiths, David J. “Introduction to electrodynamics,” *Prentice Hall*, 1999, 3rd ed.
[2] Inman, Daniel J., "Engineering Vibration," *Upper Saddle, NJ: Pearson Education, Inc.*, 2008, pp. 43-48.
[3] J. H. Wilkinson, "The Algebraic Eigenvalue Problem," *Oxford, Clarendon Press*, 1965
[4] Fritz John, "Partial Differential Equations," *New York, Springer-Verlag,* 1982, 4th ed.
[5] Boyce, W. E.; DiPrima, R. C., "Elementary Differential Equations and Boundary Value Problems 8th Edition," *Wiley Interscience*, 1965, pp. 186–192, 237–241.
[6] Newmark, Nathan M., "A method of computation for structural dynamics," *Journal of the Engineering Mechanics Division*, 1959, 85 (EM3): 67–94

Measurement and modeling of effective cable parameters of unshielded conductors

Hollaus Karl (1), Bauer Susanne (2), Leumüller Michael (3), Türk Christian (4)

(1) Institute for Analysis and Scientific Computing, Technische Universitat Wien, Wien, Austria and Silicon Austria Labs GmbH, Graz, Austria
(2) IGTE, TU Graz, Graz, Austria
(3) Technische Universität Wien, Wien, Austria
(4) BMLV, Wien, Austria)

Purpose:

Cables are ubiquitous in electronic-based systems. Electromagnetic emission of cables and crosstalk between wires is an important issue in electromagnetic compatibility and is to be minimized in the design phase. To facilitate the design, models of different complexity and accuracy, for instance, circuit models or finite element (FE) simulations, are used. The purpose of this study is to compare transmission line parameters obtained by measurements and simulations.

Design/methodology/approach:

Transmission line parameters were determined by means of measurements in the frequency and time domain and by FE simulations in the frequency domain and compared. Finally, a Spice simulation with lumped elements was performed.

Findings:

The determination of the effective permittivity of insulated wires seems to be a key issue in comparing measurements and simulations.

Originality/value:

A space decomposition technique for a guided wave on an infinite configuration with constant cross-section has been introduced, where an analytic representation in the direction of propagation is used, and the transversal fields are approximated by FEs.

Keywords:

Time-domain-reflectometry (TDR), Numerical simulation, Cable parameter extraction, Finite element method (FEM), Spice, Circuit analysis, S-parameter analysis

Published in COMPEL - The international journal for computation and mathematics in electrical and electronic engineering, Vol. 41 No. 3, 2022, ISSN 0332-1649, page 1041 - 1051

Steady state solution of NFC model with nonlinear load using PEEC

Kvasnicka Samuel (1,2), Bauernfeind Thomas (1), Baumgartner Paul (1), Torchio Riccardo (3)

(1) Institute of Fundamentals and Theory in Electrical Engineering, Faculty of Electrical and Information Engineering, Graz University of Technology, Graz, Austria
(2) Silicon Austria Labs, TU-Graz SAL GEMC Lab, Graz, Austria
(3) Dipatimento di Ingegneria Industriale, Universita degli Studi di Padova, Padova, Italy

Purpose:

The purpose of this paper is to show that the computation of time-periodic signals for coupled antenna-circuit problems can be substantially accelerated by means of the single shooting method. This allows an efficient analysis of nonlinearly loaded coupled loop antennas for near field communication (NFC) applications.

Design/methodology/approach:

For the modelling of electrically small coupled field-circuit problems, the partial element equivalent circuit (PEEC) method shows to be very efficient. For analysing the circuit-like description of the coupled problem, this paper developed a generalised modified nodal analysis (MNA) and applied it to specific NFC problems.

Findings:

It is shown that the periodic steady state (PSS) solution of the resulting differential-algebraic system can be computed very time efficiently by the single shooting method. A speedup of roughly 114 to conventional transient approaches can be achieved.

Originality/value:

The present paper explores the implementation and application of the shooting method for nonlinearly loaded coupled antenna-circuit problems based on the PEEC method and shows the efficiency of this approach.

Keywords:

Circuit analysis, Transient analysis, Time-domain modelling, Equivalent circuit model, Computational electromagnetics, Field circuit models, Near field communication, Nonlinear resistive loads, Full-wave rectifier, Partial element equivalent circuit method,Modified nodal analysis, Differential-algebraic equation, Backward differentiation formula, Single shooting method

Published in COMPEL - The international journal for computation and mathematics in electrical and electronic engineering, Vol. 41 No. 3, 2022, ISSN 0332-1649, page 840 - 851

Optimization of particle trajectories inside an ion-thruster

Andras Reichardt* and Arpad L. Makara*

*Department of Broadband Infocommunication and Eletromagnetic Theory,
BUTE, Egry Jozsef u. 18, H-1111 Budapest
e-mail: reichardt.andras@vik.bme.hu

***Abstract*—We present optimization of trajectories of particles that fly from vacuum chamber to the outer world. Expected trajectories are defined by control point regions that must be entered. We present a simple electrostatic model for the system of electrodes. Potentials are calculated using a supervised machine learning (SML) algorithm.**

***Index Terms*—electrostatic approximation, ion thruster, optimization, particle trajectory**

I. Introduction and motivation

First we introduce our motivation and background used in that paper. Here we present our results about optimization of ion trajectories inside an ion thruster's nozzle region to be able to control very small satellites. In the recent years a lot of small satellites are already launched or planned to launch designed and manufactured at our department (MaSat-1, SMOG-P[1], ATL-1 [2]).

After launching a small satellite and placing it into its final orbit, it can have unwanted and uncontrolled rotation. Therefore, a small satellite needs to perform some maneuvers to stabilize or slightly change its orbit position. Due to its small size, it needs only a small drive system and torque to stabilize. Furthermore, the available energy for attitude control is also limited. In this paper, we focus on tiny satellites with a size of 2-3 U in terms of PocketCube standards. Satellites' small size and mass involves that relatively small force is enough to control such a vehicle compared to thrust needed to put them on to orbit[3], [4].

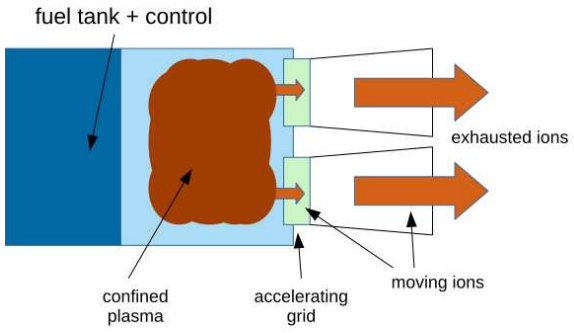

Fig. 1. Schematic of an ion thruster engine

A possible way to steer and stabilize a tiny satellite is using an ion thruster. An ion-thruster is an accelerator that uses Xenon or Iodine to produce positively or negatively charged ions[5], [6]. Ions generated in an ion-chamber using electric field. Xenon is stored in the fuel tank (shown on Fig. 1). Generated ions are accelerated using a pair electrostatic grids called accelerator grid ot fly out to the nozzle of the thruster. Nozzles surface can be used to control electrically the ion beams that flows out from the nozzle. If we control ion beams we can steer the satellite.

In an earlier paper [7] we showed that using a simple pair of electrodes control of beam trajectories can be achieved[7]. The electrodes are on the inner surface of nozzle and its potential can be varied relatively to the potential of AG. During launch of satellite the nozzles are packed up and only after the satellite is set on orbit are unwraped.

Optimization are needed to set ion beams to a prescibred path that are defined using points and weights. These points has to be touched as much as possible flying from first point (start point) toward the last point.

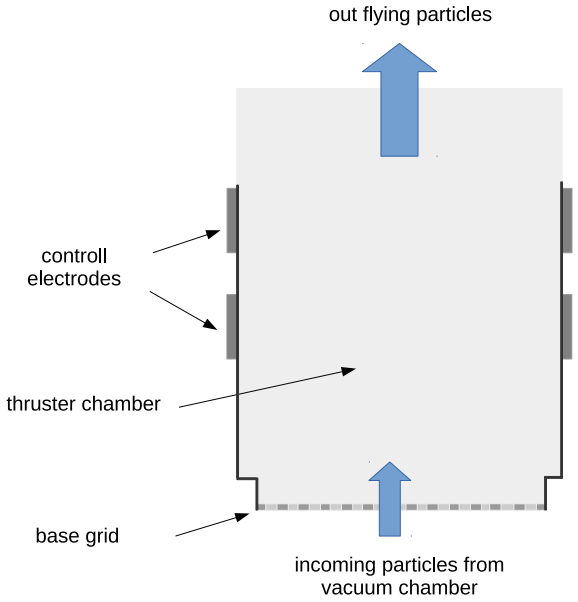

Fig. 2. Outline of the nozzle, wall of nozzle is non-conducting

The paper is organized as follows. In Section II. we propose our model of the electromagnetic problem. Thereafter in Section III we show optimization and supervized machine learning method we used. Results are shown for some cases in Section IV and a summary is given at the end in SectionV.

II. Electromagnetic model of the direct problem

Ions that enter nozzle have a high longitudinal velocity. Therefore the electromagnetic field created by control electrodes can be modeled as a constant field with very slow change in time[8]. In time that ion flies through nozzle the field do not change. Effect of ions to each other neglected just like effect of external magnetic fields. Geometry is shown on Fig. 3 where base electrode is the upper side of the acceleration grid (AG), electrodes are the control electrodes with variable potential. Simulation region is a great volume around nozzle to avoid side effects.

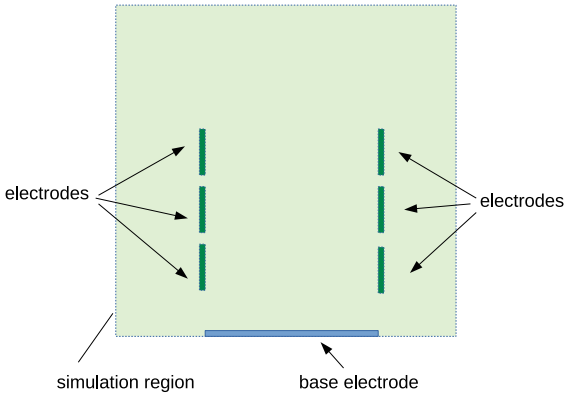

Fig. 3. Geometry of simulated rectangular shaped nozzle

The model that describes electromagnetics of the physical system is an electrostatic model[9]. Potential of the control electrodes (these electrodes are on the surface of nozzle, dark green rectangles on Fig. 3) and potential of base electrode (top electrode of the accelerator grid between plasma chamber and nozzle, blue region on Fig. 3) are specified.

Our goal is to solve this electrostatic model using FEM to calculate potential inside the nozzle. As the potential is known, any trajectory of a charged particle can be calculated[10].

In the simulation region we solve Laplace-eqation (1) with boundary conditions on base electrode ($\varphi = V_0$) and control electrodes ($\varphi = V_i$).

$$\nabla \varepsilon \nabla \varphi = 0 \tag{1}$$

On the border of simulation region homogeneous Neumann condition were used. After solving this model we can calculate any trajectory of ions that start from base electrode solving equation of motion (2) with force calculated from potential (3), where

$$m_{\text{ion}} \cdot \frac{\mathrm{d}^2 \mathbf{r}}{\mathrm{dt}^2} = \mathbf{F} \tag{2}$$

$$\mathbf{F} = (-1) \cdot q_{\text{ion}} \cdot \nabla \varphi \tag{3}$$

Geometrical parameters of nozzle as shown on Fig. 2 are determined by size limits of the satellite and fixed in

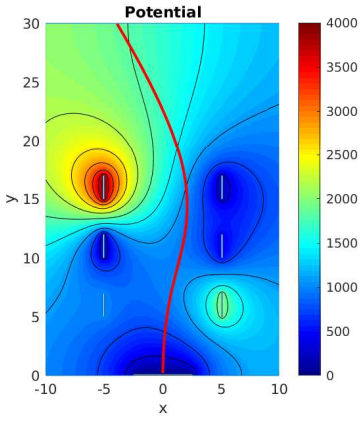

Fig. 4. Electrostatic potential simulated (colored contour) and particle trajectory (red line)

simulations. All supporting structures of the electrodes are made of thin insulator rods and in a normal operation ions do not collide them.

III. Some words about optimization and machine learning

Nowadays, Artificial Intelligence (AI) is a popular buzzword, and many efforts are made to use everywhere. There are specialized computers that offer built-in support for AI-like problems. Our goal using AI was to formulate and prototype this problem from the AI viewpoint. Using these special computers, the calculation of control voltages for satellite trajectory correction could be calculated in real-time.

A. Definition of optimal trajectory

Goal of optimization was to determine voltages of control electrodes to achieve that ionbeams that flows out of nozzle follows a prescribed path inside the nozzle. Path of ionbeams are defined through definition of points and weights along the required path (see Fig. 6).

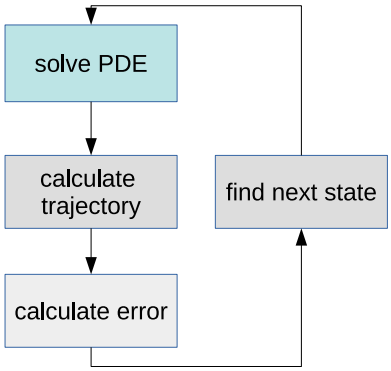

Fig. 5. Schmetic flow chart of the optimization process. Red line indicates trajectory of ion that flies out of acceleration grid. Color contour shows contour plot of electrostatic potential.

Start point of all ions is on the outer surface of acceleration grid (AG). Final point is the point where

ion leaves nozzle. Inside points (control points, CPs) are defined too. A possible configuration is shown on Fig. 6.

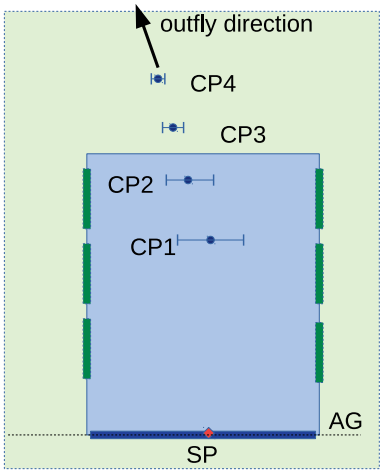

Fig. 6. Control points defined inside and outside of nozzle. Electrodes (green rectangles), top of acceleration grid (AG, blue) and starting point (SP, red) shown. Width of control points are inversely proportional to the weight of them. Wide point means low weight. Light blue region means "geometrical" definition of the nozzle.

Error function is based on deviation of trajectory from control points. Ions have a high velocity perpendicular to the plane of AG's surface it is leaved. Derivation of ion trajectory from CP is calculated with a horizontal distance.

At the k[th] CP the error-function is $|x_k - x_{k,pre}|$, where x_k is horizontal coordinate of ion and $x_{k,pre}$ is horizontal coordinate of the control point. Other error-functions can be used in case of other problems, but in this case one used was the best.

Total error-function is calculated as follows :

$$\langle \text{error} \rangle = \sum_{k=1}^{N} p_k \cdot |x_k - x_{k,pre}| \qquad (4)$$

where p_k is weigth of kth CP. Using a weights some CPs can be defined as more important than others.

B. Optimization as a machine learning problem

There are a lot of different techniques in machine learning (ML)[12], [13]. We have chosen supervised machine learning (SML) to solve this problem. SML differs from "simple" ML to have a goal-function (or error-function) defined and used to characterize the state.

SML is an iterative process, as shown in Fig. 5. We define a $\mathbf{W}$ parameter vector that contains all the potentials of electrodes. In every step a guess is made using (5) and next $\mathbf{W}$ is chosen. Error is calculated using (4). Iteration stops if the maximum number of iterations reached or the error is less than the limit.

$$\mathbf{W_{next}} = \mathbf{W_{prev}} + 2 \cdot \mu \cdot \langle \text{error} \rangle \cdot p \qquad (5)$$

where $\mathbf{W}$ is parameter-vector, μ learning-factor, $\langle \text{error} \rangle$ is sum of errors at all control points, p is scaling factor.

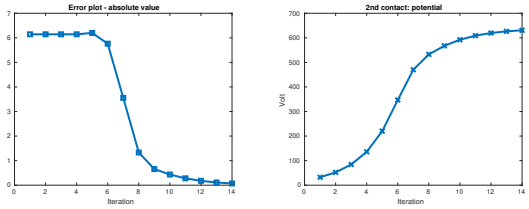

Fig. 7. Errors calculated (measured) after every steps of optimization on the left. Voltage of the 2nd contact is shown on the right in case of the same optimization process.

Learning-factor should be less than $1/2$. Its value is important because if it is small, then convergence is slow, or a "solution" easier can be stucked in a shallow local minimum. A high learning factor can cause large steps in convergence, but sometimes it can cause non-convergence of the process.

IV. Results of optimization work

We analyzed a setup of 6 electrodes in use with a symmetrical arrangement. Ions are started from the top of the base electrode (middle of base electrode used as the origo of coordinate system). Using a low learning-factor (0.05) a moderate error-function is generating (shown on Fig. 7).

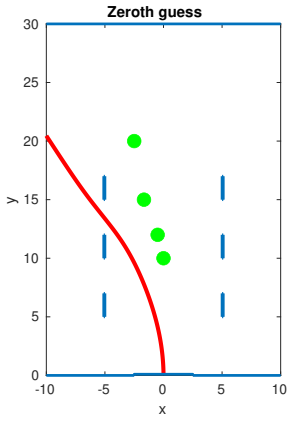

Fig. 8. Trajectory of an ionbeam before after optimization steps. Green disks are control points (1st point not shown, starting point), red line indicates trajectory of ionbeam, electrodes are shown as blue rectangles.

Initial guess of electrode potentials were selected randomly, the resulting trajectory is shown on the Fig. 8. After a few iteration steps the trajectory takes up its best way, show on Fig. 9. Control points (green disks) can have different weights, points that are closer to the end of nozzle have higher weights because they give the main curve of the outflying path. As it can be seen this guess has some big problems and couldn't be realizable.

After optimization the trajectory is shown on Fig. 9. Path of ions follows the predescribed route.

We found that number of electrode-pairs determines the possible control points. If we choose nearly the same number of control points as the number of electrode-pairs then optimization will have a good output in terms

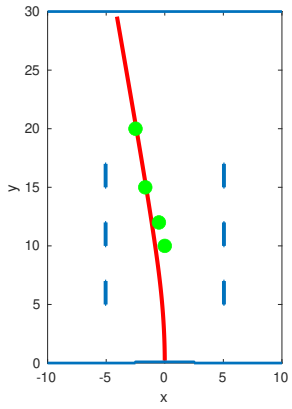

Fig. 9. Trajectory of an ionbeam after optimization steps. Notations are the same as on Fig. 8.

of error defined earlier. Of course not all routes can be realized because the ions have inertia and it doesn't allow arbitrary changes in direction.

Our simulations were performed in a two-dimensional environment that used the symmetry of the rectangular shape nozzle, so control of ionbeams are available only in one direction.

V. Summary

In this paper, we solved the problem of optimizing control electrodes' potential to drive ion-beam on the prescribed path. Optimization is realized using a machine-learning algorithm to be able to realize on special hardware later. It was shown that control of the ion-beam trajectory could be done due to the adjustment of electrodes' potential.

SML is highly sensible to start point of the parameter vector, and human supervision is needed sometimes. Since SML finds only local minima, therefore, perturbing start parameter vector should sometimes be carried out.

In the future, we plan to use special hardware for implementation three-dimensional simulation of the structure to analyze selectivity of the trajectory control.

Solution of this kind of problem can give guidance for the designers how to choose the appropriate number and location of the control electrode to achieve maximum maneuverability of tiny satellites.

The solution's computational cost in case of a three dimensional direct problem is much greater than of this two-dimensional problem therefore this simple guess can be a good initial state of the further (3d) solutions.

References

[1] SMOG-1, Official Site, http://gnd.bme.hu/smog
[2] J. McDowell, List of all known satellites launched, http://planet4589.org/space/log/launchlog.txt
[3] Arianespace, Ariane 5 Users Manual Issue 5 Revision 2, October, 2016.
[4] Wilfried Ley, Klaus Wittmann and Willi Hallmann (ed): Handbook of Space Technology, Wiley, 2009.
[5] Choueiri, Edgar Y (2009). "New dawn of electric rocket". Scientific American. 300 (2): 5865.
[6] Martinez-Sanchez, M., Pollard, J.E. Spacecraft Electric Propulsion An Overview. J. Propul. Power, 14 (5), 688693, 1998.
[7] A. Makara, A. Reichardt and L. Csurgai-Horvath, "Visualization and simulation of ion thrusters possibly usable by small satellites", H-SPACE2020, Budapest, 2020
[8] Jahn, Robert G. (1968). Physics of Electric Propulsion (1st ed.). McGraw Hill Book Company
[9] K. Simonyi, "Theoretische Elektrotechnik", Leipzig : Barth, 1993.
[10] R. Hockney, J. Eastwood, "Computer Simulation Using Particles", IOP, New York, 1989.
[11] Jahn, Robert G. (1968). Physics of Electric Propulsion (1st ed.). McGraw Hill Book Company
[12] Kevin P. Murphy, "Machine Learning A Probabilistic Perspective", 2012, MIT Press
[13] Martin T. Hagan et al., "Neural Network Design" , 2nd ed., E-Book, 2014

A mixed multiscale FEM for the eddy current problem with T,- and vector hysteresis

Hanser Valentin, Schöbinger Markus, Hollaus Karl

Institute of Analysis and Scientific Computing, Technische Universität Wien, Vienna, Austria

Purpose:

This work introduces an efficient and accurate technique to solve the eddy current problem in laminated iron cores considering vector hysteresis.

Design/methodology/approach:

The mixed multiscale finite element method based on the based on the T,- formulation, with the current vector potential T and the magnetic scalar potential allows the laminated core to be modelled as a single homogeneous block. This means that the individual sheets do not have to be resolved, which saves a lot of computing time and reduces the demands on the computer system enormously.

Findings:

As a representative numerical example, a single-phase transformer with 4, 20 and 184 sheets is simulated with great success. The eddy current losses of the simulation using the standard finite element method and the simulation using the mixed multiscale finite element method agree very well and the required simulation time is tremendously reduced.

Originality/value:

The vector Preisach model is used to account for vector hysteresis and is integrated into the mixed multiscale finite element method for the first time.

Keywords:

Electromagnetic fields, Finite element method, Eddy currents, Magnetic hysteresis, Lamination modelling, Homogenization method, Mixed potential formulation, Eddy current problem, Mixed multiscale finite element method, Vector Preisach model

Published in COMPEL - The international journal for computation and mathematics in electrical and electronic engineering, Vol. 41 No. 3, 2022, ISSN 0332-1649, page 852 - 866

Application of model order reduction with Cauer ladder networks to industrial inductors

Koester Niels (1), Koenig Oliver (2), Thaler Alexander (1), Bíró Oszkár (3)

(1) Department E: Electrics/Electronics and Software, VIRTUAL VEHICLE Research Center, Graz, Austria
(2) Product Development Control Systems, LGCO, Graz, Austria
(3) Institute of Fundamentals and Theory in Electrical Engineering, Graz, Austria

Purpose:

The Cauer ladder network (CLN) model order reduction (MOR) method is applied to an industrial inductor. This paper aims to to anaylse the influence of different meshes on the CLN method and their parameters.

Design/methodology/approach:

The industrial inductor is simulated with the CLN method for different meshes. Meshes considering skin effect are compared with equidistant meshes. The inductor is also simulated with the eddy current finite element method (ECFEM) for frequencies 1kHz to 1MHz. The solution of the CLN method is compared with the ECFEM solutions for the current density in the conductor and the total impedance.

Findings:

The increase of resistance resulting from the skin effect can be modelled with the CLN method, using a uniform mesh with elements much larger than the skin depth. Meshes taking account of the skin depth are only needed if the electromagnetic fields have to be reconstructed. Additionally, the convergence of the impedance is used to define a stopping criterion without the need for a benchmark solution.

Originality/value:

The work shows that the CLN method can generate a network, which is capable of mimicking the increase of resistance usually accompanied by the skin effect without using a mesh that takes the skin depth into account. In addition, the proposed stopping criterion makes it possible to use the CLN method as an a priori MOR technique.

Keywords:

Cauer ladder networks, Eddy current problem, Finite element method, Model order reduction, Electromagnetic fields, Eddy currents, Equivalent circuit model

Published in COMPEL - The international journal for computation and mathematics in electrical and electronic engineering, Vol. 41 No. 3, 2022, ISSN 0332-1649, page 867 - 877

Towards real-time magnetic dosimetry simulations for inductive charging systems

Haussmann Norman (1), Zang Martin (1), Mease Robin (1), Clemens Markus (1), Schmuelling Benedikt (2), Bolten Matthias (3)

(1) Chair of Electromagnetic Theory, University of Wuppertal, Wuppertal, Germany
(2) E-Mobility Research Group, University of Wuppertal, Wuppertal, Germany
(3) Chair of Scientific Computing and High Performance Computing, University of Wuppertal, Wuppertal, Germany

Purpose:

Inductive charging systems for electrically powered cars produce a magneto-quasistatic field and organism in the vicinity might be exposed to that field. Magneto-quasistatic fields induce electric fields in the human body that should not exceed limits given by the International Commission of Non-Ionizing Radiation protection (ICNIRP) to ensure that no harm is done to the human body. As these electric fields cannot be measured directly, they need to be derived from the measured magnetic flux densities. To get an almost real-time estimation of the harmfulness of the magnetic flux density to the human body, the electric field needs to be calculated within a minimal computing time. The purpose of this study is to identify fast linear equations solver for the discrete Poisson system of the Co-Simulation Scalar Potential Finite Difference scheme on different graphics processing unit systems.

Design/methodology/approach:

The determination of the exposure requires a fast linear equations solver for the discrete Poisson system of the Co-Simulation Scalar Potential Finite Difference (Co-Sim. SPFD) scheme. Here, the use of the AmgX library on NVIDIA GPUs is presented for this task.

Findings:

Using the AmgX library enables solving the equation system resulting from an ICNIRP recommended human voxel model resolution of 2mm in less than 0.5s on a single NVIDIA Tesla V100 GPU.

Originality/value:

This work is one essential advancement to determine the exposure of humans from wireless charging system in near real-time from in situ magnetic flux density measurements.

Keywords:

Inductive power transfer, Finite difference method, GPU computing, Inductive charging, Magnetic dosimetry, Real-time

Published in COMPEL - The international journal for computation and mathematics in electrical and electronic engineering, Vol. 41 No. 3, 2022, ISSN 0332-1649, page 878 - 888

Topology optimization of magnetic cores for WPT using the geometry projection method

Otomo Yoshitsugu, Igarashi Hajime

Graduate School of Information Science and Technology, Hokkaido University, Sapporo, Japan

Purpose:

The purpose of this study is to search for an optimal core shape that is robust against misalignment between the transmitting and receiving coils of the wireless power transfer (WPT) device. During the optimization process, the authors maximize the coupling coefficients while minimizing the leakage flux around the coils to ensure the safety of the WPT device.

Design/methodology/approach:

In this study, a novel topology optimization method for WPT devices using the geometry projection method is proposed to optimize the magnetic core shape. This method facilitates the generation of bar-shaped magnetic cores because the material distribution is represented by a set of elementary bars.

Findings:

It is shown that an optimized core shape, which is obtained through topology optimization, effectively increases the net magnetic flux interlinked with the receiving coil and outperforms the conventional core.

Originality/value:

In the previous topology optimization method, the material distribution is represented by a linear combination of Gaussian functions. However, this method does not usually result in bar-shaped cores, which are widely used in WPT. In this study, the authors propose a novel topology optimization method for WPT devices using geometry projection that is used in structural optimization, such as beam and cantilever shapes.

Keywords:

Geometry projection method, Robust optimization, Topology optimization, Wireless power transfer (WPT), Robust design

Published in COMPEL - The international journal for computation and mathematics in electrical and electronic engineering, Vol. 41 No. 3, 2022, ISSN 0332-1649, page 889 - 899

Deep learning-based surrogate model for fast multi-material topology optimization of IPM motor

Sato Hayaho, Igarashi Hajime

Graduate School of Information Science and Technology, Hokkaido University, Sapporo, Japan

Purpose:

This paper aims to present a deep learning–based surrogate model for fast multi-material topology optimization of an interior permanent magnet (IPM) motor. The multi-material topology optimization based on genetic algorithm needs large computational burden because of execution of finite element (FE) analysis for many times. To overcome this difficulty, a convolutional neural network (CNN) is adopted to predict the motor performance from the cross-sectional motor image and reduce the number of FE analysis.

Design/methodology/approach:

To predict the average torque of an IPM motor, CNN is used as a surrogate model. From the input cross-sectional motor image, CNN infers dq-inductance and magnet flux to compute the average torque. It is shown that the average torque for any current phase angle can be predicted by this approach, which allows the maximization of the average torque by changing the current phase angle. The individuals in the multi-material topology optimization are evaluated by the trained CNN, and the limited individuals with higher potentials are evaluated by finite element method.

Findings:

It is shown that the proposed method doubles the computing speed of the multi-material topology optimization without loss of search ability. In addition, the optimized motor obtained by the proposed method followed by simplification for manufacturing is shown to have higher average torque than a reference model.

Originality/value:

This paper proposes a novel method based on deep learning for fast multi-material topology optimization considering the current phase angle.

Keywords:

Permanent magnet machine, Topology optimization

Published in COMPEL - The international journal for computation and mathematics in electrical and electronic engineering, Vol. 41 No. 3, 2022, ISSN 0332-1649, page 900 - 914

Magnetic field simulations using explicit time integration with higher order schemes

Kähne Bernhard (1), Clemens Markus (1), Schöps Sebastian (2)

(1) Chair of Electromagnetic Theory, University of Wuppertal, Wuppental, Germany
(2) Graduate School of Excellence Computational Engineering, Technische Universitat Darmstadt, Darmstadt, Germany

Purpose:

A transient magneto-quasistatic vector potential formulation involving nonlinear material is spatially discretized using the finite element method of first and second polynomial order. By applying a generalized Schur complement the resulting system of differential algebraic equations is reformulated into a system of ordinary differential equations (ODE). The ODE system is integrated in time by using explicit time integration schemes. The purpose of this paper is to investigate explicit time integration for eddy current problems with respect to the performance of the first-order explicit Euler scheme and the Runge-Kutta-Chebyshev (RKC) method of higher order.

Design/methodology/approach:

The ODE system is integrated in time using the explicit Euler scheme, which is conditionally stable by a maximum time step size. To overcome this limit, an explicit multistage RKC time integration method of higher order is used to enlarge the maximum stable time step size. Both time integration methods are compared regarding the overall computational effort.

Findings:

The numerical simulations show that a finer spatial discretization forces smaller time step sizes. In comparison to the explicit Euler time integration scheme, the multistage RKC method provides larger stable time step sizes to diminish the overall computation time.

Originality/value:

The explicit time integration of the Schur complement vector potential formulation of eddy current problems is accelerated by a multistage RKC method.

Keywords:

Eddy currents, Finite element method

Published in COMPEL - The international journal for computation and mathematics in electrical and electronic engineering, Vol. 41 No. 3, 2022, ISSN 0332-1649, page 915 - 924

Correlating structural complexity and acoustic noise performance of electric motors

Ibrahim Issah, Mohammadi Hossain Mohammad, Ghorbanian Vahid, Lowther David

Department of Electrical and Computer Engineering, McGill University, Montreal, Canada

Purpose:

Acoustic noise is a crucial performance index in the design of electrical machines. Due to the challenges associated with modelling a complete motor, the stator is often used to estimate the sound power in the prototyping stage. While this approach greatly reduces lengthy simulations, the actual sound power of the motor may not be known. But, from the acoustic noise standpoint, not much is known about the correlation between the stator and complete motor. This paper, therefore, aims to use the sound pressure levels of the stator and the full motor to investigate the existence of correlations in the interior permanent magnet synchronous motor.

Design/methodology/approach:

A multiphysics simulation framework is proposed to evaluate the sound pressure levels of multiple motor geometries in a given design space. Then, a statistical analysis is performed on the calculated sound pressure levels of each geometry over a selected speed range to compare the correlation strength between the stator and the full model.

Findings:

It was established that the stator and the complete motor model are moderately correlated. As such, a reliance on the stator sound power for design and optimization routines could yield inaccurate results.

Originality/value:

The main contribution involves the use of statistical tools to study the relationship between sound pressure levels associated with the stator geometry and the complete electric motor by increasing the motor sample size to capture subtle acoustic correlation trends in the design space of the interior permanent magnet synchronous motor.

Keywords:

Acoustic noise, Electric motor, Spearman's coefficient, Electrical machine, Finite element analysis, Multiphysics

Published in COMPEL - The international journal for computation and mathematics in electrical and electronic engineering, Vol. 41 No. 3, 2022, ISSN 0332-1649, page 925 - 937

Computational Electromagnetics in Education: A Technique for Calculation and Design of Induction Cooker Inductors

Michael G. Pantelyat and Yevgen I. Bajda
Department for Electrical Apparatus, National Technical University "Kharkiv Polytechnic Institute",
Kyrpychova Str. 2, UA-61002 Kharkiv, Ukraine
E-mail: m150462@yahoo.com, baida.kpi@gmail.com

***Abstract*—A technique for calculation and design of an inductor - the main structural element of an induction cooker is proposed. The technique consists of two stages: the first one has been developed on the basis of engineering methods for calculating inductors of industrial induction heaters, taking into account the design features and operating modes of induction cookers, and the second one represents the Finite Element Analysis of electromagnetic and thermal fields of household induction cookers. The calculation results and designs of the inductors with respect to a number of modes of heating of dishes of various geometric sizes are presented and analyzed.**

***Index Terms*—design, Finite Element Method, household induction cooker, inductor.**

I. INTRODUCTION

Induction cookers represent a relatively new class of modern electrical household appliances – electrical kitchen stoves which heat metal dishes by eddy currents generated by electromagnetic field with frequency of 20-100 kHz. The main structural part of the induction cooker is inductor – a one-turn or multi-turn coil, the alternating current flow in which generates an electromagnetic field which in its turn induces eddy currents in heated dishes with meal. The typical designs of one-ring and two-ring induction cookers as well as their inductor are presented in Fig. 1 [1].

Of considerable interest is the investigation of electromagnetic and thermal processes that occur in induction cookers during their operation, as well as the development of a technique for calculation and design of their structural elements. The developed technique and the results obtained should be intended for use in the practice of design of household induction cookers, as well as in the educational process for the training of students in the relevant field of study.

The Department for Electrical Apparatus, National Technical University "Kharkiv Polytechnic Institute", Kharkiv, Ukraine [2] is the only Department in Ukraine and, probably, in Europe which trains Bachelor and Master students in the field of study "Electrical Household Appliance". Graduates of the Department are Electrical Engineers working in the area of investigation, analysis, design and operation of various household devices for heating, conditioning, cooking, etc.

Figure 1: Design of induction cookers and their inductor.

In this paper, a technique for calculation and design of inductors of household induction cookers is proposed. The technique consists of two stages: the first one has been developed on the basis of engineering methods for calculating inductors of industrial induction heaters [3], taking into account the design features and operating modes of induction cookers, and the second one represents the Finite Element Analysis of electromagnetic and thermal fields of household induction cookers.

To increase professional skill of its graduates the Department intensifies teaching in the fields of Fundamentals and Theory in Electrical Engineering, Electromagnetic Theory and Computational Electromagnetics. Students are directly involved in investigations presented in this paper. In particular, the Department widely uses Comsol Multiphysics commercial code [4], open code FEMM [5] as well as in cooperation with the Institute for Fundamentals and Theory in Electrical Engineering (IGTE) TU Graz the EleFAnT2D computer code [6] developed at the IGTE, to build a relatively simple finite element models and simulate electromagnetic and thermal field distributions of induction cookers as examples of modern electrical household appliances. This helps students to understand principles of computational electromagnetics and make initial steps in practical numerical analysis.

Below both stages of the developed technique of calculation and design of inductors of induction cookers are described, the results obtained are analyzed in relation to the educational process of the training of students in the field of study "Electrical Household Appliance".

II. CALCULATION AND DESIGN OF INDUCTORS OF HOUSEHOLD INDUCTION COOKERS

A. A Calculation Technique

Initial data for engineering calculations and design are:

- geometry (diameter of the bottom, wall thickness) of the heated dishes (pans, pots);
- temperature-dependent electrophysical properties of the material of the dishes;

- electromagnetic field frequency and inductor voltage;
- power released in heated dishes and heating temperature.

Following [3] the main steps of the calculation and design of induction cookers' inductors are:

- selection of the main structural parameters of the inductor (outer and inner diameters of the inductor, the gap between the inductor and the dishes, the thickness of the inductor);
- calculation of electrical and energy indicators (specific surface power in the dishes, magnetic field strength on the surface of the inductor and dishes, coupling coefficient, active and reactive power in the inductor and in the gap, total power of the inductor-dishes system, electrical efficiency, power factor, current in the inductor, fill factor, etc.);
- determination of the number of turns of the inductor and calculation of the width of the turn

Consider briefly the main stages of the calculation. The sketch of the "inductor-dishes" system is shown in Fig. 2.

1) The geometrical dimensions of the inductor are selected (see Fig. 2). The outer diameter of the inductor d_{12} is taken equal to the diameter of the heated surface, i.e. the diameter of the bottom of the dishes d_2:

$$d_{12} \approx d_2.$$

The inner diameter of the inductor d_{11} is selected by the relationship

$$d_{11} \approx (2-4)\delta,$$

where δ denotes the gap between the inductor and the heated dishes, which, as in the design of inductors of industrial induction heating devices, is assumed to be minimal, based on the presence of thermal and electrical insulation and taking into account technological requirements. For household induction cookers, it is fashionable to take, for example, δ= 0.01 m.

The inductor thickness δ_1 is selected from the condition for minimizing losses [3]

$$\delta_1 \geq 1.3\Delta_1,$$

where Δ_1 denotes the penetration depth of the electromagnetic field (skin layer thickness) into the inductor material (nonmagnetic copper), calculated by the well-known formula [3].

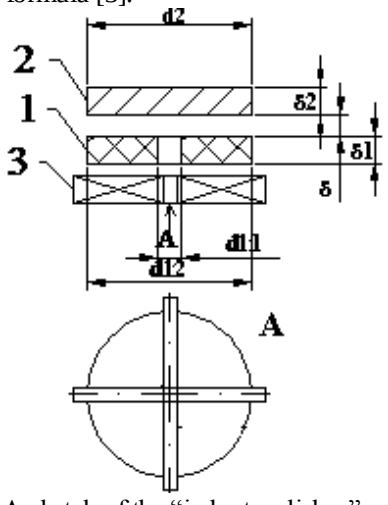

Figure 2: A sketch of the "inductor-dishes" system: 1 – inductor; 2 – heated dishes; 3 – ferrite core.

2) The main electrical and energy indicators of the inductor and the system "inductor-dishes" are calculated. The specific surface power in the dishes p_{02} is determined by the formula:

$$p_{02} = \frac{4P_2}{\pi(d_{12}^2 - d_{11}^2)},$$

where P_2 denotes the given in initial data power released in heated dishes.

The magnetic field strength H_{02} on the surface of the heated dishes is calculated by the formula [3]

$$H_{02} = \sqrt{\frac{p_{02} \cdot 10^3}{\rho_2 \mu_2 f F_\Phi}},$$

where ρ_2 denotes the electrical resistivity of the steel of the dishes at the given maximum temperature of its heating T_2, μ_2 the calculated value of the magnetic permeability of the dishes' steel at the given temperature T_2 (determined, for example, by the formulas and graphs presented in [3]), F_Φ the correction factor, the value of which is determined by the graphs presented in [3].

Then, the coupling coefficient k_{12} is determined, which in fact represents the transformation coefficient under the assumption that the inductor and heated dishes are windings of an air transformer [3]. The calculation of the coupling coefficient is performed using the corresponding expression given in [3].

The magnetic field strength on the surface of the inductor H_{01} is determined by the expression

$$H_{01} = \frac{H_{02}}{k_{12}}.$$

Then, the active power in the inductor P_1 is calculated:

$$P_1 = \pi \cdot H_{01}^2 \frac{d_{12}^2 - d_{11}^2}{4} \sqrt{\rho_1 f} F_1 \frac{1}{k_f},$$

where ρ_1 denotes the electrical resistivity of the material of the inductor (copper), k_f the fill factor of the inductor, taking into account the presence of interturn insulation which is preselected (usually k_f = 0.85-0.95 [3]), F_1 the correction factor, the value of which is determined by the graphs presented in [3].

Reactive powers in the inductor P_{Q1}, in the dishes P_{Q2} and in the gap P_{Q3} are determined by the formulas [3]:

$$P_{Q1} = P_1 \frac{G_1}{F_1};$$

$$P_{Q2} = 0.6 P_2 \frac{G_\Phi}{F_\Phi},$$

where G_1, G_Φ, F_1, F_Φ denote correction factors, the values of which are determined by the graphs presented in [3];

$$P_{Q3} = \pi \cdot H_{01}^2 f \delta d_{12}^2.$$

Then, the active P_Σ and reactive $P_{Q\Sigma}$ powers of the «inductor-dishes" system as the sum of the corresponding powers as well as the total power of the system $P_{S\Sigma}$ are determined:

$$P_{S\Sigma} = \sqrt{P_\Sigma^2 + P_{Q\Sigma}^2}.$$

Then the calculation of the electrical efficiency η and

power factor cosφ is carried out:

$$\eta = \frac{P_2}{P_\Sigma}; \qquad \cos\varphi = \frac{P_\Sigma}{P_{S\Sigma}}.$$

The calculation of the current in the inductor I_1 is performed by the formula:

$$I_1 = \frac{P_{S\Sigma}}{U_1},$$

where U_1 denotes the given voltage on the inductor.

3) The determination of the number of turns of the inductor and the calculation of the width of the turn are carried out. The number of turns of the inductor w_1 is calculated by the formula [3]

$$w_1 = \frac{H_{01} \cdot 0.5(d_{12} - d_{11})}{\sqrt{2} I_1},$$

and the width of the coil with insulation b_1 is determined as:

$$b_1 = \frac{d_{12} - d_{11}}{2w_1}.$$

B. *Initial Data for Calculations*

In this work, the inductors of induction cookers for two variants of the initial data presented in Table I are calculated and designed. It is assumed that the dishes heated is a pan made of Steel 45 grade [3].

The calculations are carried out for large and small diameter pans (24 cm and 12 cm, respectively) for the minimum (20 kHz) and maximum (100 kHz) frequencies of the electromagnetic field, used in modern induction cookers [1]. According to the technical characteristics of induction cookers, the power released in the dishes (2.0 kW and 3.3 kW), as well as the temperature of heating the dishes (100 °C and 280 °C), also vary. Thus, in this paper, two inductors (of large and small diameters for heating of the corresponding dishes) are calculated and designed for use either in the corresponding single-ring induction cookers, or in one double-ring cooker with rings of different diameters.

TABLE I
INITIAL DATA FOR INDUCTOR CALCULATION AND DESIGN

Option number	1	2
Diameter of the bottom of the dishes d_2, m	0.12	0.24
Wall thickness of the dishes δ_2, m	0.003	0.004
Electrical resistivity of steel of dishes at 20 ^{0}C ρ, Ω·m	$18.9 \cdot 10^{-8}$	$18.9 \cdot 10^{-8}$
Dishes heating temperature T_2, ^{0}C	100	280
Electrical resistivity of steel of dishes at given temperature T_2 for heating dishes ρ_2, Ω·m	$23.8 \cdot 10^{-8}$	$38.16 \cdot 10^{-8}$
Frequency of the electromagnetic field f, kHz	100	20
Inductor voltage U_1, V	220	220
Power released in the dishes P_2, W	2000	3300

C. *Results of Calculations and their Analysis*

The results of the calculation of inductors for both variants of the initial data are presented in Table II. We analyze briefly the results obtained.

The basic geometric dimensions of the "inductor-dishes" system are calculated (see Fig. 2). The outer diameter of the inductor is taken equal to the diameter of the heated surface (diameter of the pan). The gap between the inductor and the dishes is tentatively assumed to be 10 cm (0.01 m) and will be specified in the design process of the induction cooker, based on the presence of thermal and electrical insulation, taking into account the features of the technological process of assembling the cooker. Given in Table II the values of the inductor

TABLE II
RESULTS OF INDUCTOR CALCULATION

Option number	1	2
Outer diameter of the inductor d_{12}, m	0.12	0.24
Inner diameter of the inductor d_{11}, m	0.04	0.04
Gap between the inductor and the dishes δ, m	0.01	0.01
Inductor thickness δ_1, m	$0.29 \cdot 10^{-3}$	$0.5 \cdot 10^{-3}$
Specific surface power in the dishes p_{02}, W/m^2	$1.99 \cdot 10^5$	$7.5 \cdot 10^4$
Magnetic field strength on the surface of the dishes H_{02}, A/m	$1.55 \cdot 10^4$	$0.99 \cdot 10^4$
Magnetic field strength on the surface of the inductor H_{01}, A/m	$6.596 \cdot 10^4$	$4.213 \cdot 10^4$
Coupling coefficient k_{12}	0.235	0.253
Active power in inductor P_1, W	$2.058 \cdot 10^3$	$1.49 \cdot 10^3$
Reactive power in the inductor P_{Q1}, VAr	$2.058 \cdot 10^3$	$1.49 \cdot 10^3$
Reactive power in the dishes P_{Q2}, VAr	$1.2 \cdot 10^3$	$1.98 \cdot 10^3$
Reactive power in the gap P_{Q3}, VAr	$0.098 \cdot 10^3$	$0.161 \cdot 10^3$
Active power of the "inductor-dishes" system P_Σ, W	$4.058 \cdot 10^3$	$4.79 \cdot 10^3$
Reactive power of the "inductor-dishes" system $P_{Q\Sigma}$, VAr	$3.258 \cdot 10^3$	$3.47 \cdot 10^3$
Total power of the "inductor-dishes" system $P_{S\Sigma}$, VA	$5.204 \cdot 10^3$	$5.915 \cdot 10^3$
Electrical efficiency η	0.493	0.689
Power factor cosφ	0.78	0.81
Inductor current I_1, A	23.655	26.886
Number of turns of the inductor w_1	2	12
Width of coil with insulation b_1, m	0.02	0.0083

thickness calculated for both variants of the initial data are the minimum values that will also be refined during the designing the inductor. Among the calculated electric and energy quantities, the electric efficiency of the induction cooker is of most interest. The calculated values of the efficiency (about 50-70%, see Table II) are in good agreement with the results of experiments performed for one of household induction cookers [7] (59-70% depending on the selected mode of heating of the pot with water). We also note that the measured values of the power factor [7] are in the range of 0.98-1.00, in contrast to the calculation results (about 0.80, see table II). This may be because the reactive power compensator is probably used in the structure of the induction cooker.

The designs of a 2-turn and a 12-turn inductor calculated (the initial data and the results obtained – see Tables I, II, options 1 and 2, respectively) are presented in Fig. 3. Figure 4 shows the main structural elements of an induction cooker with a two-turn inductor, calculated according to the method developed by the authors. The developed design of a single-ring cooker with a two-turn inductor is also shown in Fig. 4.

III. Household Induction Cooker Electromagnetic and Thermal Fields Computer Simulation

A. Problem Definition

To investigate operation modes of household devices under consideration (power, frequency and their temporal variation, duration of heating, etc.) it is necessary to consider multiphysics phenomena taking place during their operation. Generally, the computer simulation represents numerical solution of the nonlinear multiply coupled problem including electromagnetic and thermal fields. In our cases the electromagnetic field can be solved independently of the temperature distribution, i.e., without taking the dependence of electrical conductance and magnetic permeability on temperature into account. This simplification is acceptable practically without any negative influence on the results because of rather low temperature rise – till 240-280 ^{0}C (higher temperatures are unacceptable due to the possible mechanical deformations of dishes as well as loss of nutritional quality of meal).

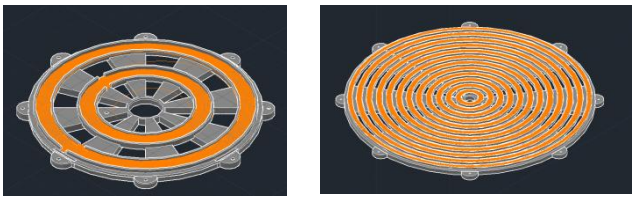

Figure 3: Designs of induction cookers' 2-turn and 12-turn inductors.

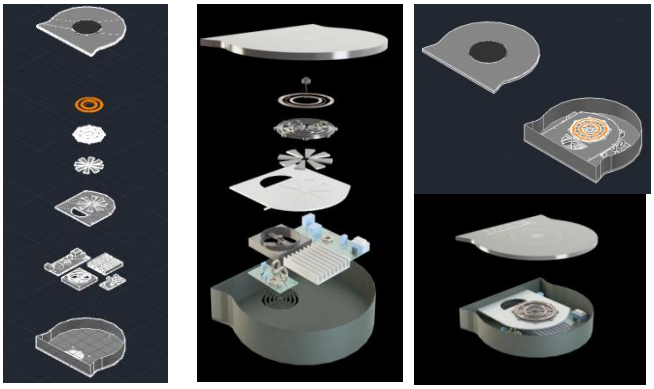

Figure 4: Conceptual design of an induction cooker with 2-turn inductor.

There are publications [8-11] devoted to induction cookers' electromagnetic and thermal fields computations using various formulations and approaches. In this paper the Authors do not intend to develop new or improve existing numerical techniques for induction cooker computer simulation. The goal of this section of the paper is to present international collaborative academic activities of the Department for Electrical Apparatus, National Technical University "Kharkiv Polytechnic Institute", Kharkiv, Ukraine and the Institute for Fundamentals and Theory in Electrical Engineering (IGTE) TU Graz, Austria to intensify Ukrainian students training in the field of Computational Electromagnetics using induction cookers as examples of devices under consideration. The paper describes examples of computational models developed by Ukrainian students using in-house computer code EleFAnT2D [6] during their stay at the IGTE under the guidance of their Austrian and Ukrainian tutors as well as obtained numerical results and their utilization to develop students' conceptual designs of induction cookers.

B. Simple Computation Models of Induction Cookers

To facilitate students' understanding of the basic principles of Computational Electromagnetics, the finite element analysis of induction cookers' electromagnetic and thermal fields is carried out in 2D formulation. Figures 5, 6 show examples of axisymmetrical computational models built using in-house computer code EleFAnT2D [6] developed at the IGTE. The first (the simplest) model includes (see Fig. 5) a copper two-turn inductor, a pan made from soft magnetic steel, a ferrite core, and dielectric subdomains. In Fig. 6 the improved model of the induction cooker is presented. We consider a modern pan designed specifically for induction cookers: an aluminum pan with a thin bottom ferromagnetic layer which is needed to obtain proper distributions of the electromagnetic field and eddy currents in the bottom of the pan. In addition, a ferrite magnetic core of the induction cooker is designed in such a way that can significantly improve its shielding capacity, thus reducing the scattering of electromagnetic field of the inductor in the surrounding area in order to increase the efficiency of the induction cooker. So, the second (more complicated) model includes (see Fig. 6) a copper three-turn inductor, heated dishes (an aluminum pan with a ferromagnetic layer), an improved ferrite core, and dielectric subdomains. The goal of students' investigations is to understand the influence of power, frequency, geometrical parameters of the models (see Fig. 5, 6), duration of heating, etc. on the electromagnetic and thermal field distributions.

C. A Mathematical Model and Results Obtained

The transient distribution of electromagnetic field is described by [12]:

$$\operatorname{curl}\left(\frac{1}{\mu}\operatorname{curl}\boldsymbol{A}\right)+\gamma\frac{\partial \boldsymbol{A}}{\partial t}=\boldsymbol{J}_{\text{ext}}, \tag{1}$$

where $\boldsymbol{A}$ denotes the magnetic vector potential, μ the magnetic permeability, γ the electric conductance and $\boldsymbol{J}_{\text{ext}}$ the harmonic current density applied to the inductor. Parameter γ is generally a function of the temperature T whereas μ is a function of the temperature T and magnetic flux density B. As said above, however, in case of a relatively small temperature rise, the temperature dependencies are disregarded.

The eddy currents produced in electrically conductive bodies given by the second term on the left–hand side in equation (1) give rise to the specific Joule losses w_J:

$$w_J=\gamma\left(\frac{\partial A}{\partial t}\right)^2 \tag{2}$$

whose value decreases roughly exponentially with the distance from the surface of the heated body.

In fact, the complete solution of the parabolic equation (1) is unfeasible due to relatively long time of the heating process. That is why we simplified the model by considering harmonic magnetic field. Now equation (1) can be rewritten in terms of the phasor $\underline{\boldsymbol{A}}$ of the magnetic vector potential $\boldsymbol{A}$ [12]:

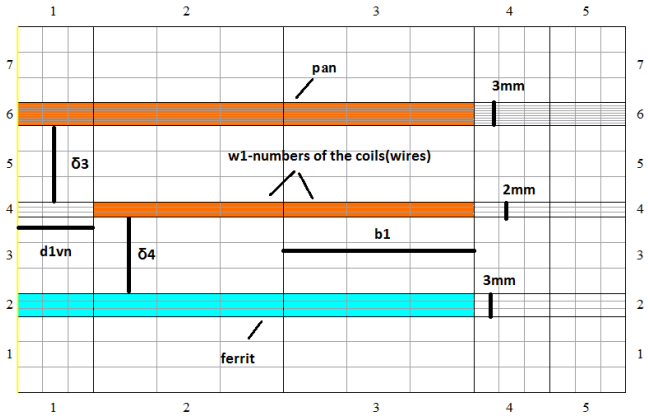

Figure 5: The first computational model of an induction cooker.

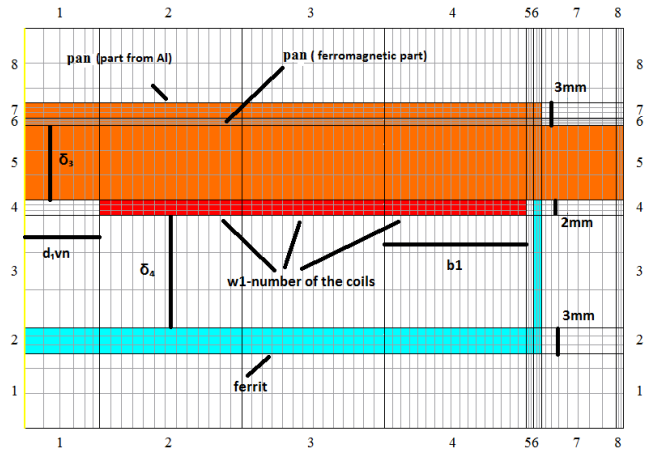

Figure 6: The second computational model of an induction cooker.

$$\operatorname{curl}\frac{1}{\mu}\operatorname{curl}\underline{\boldsymbol{A}}+j\omega\gamma\underline{\boldsymbol{A}}=\underline{\boldsymbol{J}}_{\text{ext}}. \tag{3}$$

The computations are carried out iteratively, and at each step the magnetic permeability μ in each element containing ferromagnetic material is adjusted in accordance with the main magnetization curve of soft magnetic material.

The specific Joule losses are then expressed as:

$$w_J=\gamma\omega^2\left|\underline{\boldsymbol{A}}\right|^2. \tag{4}$$

The temperature field is described by [13]:

$$\operatorname{div}(\lambda\operatorname{grad}T)=\rho c\frac{\partial T}{\partial t}-w_J, \tag{5}$$

where λ is the thermal conductivity, ρ the mass density and c the specific heat of the material. All these parameters are generally temperature–dependent functions. The boundary conditions are respected by convection while the thermal radiation is neglected because of the relatively low temperatures.

Equations (3), (5) are solved in the axisymmetrical formulation by the Finite Element Method using in-house computer code EleFAnT2D [6].

Examples of obtained by students distributions of electromagnetic and thermal fields are presented in Fig. 7, 8. Figure 7 shows magnetic flux density distribution in the model with geometrical parameters (see Fig. 6 – improved model of the induction cooker) $d_{1\text{vn}}$ = 10 mm, b_1 = 16 mm, δ_3 = 10 mm, δ_4 = 2 mm and frequency of current in the inductor of 20 kHz. In its turn, Fig. 8 shows steady-state temperature field distribution of the heated aluminum pan with thin ferromagnetic layer.

Numerical analysis carried out by students helps them to propose designs of various inductors of induction cookers as well as to develop in their Bachelor and Master Theses conceptual designs of induction cookers in whole. Illustrative examples are presented in Fig. 3, 4.

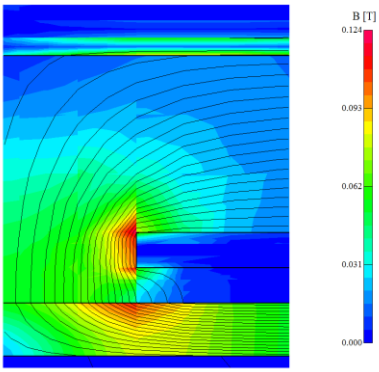

Figure 7: Electromagnetic field distribution.

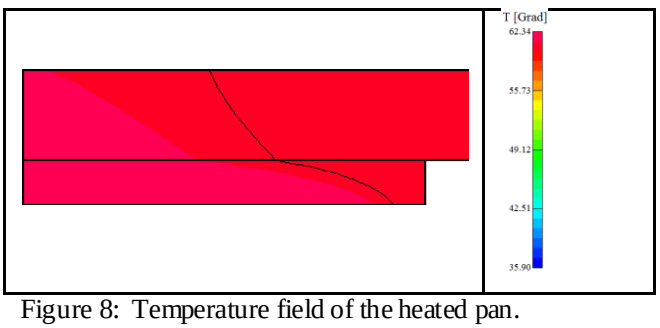

Figure 8: Temperature field of the heated pan.

IV. Conclusion

The Department for Electrical Apparatus, National Technical University "Kharkiv Polytechnic Institute", Kharkiv, Ukraine is the only Department in Ukraine and, probably, in Europe which trains Bachelor and Master students in the field of study "Electrical Household Appliance". Graduates of the Department are Electrical Engineers working in the area of investigation, analysis, design and operation of various household appliances including modern induction cookers.

In this paper, a developed technique for calculation and design of inductors of household induction cookers is described. The technique consists of two stages: the first one has been developed on the basis of engineering methods for calculating inductors of industrial induction heaters, taking into account the design features and operating modes of induction cookers, and the second one represents the Finite Element Analysis of electromagnetic and thermal fields of household induction cookers.

Inductors of induction cookers for various variants of the initial data are calculated and designed. The paper presents the conceptual designs of inductors and induction cookers developed by students.

The Department of Electrical Apparatus, National Technical University "Kharkiv Polytechnic Institute", Kharkiv, Ukraine uses widely various computer codes including EleFAnT2D developed at the IGTE to intensify teaching in the field of Computational Electromagnetics. The finite element analysis of electromagnetic and thermal fields distributions of modern electrical household appliances – induction cookers is carried out. Training computational models of induction cookers are developed and investigated by Ukrainian students under the guidance of their Austrian and Ukrainian tutors. Obtained numerical results and their analysis are used during preparation of Bachelor and Master Theses.

V. Acknowledgment

The authors acknowledge the Institute for Fundamentals and Theory in Electrical Engineering (IGTE) TU Graz, Austria (Prof. Oszkár Bíró, Prof. Thomas Bauernfeind) for providing EleFAnT2D code and giving support in the modelling, simulation and post processing.

References

[1] M.G. Pantelyat, O. Bíró, and Th. Bauernfeind, "Computational electromagnetics in education: finite element analysis of induction cookers' electromagnetic and thermal fields," *Abstracts of the 17th Int. IGTE Symp. on Numerical Field Calculation in Electrical Engineering*, 18-21 Sept. 2016, Graz, Austria, p. 20.

[2] http://web.kpi.kharkov.ua/ea/about-the-department/

[3] A.B. Kuvaldin, *Induction Heating of Ferromagnetic Steel*, Moscow: Energoatomizdat, 1988 (in Russian).

[4] https://doc.comsol.com

[5] http://www.femm.info

[6] http://www.igte.tugraz.at/de/elefant/elefant.html

[7] O.O. Chepeliuk, M.G. Pantelyat, Yu.S. Hryshchuk and A.K. Yeloiev, "An experimental stand for induction cookers investigations", *Journal of the Kharkiv National Technical University*, No. 2, pp. 23-28, 2019 (in Ukrainian).

[8] C. Carretero, O. Lucia, J. Acero, J.M. Bordio, and R. Alonso, "Passive network equivalent of an induction system for domestic cookers application based on FEA tool simulation," *Proc. 26th Annual IEEE Applied Power Electronics Conf. and Exposition (APEC)*, 6-11 March 2011, Fort Worth, Texas, USA, pp. 1753-1758, 2011.

[9] C. Carretero, O. Lucia, J. Acero, and J.M. Bordio, "Computational modeling of two partly coupled coils supplied by a double half-bridge resonant inverter for induction heating appliances," *IEEE Transactions on Industrial Electronics*, vol. 60, pp. 3092-3105, 2013.

[10] L.C. Meng, K.W.E. Cheng, and K.W. Chan, "Heating performance improvement and field study of the induction cooker," *Proc. of the 3rd Int. Conf. on Power Electronics Systems and Applications (PESA)*, 20-22 May 2009, Hong Kong, pp. 313-317, 2009.

[11] L.C. Meng, K.W.E. Cheng, and P.C.K. Luk, "Field analysis of an induction cooker with square 9-coil system by applying diverse exciting pattern," *Proc. 6th IET Int. Conf. on Power Electronics, Machines and Drives (PEMD 2012)*, 27-29 March 2012, Bristol, United Kingdom, pp. 1-5, 2012.

[12] M.V.K. Chari and S.J. Salon, *Numerical Methods in Electromagnetism*. New York: Academic, 2000.

[13] J.P. Holman, *Heat Transfer*. New York: McGraw-Hill, 2002.

Domain decomposition and upscaling technique for metascreens

Leumüller Michael, Hollaus Karl, Schöberl Joachim

Institute for Analysis and Scientific Computing, Technische Universität Wien, Vienna, Austria

Purpose:

This paper aims to consider a multiscale electromagnetic wave problem for a housing with a ventilation grill. Using the standard finite element method to discretise the apertures leads to an unduly large number of unknowns. An efficient approach to simulate the multiple scales is introduced. The aim is to significantly reduce the computational costs.

Design/methodology/approach:

A domain decomposition technique with upscaling is applied to cope with the different scales. The idea is to split the domain of computation into an exterior domain and multiple non-overlapping sub-domains. Each sub-domain represents a single aperture and uses the same finite element mesh. The identical mesh of the sub-domains is efficiently exploited by the hybrid discontinuous Galerkin method and a Schur complement which facilitates the transition from fine meshes in the sub-domains to a coarse mesh in the exterior domain. A coarse skeleton grid is used on the interface between the exterior domain and the individual sub-domains to avoid large dense blocks in the finite element discretisation matrix.

Findings:

Applying a Schur complement to the identical discretisation of the sub-domains leads to a method that scales very well with respect to the number of apertures.

Originality/value:

The error compared to the standard finite element method is negligible and the computational costs are significantly reduced.

Keywords:

Finite element method, Domain decomposition method, Metasurfaces

Published in COMPEL - The international journal for computation and mathematics in electrical and electronic engineering, Vol. 41 No. 3, 2022, ISSN 0332-1649, page 938 - 953

Maximum entropy snapshot sampling for reduced basis modelling

Bannenberg W.F.M. Marcus (1), Kasolis Fotios (3), Günther Michael (1), Clemens Markus (2)

(1) (IMACM, Bergische Universität Wuppertal, Chair of Applied Mathematics and Numerical Analysis (AMNA)
(2) IMACM, Bergische Universität Wuppertal, Chair of Electromagnetic Theory, Wuppertal, Germany
(3) STMicroelectronics, Catania, Italy

Purpose:

The maximum entropy snapshot sampling (MESS) method aims to reduce the computational cost required for obtaining the reduced basis for the purpose of model reduction. Hence, it can significantly reduce the original system dimension whilst maintaining an adequate level of accuracy. The purpose of this paper is to show how these beneficial results are obtained.

Design/methodology/approach:

The so-called MESS method is used for reducing two nonlinear circuit models. The MESS directly reduces the number of snapshots by recursively identifying and selecting the snapshots that strictly increase an estimate of the correlation entropy of the considered systems. Reduced bases are then obtained with the orthogonal-triangular decomposition.

Findings:

Two case studies have been used for validating the reduction performance of the MESS. These numerical experiments verify the performance of the advocated approach, in terms of computational costs and accuracy, relative to gappy proper orthogonal decomposition.

Originality/value:

The novel MESS has been successfully used for reducing two nonlinear circuits: in particular, a diode chain model and a thermal-electric coupled system. In both cases, the MESS removed unnecessary data, and hence, it reduced the snapshot matrix, before calling the QR basis generation routine. As a result, the QR-decomposition has been called on a reduced snapshot matrix, and the offline stage has been significantly scaled down, in terms of central processing unit time.

Keywords:

Reduced-order method, Circuit analysis, Model order reduction, Numerical linear algebra

Published in COMPEL - The international journal for computation and mathematics in electrical and electronic engineering, Vol. 41 No. 3, 2022, ISSN 0332-1649, page 954 - 966

Model order reduction of nonlinear eddy-current field using parameterized CLN

Tobita Miwa, Eskandari Hamed, Matsuo Tetsuji

Graduate School of Engineering, Kyoto University, Kyoto, Japan

Purpose:

The authors derive a nonlinear MOR based on the Cauer ladder network (CLN) representation, which serves as an application of the parameterized MOR. Two parametrized CLN representations were developed to handle the nonlinear magnetic field. Simulations using the parameterized CLN were also conducted using an iron-cored inductor model under the first-order approximation.

Design/methodology/approach:

This work studies the effect of parameter variations on reduced systems and aims at developing a general formulation for parametrized model order reduction (MOR) methods with the dynamical transition of parameterized state.

Findings:

Terms including time derivatives of basis vectors appear in nonlinear state equations, in addition to the linear network equations of the CLN method. The terms are newly derived by an exact formulation of the parameterized CLN and are named parameter variation terms in this study. According to the simulation results, the parameter variation terms play a significant role in the nonlinear state equations when reluctivity is used, while they can be neglected when differential reluctivity is used.

Originality/value:

The authors introduced a general representation for the dynamical behavior of the reduced system with time-varying parameters, which has not been theoretically discussed in previous studies. The effect of the parameter variations is numerically given as a form of parameter variation terms by the exact derivation of the nonlinear state equations. The influence of parameter variation terms was confirmed by simulation.

Keywords:

Model order reduction, Eddy currents, Magnetic saturation

Published in COMPEL - The international journal for computation and mathematics in electrical and electronic engineering, Vol. 41 No. 3, 2022, ISSN 0332-1649, page 967 - 980

Computation of rotational hysteresis losses by vector Preisach models based on rotational operators

Nierla Michael (1), Kaltenbacher Manfred (2), Rupitsch Johann Stefan (3)

(1) Department of Electrical, Electronic and Communication Engineering, Friedrich-Alexander-University Erlangen-Nuremberg, Erlangen, Germany
(2) Institute of Fundamentals and Theory in Electrical Engineering, TU Graz, Graz, Austria
(3) Mikrosystems Engineering, Technical Department Albert-Ludwigs-University Freiburg, Freiburg, Germany

Purpose:

A major purpose of vector hysteresis models lies in the prediction of power losses under rotating magnetic fields. The well-known vector Preisach model by Mayergoyz has been shown to well predict such power losses at low amplitudes of the applied field. However, in its original form, it fails to predict the reduction of rotational power losses at high fields. In recent years, two variants of a novel vector Preisach model based on rotational operators have been published and investigated with respect to general accuracy and performance. This paper aims to examine the capabilities of the named vector Preisach models in terms of rotational hysteresis loss calculations.

Design/methodology/approach:

In a first step, both variants of the novel rotational operator-based vector Preisach model are tested with respect to their overall capability to prescribe rotational hysteresis losses. Hereby, the direct influence of the model-specific parameters onto the computable losses is investigated. Afterward, it is researched whether there exists an optimized set of parameters for these models that allows the matching of measured rotational hysteresis losses.

Findings:

The theoretical investigations on the influence of the model-specific parameters onto the computable rotational hysteresis losses showed that such losses can be predicted in general and that a variation of these parameters allows to adapt the simulated loss curves in both shape and amplitude. Furthermore, an optimized parameter set for the prediction of the named losses could be retrieved by direct matching of simulated and measured loss curves.

Originality/value:

Even though the practical applicability and the efficiency of the novel vector Preisach model based on rotational operators has been proven in previous publications, its capabilities to predict rotational hysteresis losses has not been researched so far. This publication does not only show the general possibility to compute such losses with help of the named vector Preisach models but also in addition provides a routine to derive an optimized parameter set, which allows an accurate modeling of actually measured loss curves.

Keywords:

Hysteresis modeling, Vector Preisach model, Rotational hysteresis losses, Computational electromagnetics, Power losses, Magnetic hysteresis

Published in COMPEL - The international journal for computation and mathematics in electrical and electronic engineering, Vol. 41 No. 3, 2022, ISSN 0332-1649, page 981 - 995

Investigation of electromagnetic wave propagation in the bicomplex 3D-FEM using a wavenumber Whitney Hodge operator

Reum Thomas, Toepfer Hannes

Advanced Electromagnetics Group, Faculty of Electrical Engineering and Information Technology, Technische Universität Ilmenau, Ilmenau, Germany

Purpose:

The purpose of this paper is to show the applicability of a discrete Hodge operator in the context of the De Rham cohomology to bicomplex-valued electromagnetic wave propagation problems. It was applied in the finite element method (FEM) to get a higher accuracy through conformal discretization. Therewith, merely the primal mesh is needed to discretize the full system of Maxwell equations.

Design/methodology/approach:

At the beginning, the theoretical background is presented. The bicomplex number system is used as a geometrical algebra to describe three-dimensional electromagnetic problems. Because we treat rotational field problems, Whitney edge elements are chosen in the FEM to realize a conformal discretization. Next, numerical simulations regarding practical wave propagation problems are performed and compared with the common FEM approach using the Helmholtz equation.

Findings:

Different field problems of three-dimensional electromagnetic wave propagation are treated to present the merits and shortcomings of the method, which calculates the electric and magnetic field at the same spatial location on a primal mesh. A significant improvement in accuracy is achieved, whereas fewer essential boundary conditions are necessary. Furthermore, no numerical dispersion is observed.

Originality/value:

A novel Hodge operator, which acts on bicomplex-valued cotangential spaces, is constructed and discretized as an edge-based finite element matrix. The interpretation of the proposed geometrical algebra in the language of the De Rham cohomology leads to a more comprehensive viewpoint than the classical treatment in FEM. The presented paper may motivate researchers to interpret the form of number system as a degree of freedom when modeling physical effects. Several relationships between physical quantities might be inherently implemented in such an algebra.

Keywords:

Electromagnetic waves, Finite element method, Partial differential equations, Computational electromagnetics, Whitney forms, Discrete electromagnetism

Published in COMPEL - The international journal for computation and mathematics in electrical and electronic engineering, Vol. 41 No. 3, 2022, ISSN 0332-1649, page 996 - 1010

Fast and numerically stable Mie solution of EM near field and absorption for stratified spheres

Csernyava Olivér (1), Horváth Péter Bálint (1), Badics Zsolt (1) (2), Bilicz Sándor (1)

(1) Department of Broadband Infocommunications and Electromagnetic Theory, Budapest University of Technology and Economics, Budapest, Hungary
(2) Tensor Research LLC, Andover, Massachusetts, USA

Purpose:

he purpose of this paper is the development of an analytic computational model for electromagnetic (EM) wave scattering from spherical objects. The main application field is the modeling of electrically large objects, where the standard numerical techniques require huge computational resources. An example is full-wave modeling of the human head in the millimeter-wave regime. Hence, an approximate model or analytical approach is used.

Design/methodology/approach:

The Mie–Debye theorem is used for calculating the EM scattering from a layered dielectric sphere. The evaluation of the analytical expressions involved in the infinite sum has several numerical instabilities, which makes the precise calculation a challenge. The model is validated through an application example with comparing results to numerical calculations (finite element method). The human head model is used with the approximation of a two-layer sphere, where the brain tissues and the cranial bones are represented by homogeneous materials.

Findings:

A significant improvement is introduced for the stable calculation of the Mie coefficients of a core–shell stratified sphere illuminated by a linearly polarized EM plane wave. Using this technique, a semi-analytical expression is derived for the power loss in the sphere resulting in quick and accurate calculations.

Originality/value:

Two methods are introduced in this work with the main objective of estimating the final precision of the results. This is an important aspect for potentially unstable calculations, and the existing implementations have not included this feature so far.

Keywords:

Applied electromagnetism, Microwaves, Electromagnetic wave, Computational electromagnetics, Wave propagation, Mie, Multilayer, SAR, Sphere, Wave scatterings,

Published in COMPEL - The international journal for computation and mathematics in electrical and electronic engineering, Vol. 41 No. 3, 2022, ISSN 0332-1649, page 1011 - 1023

On the Modeling and Simulation of AC fields in High-Temperature Superconductors

W. R. Tonnon*, and J. Smajic*

* Institute of Electromagnetic Fields, ETH Zürich, 8092 Zürich, Switzerland
E-mail: wtonnon@ethz.ch

***Abstract*—In this work, we develop a complete numerical scheme for the computation of the losses in high-temperature superconductors based on earlier work by Brambilla et al. The original scientific contribution of this paper is the use of the relaxed-fixed-point iteration for finding fixed-points. In the one-dimensional case, we prove that this method is guaranteed to converge for functions with continuous derivative. Numerical experiments suggest that these convergence results carry over to the higher-dimensional case. It is shown that the relaxed-fixed-point iteration greatly outperforms Jacobian-based solvers for the non-linear system that occurs when modeling high-temperature superconductors.**

***Index Terms*—Superconductors, FEM, Non-Linear**

I. Introduction

High-temperature superconductors play an increasingly important rule in modern engineering with applications ranging from magnetic resonance imaging to power engineering [1]. In the latter application, it is important to be able to estimate the losses during operation. Analytical results for the losses in superconductors with simple geometries are available [2]. However, practical superconductors often do not adhere to these simple geometries. Therefore, it is necessary to develop numerical schemes that are able to predict the losses in superconductors with complicated geometries.

Already in 1962, Bean proposed a very simple model to describe the current distribution in a superconductor wire [4][5]. In 1993, Rhyner introduced the idea that a superconductor can be described by a non-linear relation between the resistivity and current density [6]. Based on the idea of Rhyner, Brambilla et al. developed a 2D numerical scheme to estimate the AC losses in superconductors [3]. The formulation leads to a system of non-linear equations. However, a discussion on stability and performance of non-linear solvers for this system is not available.

In this paper, we propose the use of the relaxed-fixed-point iteration as non-linear solver for the given problem. We show that for any $f \in C^1(\mathbb{R};\mathbb{R})$ with at least one fixed-point, suitable parameters can be chosen such that convergence of the relaxed-fixed-point-iteration is guaranteed. We provide experimental verification that suggests that this result can be extended to more general functions $f \in C^1(\mathbb{R}^N;\mathbb{R}^N)$ with $N > 1$. Using the relaxed-fixed-point iteration, we are able to compute current distributions in a circular superconductor. By comparison with analytical results for the losses in high-temperature superconductors [2], we validate our results.

This paper is constructed as follows. In section II, we explain how we arrive at the system of non-linear equations. Also, we introduce the relaxed-fixed-point iteration, and provide a rigorous convergence result for the case $N = 1$. Then, in section III we show experimental convergence results for the case $N > 1$, and we discuss the performance of the solver. Finally, we conclude our work in section IV.

II. Methods

A. Formal Description of the Problem

The behaviour of a high-temperature superconductor can be encapsulated in an empirical non-linear relationship between the resistivity and the current density [3] [6] [7] of the form

$$\rho(\mathbf{J}) = \frac{E_c}{J_c}\left|\frac{\mathbf{J}}{J_c}\right|^{n-1}, \tag{1}$$

where ρ is the local resistivity, $\mathbf{J}$ is the local current density, E_c is the amplitude of the electric field under the critical current density, J_c is the critical current density, and n is a material-dependent integer with a value between 10-30.

Since we are interested in high-power applications, it is reasonable to neglect the displacement current. Therefore, we can reduce Maxwell's equations to the following system [8]

$$\begin{cases} \nabla \times \Big(\rho(\nabla \times \mathbf{H})\ \nabla \times \mathbf{H}\Big) = -\mu\frac{\partial \mathbf{H}}{\partial t}, \\ \nabla \cdot \mathbf{H} = 0, \\ \mathbf{n} \times \mathbf{H} = \mathbf{g}, \end{cases} \tag{2}$$

where $\mathbf{H}$ indicates the magnetic field, and μ is the magnetic permeability. We also enforced Dirichlet boundary conditions, that is, we enforced the tangential magnetic field to be equal to some known $\mathbf{g}$ (possibly space- and time-dependent). Note that the resistivity ρ occuring in equation 2 depends non-linearly on the current density $\mathbf{J} = \nabla \times \mathbf{H}$ by equation 1. In this work, we will only consider two-dimensional domains.

B. Weak Formulation

Following [10], we use as test space the Sobolev space $H_0(\text{curl};\Omega)$, which is defined as

$$\begin{aligned} H_0(\text{curl};\Omega) = \{\boldsymbol{\psi} \in &\mathrm{L}^2(\Omega) : \nabla \times \boldsymbol{\psi} \in \mathrm{L}^2(\Omega) \\ &\text{and } \mathbf{n} \times \boldsymbol{\psi} = \mathbf{0} \text{ on } \partial\Omega\}, \end{aligned} \tag{3}$$

equipped with the norm

$$\|\boldsymbol{\psi}\|_{H(\text{curl};\Omega)} = \|\nabla \times \boldsymbol{\psi}\|_{L^2(\Omega)} + \|\boldsymbol{\psi}\|_{L^2(\Omega)}. \quad (4)$$

Note that $H_0(\text{curl};\Omega)$ is a Hilbert space under the topology induced by the given norm [11]. Let us define $H_D(\text{curl};\Omega)$ as

$$H_D(\text{curl};\Omega) = \{\boldsymbol{\psi} \in \mathrm{L}^2(\Omega) : \nabla \times \boldsymbol{\psi} \in \mathrm{L}^2(\Omega) \text{ and } \mathbf{n} \times \boldsymbol{\psi} = \mathbf{D} \text{ on } \partial\Omega\}. \quad (5)$$

The total problem can be formulated as follows. We search $\mathbf{H} : [0,T] \to H_D(\text{curl};\Omega)$ such that $\forall \boldsymbol{\psi} \in H_0(\text{curl};\Omega)$ holds that

$$\int_\Omega (\partial_t(\mu\mathbf{H}) \cdot \boldsymbol{\psi} dx + \int_\Omega \rho(\nabla \times \mathbf{H}) \nabla \times \mathbf{H} \cdot \nabla \times \boldsymbol{\psi} dx = 0. \quad (6)$$

For the finite-element discretization of our system, we use Nédélec elements, also known as Whitney or edge elements. The benefit of using these elements is that they are locally divergence free, and the continuity condition for tangential magnetic fields is automatically satisfied between elements [9]. If we assume sufficient regularity of the solution, we can expect h-convergence of first order [10].

C. Time Discretization

After finite-element discretization as described in section II-B, we obtain the following method-of-lines ordinary differential equation

$$\begin{bmatrix}[A_{11}] & [A_{12}] \\ [0] & [0]\end{bmatrix} [\dot{\tilde{u}}] + \begin{bmatrix}[B_{11}([\tilde{u}])] & [B_{12}([\tilde{u}])] \\ [0] & [\tilde{I}]\end{bmatrix} [\tilde{u}] = \begin{bmatrix}[0] \\ [D]\end{bmatrix}, \quad (7)$$

where $[A_{1i}]$ and $[B_{1i}]$ respectively corresponds to the first and second integral in equation 6, $[\tilde{u}]$ is the discretized representation of the solution $\mathbf{H}$ of equation 6, $[D]$ is a vector with the tangential components of the Dirichlet boundary conditions, and $[\tilde{I}]$ is the identity matrix with some signs flipped depending on the orientation of the edges. Note that all the elements of $[\tilde{u}]$ corresponding to edge elements on the boundary, are all assumed to be in the last elements. Since these values are enforced by the Dirichlet boundary conditions, we can set

$$[\tilde{u}] = \begin{bmatrix}[u] \\ [\tilde{I}][D]\end{bmatrix}. \quad (8)$$

Using this representation for $[\tilde{u}]$, we can simplify equation 7 to

$$[A_{11}][\dot{u}] + [B_{11}([u])][u] = -[A_{12}][\tilde{I}][\dot{D}] - [B_{12}([u])][\tilde{I}][D]. \quad (9)$$

Using a second-order backward differentiation scheme, we obtain

$$[U_{n+2}] = \Big([I] + \frac{2}{3}dt[A_{11}]^{-1}[B_{11}([U_{n+2}])]\Big)^{-1} \Big(\frac{4}{3}[U_{n+1}] - \frac{1}{3}[U_n] - \frac{2}{3}dt[A_{11}]^{-1}[A_{12}][\tilde{I}][\dot{D}(t_{n+2})] - \frac{2}{3}dt[A_{11}]^{-1}[B_{12}([U_{n+2}])][\tilde{I}][D(t_{n+2})]\Big), \quad (10)$$

where t_n is the time after n time steps, $[U_n]$ is the approximation of $[u]$ at time t_n, and dt is the length of a single time step. We can expect second-order convergence if stability conditions are met [12].

D. Non-Linear Solver

The system in equation 10 needs to be solved for $[U_{n+2}]$. In fact, if we let $N \in \mathbb{N}$ indicate the length of $[U_{n+2}]$, then we can find an $f \in C^\infty(\mathbb{R}^N;\mathbb{R}^N)$ such that equation 10 is equivalent to

$$[U_{n+2}] = f([U_{n+2}]). \quad (11)$$

A first idea would be to use the traditional fixed-point iteration to solve this system. However, since the traditional fixed-point iteration requires f to be a contraction mapping [13], we have to increase the stability of the fixed-point iteration. With that goal in mind, we take the weighted average between the fixed-point iteration and the identity operator.

Definition 1. We call a sequence $(x_n)_{n\in\mathbb{N}} \subset \mathbb{R}$ an *α-relaxed-fixed-point iteration* with respect to some $f : \mathbb{R}^N \to \mathbb{R}^N$, if it satisfies

$$x_{k+1} = \alpha f(x_k) + (1-\alpha)x_k, \quad (12)$$

for $k \in \mathbb{N}$, $x_0, \alpha \in \mathbb{R}$.

Intuitively, as we bring α closer to zero we would expect the iteration to become more and more stable. However, to the knowledge of the authors, there is no literature available that confirms this intuition. In [13], a convergence requirement is derived which is equivalent to the requirement for the regular fixed-point iteration. However, we are interested in weaker convergence conditions. For the case $N = 1$, we can prove convergence under significantly weaker assumptions on f (see Theorem 5).

To do so, we will define two classes of functions, pseudo-contraction mappings and expansion mappings, and prove convergence results for functions in these classes. Then we will show that any function that satisfies the assumptions of Theorem 5 can be constructed from functions in these classes. Let $\Omega \subset\subset \mathbb{R}$ be connected and bounded. A pseudo-contraction mapping can be defined as

Definition 2. A function $f \in C^1(\Omega;\mathbb{R})$ is called a *pseudo-contraction mapping*, if there exists $x^* \in \Omega$, $C > 0$ such that

- $\forall x > x^* : f(x) < x$
- $\forall x < x^* : x < f(x)$

Remark 1. If f is a pseudo-contraction mapping, the point x^* in Definition 2 must be a unique fixed-point of f.

Lemma 1. *Let f be a pseudo-contraction mapping, then there exists a $C > 0$ such that*

- $\forall x > x^* : C(x^* - x) < f(x) - x^* < x - x^*$,
- $\forall x < x^* : x - x^* < f(x) - x^* < C(x^* - x)$,

and we say f is a C-pseudo-contraction mapping

Proof: Since Ω is bounded, this follows directly by the continuity of the derivative of f. ■

Lemma 2. *If f is a C-pseudo-contraction mapping, then, for α with $0 < \alpha < \frac{1}{1+C}$, its α-relaxed-fixed-point iteration converges for any initial value $x_0 \in \Omega$, and the limit is the unique fixed-point of f.*

Proof: First, we note that by Remark 1, f must have a unique fixed-point and this fixed-point corresponds to x^* as defined in Definition 2. Now let $x_0 \in \Omega \setminus \{x^*\}$ be arbitrary. We assume without loss of generality that $x_0 \neq x^*$. We are left with two cases, either $x_0 > x^*$ or $x_0 < x^*$.

First, let $x_0 > x^*$. We show by induction that for $k \in \mathbb{N}$, $x_k > x^*$. Assume that for some $k \in \mathbb{N}$, we have that $x_k > x^*$, then

$$\begin{aligned} x_{k+1} &= \alpha f(x_k) + (1-\alpha)x_k \\ &> \alpha[C(x^* - x_k) + x^*] + (1-\alpha)x_k \\ &= \alpha(C+1)x^* + [1 - \alpha(1+C)]x_k \\ &> \alpha(C+1)x^* + [1 - \alpha(1+C)]x^* \\ &= x^*, \end{aligned}$$

where we obtained the first inequality from Lemma 1, and the second inequality from our assumption on α ($\alpha < \frac{1}{C+1}$) and the assumption $x_k > x^*$. We can thus conclude that $\forall k \in \mathbb{N} : x_k > x^*$.

On the other hand, for $k \in \mathbb{N}$, we have by Lemma 1

$$\begin{aligned} x_{k+1} &= \alpha f(x_k) + (1-\alpha)x_k \\ &< \alpha x_k + (1-\alpha)x_k \\ &= x_k \end{aligned}$$

We conclude that the sequence $(x_k)_{k\in\mathbb{N}} \subset \Omega$ is strictly decreasing and has a lower bound. By the monotone convergence theorem, we find that $x := \lim_{k\to\infty} x_k$ exists. By the continuity of f, we find

$$\begin{aligned} x &= \lim_{k\to\infty} x_{k+1} \\ &= \lim_{k\to\infty} [\alpha f(x_k) + (1-\alpha)x_k] \\ &= \alpha f(x) + (1-\alpha)x \\ &\implies x = f(x). \end{aligned}$$

Since f has a unique fixed-point, we must have that $x^* = x$. The proof for the case $x_0 < x^*$ is analogous. ■

The second class of functions is the class of expansion mapping. We define an expansion mapping as

Definition 3. A function $f \in C^1(\Omega;\mathbb{R})$ is called an *expansion mapping*, if there exists $x^* \in \Omega$, $C > 0$ such that

- $\forall x > x^* : f(x) > x$
- $\forall x < x^* : x > f(x)$

Remark 2. If f is an expansion mapping, the point x^* in Definition 3 must be a unique fixed-point of f.

We obtain the following result for expansion mappings that is analogous to Lemma 1.

Lemma 3. *Let f be an expansion mapping, then there exists a $C > 0$ such that*

- $\forall x > x^* : x - x^* < f(x) - x^* < C(x - x^*)$
- $\forall x < x^* : C(x - x^*) < f(x) - x^* < x - x^*$,

and we say f is a C-expansion mapping

Proof: Analog to the proof of Lemma 1. ■

Now we are ready to prove an analogous result to Lemma 2 for expansion mappings.

Lemma 4. *If f is a C-expansion mapping, then, for α with $-\frac{1}{C-1} < \alpha < 0$, its α-relaxed-fixed-point iteration converges for any initial value $x_0 \in \Omega$, and the limit is the unique fixed-point of f.*

Proof: First, we note that by Remark 2, f must have a unique fixed-point and this fixed-point corresponds to x^* as defined in Definition 3. Now let $x_0 \in \Omega \setminus \{x^*\}$ be arbitrary. We assume without loss of generality that $x_0 \neq x^*$. We are left with two cases, either $x_0 > x^*$ or $x_0 < x^*$.

First, let $x_0 > x^*$. We show by induction that for $k \in \mathbb{N}$, $x_k > x^*$. Assume that for some $k \in \mathbb{N}$, we have that $x_k > x^*$. We find that

$$\begin{aligned} x_{k+1} &= \alpha f(x_k) + (1-\alpha)x_k \\ &= -|\alpha| f(x_k) + (1+|\alpha|)x_k \\ &\geq -|\alpha|[C(x_k - x^*) + x^*] + (1+|\alpha|)x_k \\ &= |\alpha|(C-1)x^* + [1 - |\alpha|(C-1)]x_k \\ &\geq |\alpha|(C-1)x^* + [1 - |\alpha|(C-1)]x^* \\ &= x^*, \end{aligned}$$

where we obtained the first inequality from Lemma 3, and we obtain the first equality and the second inequality from $-\frac{1}{C-1} < \alpha < 0$. We can thus conclude that $\forall k \in \mathbb{N} : x_k > x^*$. For $k \in \mathbb{N}$, we also have

$$\begin{aligned} x_{k+1} &= \alpha f(x_k) + (1-\alpha)x_k \\ &= -|\alpha| f(x_k) + (1+|\alpha|)x_k \\ &\leq -|\alpha| x_k + (1+|\alpha|)x_k \\ &= x_k, \end{aligned}$$

where we used that $\alpha < 0$ to obtain the first equality, and Lemma 3 to obtain the inequality. We conclude that the sequence $(x_k)_{k\in\mathbb{N}} \subset \Omega$ is strictly decreasing and has a lower bound. By the monotone convergence theorem, we find that $x := \lim_{k\to\infty} x_k$ exists. The rest of the proof is analogous to the proof of Lemma 2. ■

Based on the previous results, we can state and prove the following result.

Theorem 5. *Let $f \in C^1(\bar{\Omega};\mathbb{R})$ have at least one fixed-point, then, for any initial value $x_0 \in \Omega$, there exists an $A > 0$ such that either for all $0 < \alpha < A$ or for all $-A < \alpha < 0$, the α-relaxed-fixed-point iteration with respect to f converges to one of the fixed-points of f,*

where the required sign of α depends on f and the initial value x_0.

Proof: Let $x_1^* < ... < x_N^*$ denote the fixed-points of f. Let us define $x_0^* = \inf \Omega$ and $x_{N+1}^* = \sup \Omega$. Now take $x_0 \in \Omega$ arbitrary, then either x_0 is a fixed-point, or we can find $n \in \{0, ..., N\}$ such that $x_0 \in (x_n^*, x_{n+1}^*)$. Since $f \in C^1(\bar{\Omega})$, and there are no fixed-points between x_n^* and x_{n+1}^*, we must have that either $f(x) < x$ or $f(x) > x$ for all $x \in (x_n^*, x_{n+1}^*)$. Thus we must have that $f : (x_n^*, x_{n+1}^*) \to \mathbb{R}$ is either a pseudo-contraction or an expansion mapping. Then, by Lemma 2 or 4, we are done. ■

III. RESULTS

In this section, we consider the case of a circular high-temperature superconductor with a radius of 0.3m in two dimensions that can be modeled using equation 1 with $E_c = 1\mathrm{V\,m^{-1}}$, $J_c = 2.7 \cdot 10^8 \mathrm{A/m^2}$, and $n = 19$. The superconductor transports a sinusoidal current with a frequency of 50 Hz with different amplitudes perpendicular to our two-dimensional domain of consideration. For rotationally-symmetric domains, we can enforce the transport current through the conductor by fixing the tangential magnetic fields on the boundary.

A. Current Distribution in a Circular Conductor

As described above, we can enforce the total transport current through the circular conductor. However, the exact distribution of this current over the conductor is a-priori unknown. Note that the resistivity of the material as described by equation 1 depends on the local current density. Therefore, the distribution of the current over the conductor has an influence on how the material behaves locally. Since our domain is rotationally symmetric, the current distribution can be described as a function that only depends on the radial coordinate. Since we work with linear elements to represent the magnetic field, we have a piecewise-constant representation for the current density.

If we consider a classical conductor, then an analytical solution for the distribution of the current over the conductor is available [14]. In Fig. 1, we compare the current density computed by our method to the analytical solution and we see a good agreement. There is no analytical solution available for the current distribution in the case $n > 1$. We approximated the distribution using the method described in this work. In Fig. 2, we show the current distribution in the circular superconductor corresponding to a transport current of 10% and 20% of the critical current. One thing to observe is that the current density is either close to the critical current density or almost vanishes. This behaviour is not unexpected and was already postulated by Bean in 1962 [4][5].

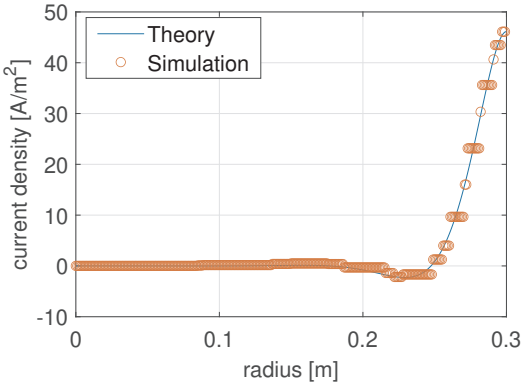

Fig. 1. We consider a classical conductor with a radius of 0.3m and a resistivity of $10^{-9}\Omega$ that transports current with an amplitude of 1000 A. The solid line and the circles respectively represent the analytical and numerical results for the current distribution.

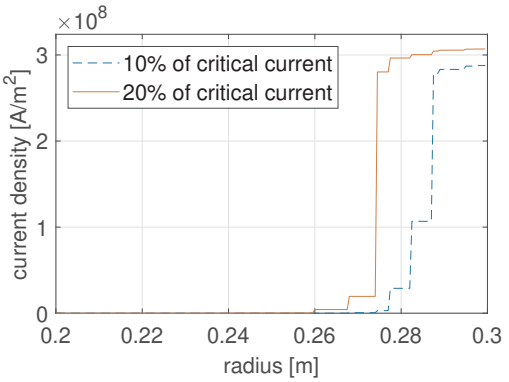

Fig. 2. The dashed and solid line represent the current distribution in the superconductor as predicted by our model when the superconductor transports a current with an amplitude respectively equal to 10% and 20% of the critical current.

B. Losses in a Circular Conductor

The time-averaged losses in our system can be approximated using

$$P = \frac{1}{T} \int_0^T \int_\Omega \rho(\mathbf{J}) |\mathbf{J}|^2 dx, \tag{13}$$

where P are the time-averaged losses, T is the final time of the simulation, Ω is the considered domain, and the relation between ρ and $\mathbf{J}$ is given by equation 1. In Fig. 3, we see that the approximate losses found by our method yield results that are close to the analytical results found in [2].

C. Performance

Since the performance of the general system is already described in [3], we will mainly focus on the performance of our chosen non-linear solver as described in section II-D. Theorem 5 shows a rather general convergence result for the relaxed-fixed-point iteration in the one-dimensional case. In this section, we will see that the solver also converges in higher dimensions. We consider

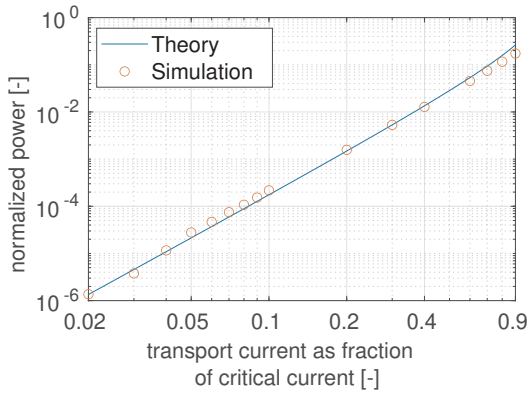

Fig. 3. The solid line and circles represent the normalized losses according to theory [2] and our numerical approximation, respectively. The normalized losses are the losses as described by equation 13 divided by $\frac{fI_c^2\mu}{\pi}$.

the equations

$$[f^{(1)}(x)] = \begin{bmatrix} \sin(10x_1)\cos(10x_2) \\ \sin(10x_2)\cos(10x_1) \end{bmatrix}. \tag{14}$$

and

$$[f^{(2)}(x)] = ([I] + [B(x)])^{-1}([b] + 2[B(x)]x), \tag{15}$$

where $[I]$ is the identity matrix,

$$[B(x)] = \begin{bmatrix} x_1^{18} + x_2^{18} & x_1^{18} \\ x_1^{18} + 7x_2^{18} & 32x_1^{18} + 2x_2^{18} \end{bmatrix}, \tag{16}$$

and

$$[b] = \begin{bmatrix} 5 \\ 3 \end{bmatrix}. \tag{17}$$

We plotted equation 15 in Fig. 4 for illustration purposes. It turns out in order to ensure convergence with initial guesses $x_0 = [2, 2]$ and $x_0 = [1.85, 1.75]$, we need to choose $0 < \alpha < 0.1$ and $-0.1 < \alpha < 0$ for equation 14 and 15, respectively. For several values of α, numerical experiments were performed, and the results are shown in Fig. 6 and 5.

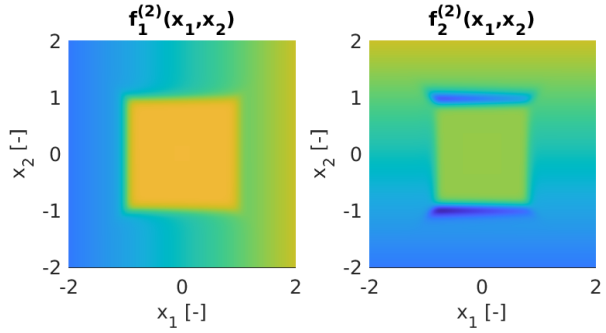

Fig. 4. A visualisation of equation 15.

These examples show good convergence results in the higher-dimensional case. However, for the real problem, we are more interested in run times. To evaluate this, we considered the problem of computing the magnetic fields

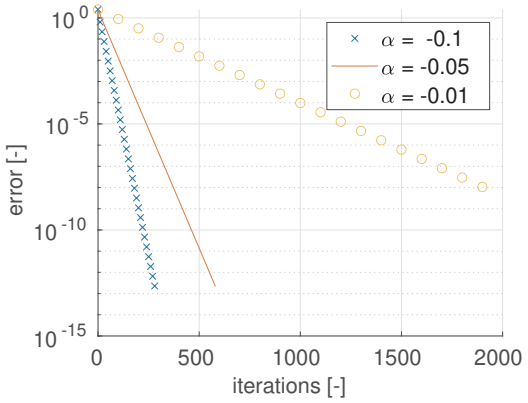

Fig. 5. The error as function of the number of iterations when the relaxed-fixed-point iteration is applied to equation 15. The error is defined as the euclidean distance between the estimate and the true fixed-point.

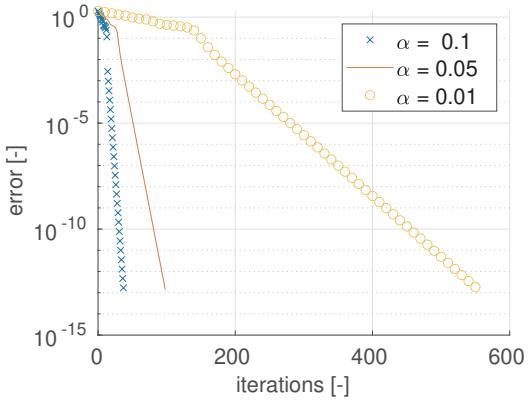

Fig. 6. The error as function of the number of iterations when the relaxed-fixed-point iteration is applied to equation 14. The error is defined as the euclidean distance between the estimate and the true fixed-point.

in in a circular superconducting wire with AC transport current as described in the beginning of this section. We performed a simulation of a circular superconductor with around 3000 degrees of freedom. The induced current is sinusoidal with a peak that is 10% of the critical current. In Figure 7 and 8, we respectively recorded the time and iterations required to solve the non-linear system at each individual time-step up to an accuracy of 10^{-4}, both by Newton's method and by the relaxed fixed-point method. We find that Newton's method requires fewer iterations to converge compared to the relaxed fixed-point method, but the run times are up to ten times as long. This can be explained by the fact that Newton's method needs to compute the Jacobian at every iteration. Despite a fully-vectorized implementation was used to evaluate an analytic equation for the gradient, this computation is still very costly.

IV. Conclusion

The relaxed-fixed-point iteration was chosen as non-linear solver for the system of non-linear equations that appears if one wants to approximate the magnetic

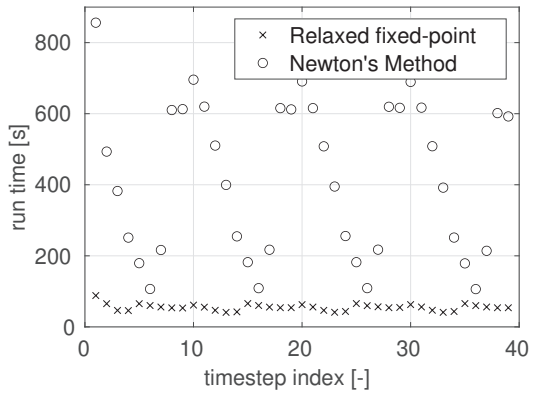

Fig. 7. We consider a superconductor that transports a current with an amplitude equal to 10% of the critical current. A simulation of 4 cycles was performed, and the time required to reach an accuracy of 10^{-4} when solving the non-linear system in equation 10 was recorded for both the relaxed-fixed-point iteration and Newton's method.

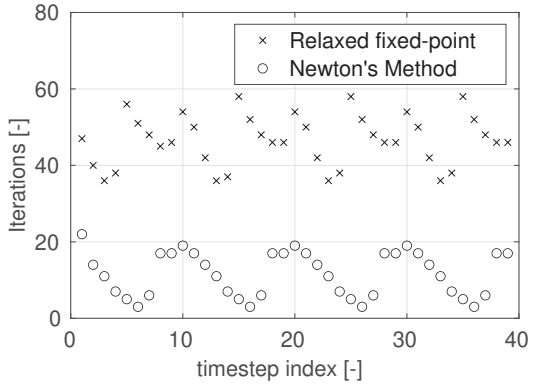

Fig. 8. We consider a superconductor that transports a current with an amplitude equal to 10% of the critical current. A simulation of 4 cycles was performed, and the number of iterations required to reach an accuracy of 10^{-4} when solving the non-linear system in equation 10 was recorded for both the relaxed-fixed-point iteration and Newton's method

fields in high-temperature superconductors using first-order Nédéléc elements and a second-order backward differentiation scheme. Rigorous convergence results were obtained in the one-dimensional case for any function with continuous derivative. Numerical experiments suggested that these strong convergence properties carry over to higher dimensions, even for highly-oscillating functions. Also for the non-linear system under consideration, the relaxed-fixed-point iteration converges in as little as one-tenth of the time compared to Newton's method.

REFERENCES

[1] A. Bussmann-Holder, H. Keller, "High-temperature superconductors: underlying physics and applications", Zeitschrift für Naturforschung B, vol 75, number 1-2, 2020

[2] W. Norris, "Calculation of hysteresis losses in hard superconductors carrying ac: isolated conductors and edges of thin sheets," Journal of Physics D: Applied Physics, Vol. 3, Num. 4, Apr. 1970

[3] R. Brambilla, F. Grilli, and L. Martini, "Development of an edge-element model for AC loss computation of high-temperature superconductors", Superconductor Science and Technology, vol. 20, num. 1, Nov. 2006

[4] C. P. Bean, "Magnetization of Hard Superconductors", Physical Review Letters. American Physical Society (APS). 8 (6): 250–253, 1962

[5] C. P. Bean , "Magnetization of High-Field Superconductors". Reviews of Modern Physics. American Physical Society (APS). 36 (1): 31–39, 1964

[6] J. Rhyner, "Magnetic properties and AC-losses of superconductors with power law current—voltage characteristics", Physica C: Superconductivity, vol 212, number 3, 1993

[7] Y. Law, D. Tageddine, S. Dufour, "3-D Numerical Modeling for the Magnetization of Superconductors Using a Local Discontinuous Galerkin Finite Element Method", IEEE Transactions on Magnetics, vol 55, number 8, 2019

[8] J. Smajic, "How to Perform Electromagnetic Finite Element Analysis", NAFEMS, 2016

[9] J. Jin, "The Finite Element Method in Electromagnetics", Wiley-IEEE press, Ed. 3, 2014, ch. 8

[10] P. Monk, "Finite element Methods for Maxwell's Equations", Oxford Scholarship Online, 2003, ISBN: 9780198508885

[11] R. Hiptmair, J. Li, J. Zou, "Convergence analysis of finite element methods for H(div;Ω)-elliptic interface problems", De Gruyter, vol 18, number 3, 2010

[12] A. Iserles, "A First Course in the Numerical Analysis of Differential Equations", Cambridge University Press, 1996

[13] H. Bauschke, and P. Combettes, "Convex Analysis and Monotone Operator Theory in Hilbert Spaces", Springer International Publisher, pp. 79

[14] W. L. Weeks, "Transmission and Distribution of Electrical Energy", Harper & Row, 1981, ISBN: 9780060469825

Finite-difference wave-propagation models for dispersive media: impact of space-time discretization

Zygiridis Theodoros (1), Kantartzis Nikolaos (2)

(1) Department of Electrical and Computer Engineering, University of Western Macedonia, Kozani, Greece
(2) Department of Electrical and Computer Engineering, Aristotle University of Thessaloniki, Thessaloniki, Greec

Purpose:

The computational accuracy and performance of finite-difference time-domain (FDTD) methods are affected by the implementation of approximating derivative formulae in diverse ways. This study aims to focus on FDTD models featuring material dispersion with negligible losses and investigates two specific aspects that, until today, are usually examined in the context of non-dispersive media only. These aspects pertain to certain abnormal characteristics of coarsely resolved electromagnetic waves and the selection of the proper time-step size, in the case of a high-order discretization scheme.

Design/methodology/approach:

Considering a Lorentz medium with negligible losses, the propagation characteristics of coarsely resolved waves is examined first, by investigating thoroughly the numerical dispersion relation of a typical discretization scheme. The second part of the study is related to the unbalanced space-time errors in FDTD schemes with dissimilar space-time approximation orders. The authors propose a remedy via the suitable choice of the time-step size, based on the single-frequency minimization of an error expression extracted, again, from the scheme's numerical dispersion formula.

Findings:

Unlike wave propagation in free space, there exist two parts of the frequency spectrum where waves in a Lorentz medium experience non-physical attenuation and display non-changing propagation constants, due to coarse discretization. The authors also show that an optimum time-step size can be determined, in the case of the (2,4) FDTD scheme, which minimizes the selected error formula at a specific frequency point, promoting more efficient implementations.

Originality/value:

Unique characteristics displayed by discretized waves, which have been known for non-dispersive media, are examined and verified for the first time in the case of dispersive materials, thus completing the comprehension of the space-time discretization impact on simulated quantities. In addition, the closed-form formula of the optimum time-step enables the efficient implementation of the (2,4) FDTD method, minimizing the detrimental influence of the low-order temporal integration.

Keywords:

Anisotropy, Electromagnetic waves, Finite difference time-domain analysis, Material modelling, Computational electromagnetics, Discretization error

Published in COMPEL - The international journal for computation and mathematics in electrical and electronic engineering, Vol. 41 No. 3, 2022, ISSN 0332-1649, page 1024 - 1040

Index of Authors

S

T

V

Z